56

AD

USAAVLABS TECHNICAL REPORT 67-68

THEORETICAL AND EXPERIMENTAL INVESTIGATION OF THE INSTANTANEOUS INDUCED VELOCITY FIELD IN THE WAKE OF A LIFTING ROTOR

By

N. Miller

J. C. Tang

A. A. Perlmutter

January 1968

U. S. ARMY AVIATION MATERIEL LABORATORIES
FORT EUSTIS, VIRGINIA

CONTRACT DA 44-177-AMC-383(T)
DYNASCIENCES CORPORATION
BLUE BELL, PENNSYLVANIA

172

Disclaimers

The findings in this report are not to be construed as an official Department of the Army position unless so designated by other authorized documents.

When Government drawings, specifications, or other data are used for any purpose other than in connection with a definitely related Government procurement operation, the United States Government thereby incurs no responsibility nor any obligation whatsoever; and the fact that the Government may have formulated, furnished, or in any way supplied the said drawings, specifications, or other data is not to be regarded by implication or otherwise as in any manner licensing the holder or any other person or corporation, or conveying any rights or permission, to manufacture, use, or sell any patented invention that may in any way be related thereto.

Trade names cited in this report do not constitute an official endorsement or approval of the use of such commercial hardware or software.

Disposition Instructions

Destroy this report when no longer needed. Do not return it to originator.

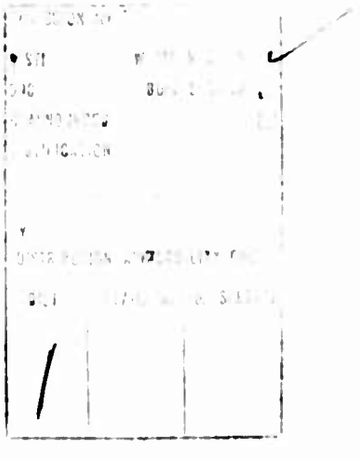

DEPARTMENT OF THE ARMY
U. S. ARMY AVIATION MATERIEL LABORATORIES
FORT EUSTIS, VIRGINIA 23604

This report has been reviewed by the U. S. Army Aviation Materiel Laboratories and is considered to be technically sound. The experimental program was undertaken to provide data for comparison with the analytical prediction of induced rotor wake velocities and to determine if in-flight measurements of rotor wake flow could be made with acceptable accuracy.

Task 1F125901A13903
Contract DA 44-177-AMC-383(T)
USAAVLABS Technical Report 67-68
January 1968

THEORETICAL AND EXPERIMENTAL INVESTIGATION OF THE INSTANTANEOUS INDUCED VELOCITY FIELD IN THE WAKE OF A LIFTING ROTOR

Dynasciences Report No. DCR-227

By

N. Miller
J. C. Tang
A. A. Perlmutter

Prepared by

Dynasciences Corporation
Blue Bell, Pennsylvania

for

U. S. ARMY AVIATION MATERIEL LABORATORIES
FORT EUSTIS, VIRGINIA

SUMMARY

Measurements have been made of the instantaneous and time-averaged values of the induced velocities in the wake of a full-scale helicopter in actual steady flight conditions. These measurements were made with three-dimensional pitot static and two-dimensional hot film probes. The test setup provided for measurements at several radial, axial, and azimuthal positions relative to the rotor centerline.

Simple, analytical methods are formulated to predict the instantaneous and time-averaged, induced velocities in the rotor wake.

Calculated values of the induced velocities are compared with the experimental data, and agreement is obtained for the hovering flight condition.

FOREWORD

This investigation was performed by Dynasciences Corporation for the United States Army Aviation Materiel Laboratories under Contract DA 44-177-AMC-383(T). Mr. William E. Sickles was the Army Project Engineer. The following Dynasciences Corporation personnel authored or contributed to this report:

Mr. N. Miller - Project Engineer
Mr. J. C. Tang - Aeronautical Engineer
Mr. E. Fraundorf - Test Engineer
Dr. A. A. Perlmutter - Senior Vice-President
Mr. J. Jones - Senior Design Engineer

TABLE OF CONTENTS

ILLUSTRATIONS

LIST OF TABLES

SYMBOLS

a	fuselage equivalent radius, ft.
a'	a/R
D	rotor diameter, ft.
H	vertical distance from rotor plane to ground, ft.
h	vertical distance from rotor plane to fuselage, ft.
h'	h/R
$K(k)$	complete elliptical integral of the first kind (see equations (18) and (19))
M	strength of the three-dimensional doublet representing the fuselage
N	number of blades
n	rotor rotational speed, rev./sec.
p'	perturbation pressure, lb./ft.^{2}
R	rotor radius, ft.
R_e	local wake radius, ft.
r	radius distance measured from X-axis, ft. (see Figure 1)
r'	r/R
T	rotor thrust, lb.
U	resultant axial velocity through the rotor disk, lb./sec.
u	instantaneous induced velocity inside the rotor wake, ft./sec.

$\bar{u}$	time-averaged, induced velocity inside the rotor wake, ft./sec.
$\bar{u}_0$	momentum value of rotor induced velocity at the rotor disk, ft./sec.
x	axial distance from the rotor disk, ft. (see Figure 1)
x'	x/R
$\bar{x}$	vertical distance from the plane containing the fuselage CG and parallel to the rotor plane (see Figure 8)
$\bar{x}'$	x/R
α	angular position of any point P with respect to the positive Y-axis (see Figure 1)
α_1	angle defining point P with vertex on X_1-axis parallel to the Y_1-Z_1 plane
$\bar{\alpha}$	angle defining point P with vertex on X_1-axis measured from the positive Y-axis parallel to the X-Y plane
Γ	circulation of the vortex system representing one blade, ft.^{2}/sec.
Γ_t	blade tip circulation of a triangularly loaded blade, ft.^{2}/sec.
θ	angular position of blade with respect to the Y-axis (see Figure 1)
θ'	angular position of any point P with respect to the blade, $\theta'=\theta-\alpha$ (see Figure 1)
ρ	air mass density, slug/ft.^{3}
t	time, sec.

ϕ yawed angle (see Figure 6)

χ wake angle (see Figure 6)

ψ azimuth test position measured from the downwind position in the direction of ω

ψ_d stream function of the three-dimensional doublet representing the fuselage

ψ_n stream function of the induced flow inside the wake of a free lifting rotor

ω rotor angular speed, rad./sec.

SUBSCRIPTS

b pertaining to bound vortex

c pertaining to central vortex

h pertaining to helical vortex

L pertaining to the longitudinal direction

N pertaining to the normal direction, which is perpendicular to the rotor plane

n pertaining to n^{th} blade

r pertaining to the radial direction in the X, Y, Z coordinate system

y pertaining to the lateral direction

α pertaining to the tangential direction in the X, Y, Z coordinate system

I. INTRODUCTION

The induced flow is one of the important parameters which determine the aerodynamic loads of the fuselage and wing surfaces immersed in the wake of helicopter rotors. Large effects on the stability and control of helicopters can be experienced as a result of the induced flow acting on tail surfaces. Very pronounced effects of the induced flow field are also evident in the performance, stability, and vibration characteristics of tandem rotor helicopters, where the rear rotor blades operating in the wake of the front rotor downwash are subjected to local alternating air loads. The actual flow field in the wake of helicopter rotors varies both with time and location relative to the rotor. Previous analyses of these alternating air velocities are relatively complex and require the use of considerable time of high-speed digital computers. Although digital computer methods represent an extremely useful tool for some applications, especially since they permit the elimination of several restrictive assumptions, it is recognized that the use of these computers is an expensive proposition. It is desirable, therefore, to continue the search for analytical methods which promise to provide a simpler and preferably a closed-form type of solution to the rotor wake velocity problem.

The effort under the program reported herein was directed, therefore, toward the development of such simpler analytical methods. In addition, full-scale measurements were performed of the time-averaged and time-dependent velocities at several locations in the rotor wake of a Hughes Model-269 helicopter.

Comparisons were made of a number of test points and the corresponding theoretical values. The results of these comparisons as well as the details of the theoretical analyses and the test program are described in the following sections.

II. THEORETICAL ANALYSIS

The aerodynamic forces acting on the fuselage and lifting surfaces of helicopters are greatly influenced by the rotor induced flow. This flow, in general, is time dependent with frequencies which are harmonics of the rotor angular speed. Available analytical methods, such as those of References 1 through 3, are relatively complex and require the use of digital computers to obtain specific solutions.

In Reference 4 an analysis is presented which results in simple, closed-form solutions to the normal average induced velocity in the wake of a rotor for both hover and forward speeds.

In the program reported herein, the analysis of Reference 4 has been extended to obtain the instantaneous, in addition to the time-averaged, induced velocity in the rotor wake. Also, an attempt has been made to account for the effect of the fuselage on the induced flow.

The analysis is performed in several parts as follows:

A. Axial Flow
B. Yawed Flow
C. Fuselage Effects
D. Ground Effect
E. Wake Contraction

A. AXIAL FLOW

The average velocity, U , through a rotor or a propeller operating in an axial flow condition can be expressed as

$$U = V + \bar{u}_0 \tag{1}$$

where V is the free-stream velocity, and $\bar{u}_0$ is the momentum value of rotor induced velocity at the rotor disk, given by

$$\bar{u}_0 = \frac{T}{2\rho\pi R^2 (V+\bar{u}_0)} \tag{2}$$

For any given axial flight condition, U and $\bar{u}_0$ can therefore be determined from the above two equations.

In the present analysis, the normal induced velocity in the rotor wake is derived for two idealized loadings, i.e., uniform and triangular. The analysis can, however, be extended to the general case of arbitrary loading.

The velocity induced at point P inside the rotor wake is derived with respect to a cylindrical coordinate system fixed to the n^{th} blade. Definitions of this coordinate system and the induced velocity components are illustrated in Figure 1. As noted in Figure 2, the effect of rotor wake contraction is neglected.

1. Uniform Disk Loading

A uniformly loaded rotor is also one of constant circulation along the rotor blade span. In this case, vorticity is shed only at the blade tips and the rotor axis. The induced velocities are derived based on the wake structure shown in Figure 2. According to this wake structure, each blade is approximated by a vortex system consisting of a bound vortex fixed to the blade, a vortex helix which trails from the blade, and a central vortex along the rotor axis. This vortex line representation is similar to that used in the theory of finite wings having a large aspect ratio (Reference 5).

a. Time-Averaged, Induced Velocity

(i) Normal Velocity Component, $\bar{u}_N$

The time-averaged, induced velocity is derived in Reference 4 for an incompressible, irrotational, and nonviscous flow. Using Reference 4, we find that the perturbation pressure can be expressed as

$$p' = -\rho U(u_{N_h} + u_{N_b}) - \rho\omega r(u_{a_h} + u_{a_c} + u_{a_b}) \qquad (3)$$

For the time-averaged pressure condition, the effect of the bound vortex can be neglected; hence, equation (3) reduces to

$$p' = -\rho U u_{N_h} - \rho \omega r (u_{a_h} + u_{a_c}) \tag{4}$$

When the notation of Figure 2 is used, the induced velocity at any point P(x,y,z) can be computed by use of the Biot-Savart law

$$d\bar{q} = \frac{\Gamma}{4\pi} \cdot \frac{d\bar{s} \times \bar{a}}{|\bar{a}|^3} \tag{5}$$

where $d\bar{s}$ is the vector length of a vortex element, $\bar{a}$ is the vector distance to point P from the vortex element, and $d\bar{q}$ is the induced velocity vector.

The normal velocity component is induced only by the helical vortex. As shown in Reference 4, this velocity component can be written as

$$u_{N_h} = \frac{\Gamma}{4JR} \int_0^{\infty} \frac{\left[1 - r' \cos\left(\theta - \frac{\pi \xi'}{J}\right)\right] d\xi'}{\left\{(X' - \xi')^2 + r'^2 + 1 - 2r' \cos\left(\theta - \frac{\pi}{J}\xi'\right)\right\}^{3/2}} \tag{6}$$

where

$$\xi' = \frac{Ut}{R}$$

$$\theta' = \theta - \alpha$$

$$J = \frac{U}{nD}$$

$$x' = \frac{x}{R}$$

$$r' = \frac{r}{R}$$

Similarly, the tangential velocity component induced by the helical vortex is

$$u_{\alpha_h} = \frac{\Gamma}{4\pi R} \int_0^{\infty} \frac{\left[r'-(x'-\xi')\frac{\pi}{J}\sin\left(\theta'\frac{\pi}{J}\xi'\right)-\cos\left(\theta'-\frac{\pi}{J}\xi'\right)\right]d\xi'}{\left[(x'\xi')^2+r'^2+1-2r'\cos\left(\theta'-\frac{\pi}{J}\xi'\right)\right]^{3/2}} \quad (7)$$

Since neither equation (6) nor equation (7) is integrable, the method proceeds by first substituting equations (6) and (7) into equation (4). There follows that

$$p' = -\frac{\rho\Gamma\omega}{4\pi} \int_0^{\infty} \frac{\left[1-2r'\cos\left(\theta'-\frac{\pi}{J}\xi'\right)+r'^2-r'(x'-\xi')\frac{\pi}{J}\sin\left(\theta'-\frac{\pi}{J}\xi'\right)d\xi'\right.}{\left[(x'-\xi')^2+r'^2+1-2r'\cos\left(\theta'-\frac{\pi}{J}\xi'\right)\right]^{3/2}} - \quad (8)$$

$$-\rho\omega r' u_{\alpha_c}$$

It can be shown by direct differentiation that the integral in equation (8) can be evaluated as:

$$\left.\frac{\xi' - x'}{\left[(x'-\xi')^2 + r'^2 + 1 - 2r'\cos\left(\theta' - \frac{\pi}{J}\xi'\right)\right]}\right|_0^{\infty} \qquad (9)$$

Thus,

$$p' = -\frac{\rho\Gamma\omega}{4\pi}\left[1 + \frac{x'}{\left[1 + r'^2 + x'^2 - 2r'\cos\theta'\right]^{1/2}}\right] - \rho\omega r' u_{\alpha_c} \qquad (10)$$

It should be noted that the perturbation pressure at the point P(x,y,z) or, using polar coordinates, P(x,r,α), given by equation (10), is that due to one blade at azimuth position θ . This pressure is, of course, dependent on the angle $\theta' = \theta - \alpha$, which represents the relative position between the blade and the point under consideration. For a given point, the pressure will vary as the rotor revolves and, hence, is a time-varying quantity.

The time dependency of the pressure at any point may be removed either by using the concept of an infinite number of blades, or by averaging the pressure during one revolution of the blade. This is equivalent to stating that

$$\frac{1}{2\pi}\int_0^{2\pi} p'\,d\theta' = -\frac{\rho U}{2\pi}\int_0^{2\pi} u_N\,d\theta' - \frac{\rho\omega}{2\pi}\int_0^{2\pi} r' u_{\alpha_h}\,d\theta' - \frac{\rho\omega}{2\pi}\int_0^{2\pi} r' u_{\alpha_c}\,d\theta' \qquad (11)$$

Since the flow induced solely by helical vortex is irrotational within the helical cylinder, there follows that

$$\int_0^{2\pi} r' u_{a_h} d\theta' = 0 \tag{12}$$

Also, u_{a_c} is independent of θ', so that the last term in equation (12) is equal to $\rho\omega r' u_{a_c}$. The normal average induced velocity may be defined by

$$\bar{u}_N = \frac{1}{2\pi} \int_0^{2\pi} u_N \, d\theta' \tag{13}$$

Equation (11) therefore becomes

$$\bar{u}_N = \frac{-1}{2\pi\rho U} \int_0^{2\pi} p' d\theta' - \rho\omega r' u_{a_c} \tag{14}$$

When equation (10) is substituted into equation (14),

$$\bar{u}_N = \frac{\Gamma\omega}{4\pi U} \left\{ 1 + \frac{1}{2\pi} \int_0^{2\pi} \frac{x' d\theta'}{\left[1 + r'^2 + x'^2 2r' \cos\theta' \right]^{1/2}} \right\} \tag{15}$$

The integral in equation (15) can be transformed into the complete elliptical integral of the first kind by the following substitutions. Let

$$\left.\begin{aligned} \beta &= \theta' \\ b^2 &= (r'+1)^2 + x'^2 \\ c^2 &= (r'-1)^2 + x'^2 \end{aligned}\right\} \qquad (16)$$

There follows that

$$1 + r'^2 + x'^2 - 2r' \cos\theta' = \frac{b^2+c^2}{2} - \frac{(b^2-c^2)\cos\beta}{2}$$

$$= b^2 \sin^2\frac{\beta}{2} + c^2 \cos^2\frac{\beta}{2} \qquad (17)$$

Letting

$$\frac{\beta}{2} = \frac{\pi}{2} - \delta,$$

$$\int_0^{2\pi} \frac{x'\,d\theta'}{\left[1 + r'^2 + x'^2 - 2r'\cos\theta'\right]} = 4x' \int_0^{\frac{\pi}{2}} \frac{d\delta}{\sqrt{b^2\cos^2\delta + c^2\sin^2\delta}}$$

$$= \frac{4x'}{b} \int_0^{\frac{\pi}{2}} \frac{d\delta}{\sqrt{1-k^2\sin^2\delta}} \qquad (18)$$

where

$$k^2 = 1 - \frac{c^2}{b^2} < 1$$

Substituting equation (18) into equation (15) yields

$$\bar{u}_N = \frac{\Gamma\omega}{4\pi U}\left[1 + \frac{2x'}{\pi b} K(k)\right] \tag{19}$$

where K(k) represents the complete elliptical integral of the first kind. For N blades the normal average induced velocity is obtained by multiplying the right-hand side of equation (19) by N.

The total thrust of the rotor is given by

$$T = N\int_0^R \rho\omega r\Gamma dr = \rho\frac{\omega R^2}{2}\Gamma N \tag{20}$$

There follows that

$$\frac{N\Gamma\omega}{4\pi U} = \frac{T}{2\pi R^2 \rho U} \tag{21}$$

Substituting equation (21) into equation (19), we find that

$$\bar{u}_N = \frac{T}{2\rho\pi R^2 U}\left[1+\frac{2x'}{\pi b}K(k)\right] \tag{22}$$

When equation (22) is expressed in terms of $\bar{u}_0$, given in equation (2), there finally results

$$\bar{u}_N = \bar{u}_0\left[1+\frac{2x'}{\pi b}K(k)\right] \tag{23}$$

(ii) Tangential Velocity Component, $\bar{u}_\alpha$

In axial flow condition, the central vortex is shed down along the rotor axis, and hence the velocity induced by the central vortex is always in the tangential direction. Referring to Figure 3 and utilizing the Biot-Savart law, we find that the velocity, $d\bar{u}_{\alpha_c}$, induced at point P(x,r,α) by the central vortex element $d\bar{s}$ can be expressed as follows:

$$d\bar{u}_{\alpha_c} = \frac{\Gamma}{4\pi}\frac{d\bar{s}\times\bar{a}}{|\bar{a}|^3} \tag{24}$$

$$= -\frac{\Gamma}{4\pi}\left\{\frac{r\,d\xi}{\left[(x-\xi)^2+r^2\right]^{3/2}}\right\}\bar{e}_\alpha$$

where $\bar{e}_\alpha$ is the unit vector in the tangential direction opposite to ω .

By integrating equation (24) from $\xi = 0$ to $\xi = \infty$, the velocity induced by the central vortex is obtained as

$$u_{a_c} = -\frac{\Gamma}{4\pi r' R}\left[\frac{x'}{(r'^2+x'^2)^{1/2}}+1\right] \tag{25}$$

For an N-bladed rotor, this induced velocity becomes

$$u_{a_c} = -\frac{N\Gamma}{4\pi r' R}\left[\frac{x'}{(r'^2+x'^2)^{1/2}}+1\right] \tag{26}$$

It should be noted in equation (26) that the velocity induced by the central vortex, U_{a_c}, is independent of the angular position of the blade and the point P. Its time-averaged value, $\bar{u}_{a_{c_1}}$, can therefore be represented by the same expression.

In considering the total time-averaged tangential velocity, $\bar{u}_a$, the effects of the bound vortex and the helical vortex can be neglected. $\bar{u}_a$ is therefore given by the same expression as $\bar{u}_{a_c}$. Thus,

$$\bar{u}_a = -\frac{N\Gamma}{4\pi R r'}\left[\frac{x'}{(r'^2+x'^2)^{1/2}}+1\right] \tag{27}$$

(iii) Radial Velocity Component, $\bar{u}_r$

When the normal and tangential velocity components are known, the radial velocity component is derived from the equation of continuity, which states

$$-\frac{1}{r}\frac{\partial}{\partial r}(r\bar{u}_r)-\frac{1}{r}\frac{\partial u_\alpha}{\partial \theta'}+\frac{\partial u_N}{\partial x}=0 \qquad (28)$$

The minus signs indicate that $\bar{u}_r$ and $\bar{u}_\alpha$ are in the opposite direction of r and θ', respectively.

As noted in Reference 4, the normal velocity component $\bar{u}_N$ does not appreciably vary with radial distance r; hence, equation (23) can be simplified as follows:

$$\bar{u}_N(r',x')=\bar{u}_N(r'=0,x')=\bar{u}_0\left[1+\frac{x'}{\sqrt{1+x'^2}}\right] \qquad (29)$$

When equations (27) and (29) are substituted into (28) and with the boundary condition $\bar{u}_r = 0$ at $r = 0$, we find that the time-averaged, radial-induced velocity is

$$\bar{u}_r=\frac{\bar{u}_0}{2}\left[\frac{r'}{(1+x'^2)^{3/2}}\right] \qquad (30)$$

b. Instantaneous Induced Velocity

(i) Normal Velocity Component, u_N

The instantaneous value of the normal induced velocity component can be obtained by using a method similar to that employed for the average value. However, in this case the effect of the bound vortex must be retained.

Again referring to equation (3) and using equations (6) and (7), we find that the perturbation pressure can be written as

$$p' = -\frac{\rho\Gamma\omega}{4\pi}\left[1+\frac{x'}{(1+x'^2+r'^2-2r'\cos\theta')^{1/2}}\right] - \rho U(u_{N_b}) - \rho\omega r'(u_{\alpha_c}+u_{\alpha_b})$$

The total normal induced velocity is

$$u_N = u_{N_h} + u_{N_b} \tag{32}$$

Combining equations (3), (31), and (32), there follows that

$$u_N = \frac{\Gamma\omega}{4\pi U}\left[1+\frac{x'}{(1+x'^2+r'^2-2r'\cos\theta')^{1/2}}\right] + u_{N_b} - \frac{\omega r'}{U}(u_{\alpha_h}) \tag{33}$$

Due to the fact that the total tangential velocity component is small compared to the normal component induced in the rotor wake, and since the tangential velocity induced by the helical vortex, u_{α_h}, is only a small fraction of the total tangential velocity induced, u_{α_h} in equation (33) is therefore neglected in this analysis, and the normal induced velocity becomes

$$u_N = \frac{\Gamma\omega}{4\pi U}\left[1+\frac{x'}{(1+x'^2+r'^2-2r'\cos\theta')^{1/2}}\right] + u_{N_b} \tag{34}$$

In the above equation, the normal velocity component induced by the blade bound vortex, u_{Nb}, can be derived directly from the Biot-Savart law as follows:

Referring to Figure 4, we find that the velocity $d\bar{u}_b$ induced at point P by the bound vortex element $d\bar{s}$ is given by

$$d\bar{u}_b = \frac{\Gamma}{4\pi} \frac{d\bar{s} \times \bar{a}}{|\bar{a}|^3} \tag{35}$$

When the above vector quantities are resolved into components along X, Y, Z axes, there results

$$d\bar{u}_b = du_{x_b}\bar{i} + du_{y_b}\bar{j} + du_{z_b}\bar{k} \tag{36}$$

$$d\bar{s} \times \bar{a} = R^2(r' \sin\theta' ds'\bar{i} - x' \sin\theta\, ds'\bar{j} - x' \cos\theta ds'\bar{k}) \tag{37}$$

$$|\bar{a}|^3 = R^3 (x'^2 + r'^2 + s'^2 - 2r's' \cos\theta')^{3/2} \tag{38}$$

where

$$ds' = \frac{ds}{R}, \; s' = \frac{s}{R}$$

and $\bar{i}$, $\bar{J}$, and $\bar{k}$ are unit vectors.

The normal velocity component can be obtained from equations (36), (37), and (38) by solving for the i^{th} component of equation (35); thus,

$$du_{N_b} = \frac{\Gamma}{4\pi R}\left[\frac{r'\sin\theta' ds'}{(x'^2+r'^2+s'^2-2r's'\cos\theta')^{3/2}}\right] \qquad (39)$$

When equation (39) is integrated from blade root to tip, there results

$$u_{N_b} = \frac{\Gamma}{4\pi R}\int_0^1\left[\frac{r'\sin\theta' ds'}{(x'^2+r'^2+s'^2-2r's'\cos\theta')^{3/2}}\right]$$

$$= \frac{\Gamma r'\sin\theta'}{4\pi R(x'^2+r'^2\sin^2\theta')}\left[\frac{1-r'\cos\theta'}{(x'^2+r'^2+1-2r'\cos\theta')^{1/2}}+\frac{r'\cos\theta'}{(x'^2+r'^2)^{1/2}}\right] \qquad (40)$$

When equation (40) is substituted into (34), the normal velocity induced by one blade in the rotor wake is obtained as

$$u_N = \frac{\Gamma\omega}{4\pi U}\left[1+\frac{x'}{(1+x'^2+r'^2-2r'\cos\theta')^{1/2}}\right]$$

$$+\frac{\Gamma r'\sin\theta'}{4\pi R(x'^2+r'^2\sin^2\theta')}\left[\frac{1-r'\cos\theta'}{(1+x'^2+r'^2-2r'\cos\theta')^{1/2}}+\frac{r'\cos\theta'}{(x'^2+r'^2)^{1/2}}\right] \qquad (41)$$

If we neglect the mutual interaction between the vortex systems representing different blades, the normal velocity induced by an N-bladed rotor is obtained simply by superposition of the velocities induced by each blade. This procedure is expressed mathematically as follows:

for an N-bladed rotor,

$$u_N = \sum_{n=1}^{N} \left[\frac{\Gamma\omega}{4\pi U} \left(1 + \frac{x'}{A}\right) + \frac{\Gamma r' \sin\theta'_n}{4\pi R(x'^2 + r'^2 \sin^2\theta'_n)} \left(\frac{1 - r'\cos\theta'_n}{A} + \frac{r'\cos\theta'_n}{B} \right) \right] \qquad (42)$$

where

$$A = (1 + x'^2 + r'^2 - 2r'\cos\theta'_n)^{1/2} \qquad (43)$$

$$B = (x'^2 + r'^2)^{1/2} \qquad (44)$$

(ii) Tangential Velocity Component, u_α

The tangential velocity, u_α , induced by the rotor is obtained by considering the effects of the central vortex and the bound vortex. The effect of the helical vortex on the induced velocity is small in the tangential direction and hence is neglected. The velocity induced by the central vortex, u_{α_c} , is readily derived in equation (26). The tangential velocity induced by the bound vortex can be obtained by an analysis similar to the one of the previous section. Again referring to Figure 4 and the Biot-Savart law, the Y and Z components of the velocity induced by the bound vortex are obtained as

$$u_{y_b} = -\frac{\Gamma x' \sin\theta}{4\pi R} \int_0^1 \frac{ds'}{(x'^2 + r'^2 + s'^2 - 2r's'\cos\theta')^{3/2}} \qquad (45)$$

$$u_{z_b} = -\frac{\Gamma x' \cos\theta}{4\pi R} \int_0^1 \frac{ds'}{(x'^2 + r'^2 + s'^2 - 2r's'\cos\theta')^{3/2}} \qquad (46)$$

Resolving u_{y_b} and u_{z_b} in the tangential direction, there results

$$u_{\alpha_b} = u_{y_b} \sin\alpha + u_{z_b} \cos\alpha \qquad (47)$$

When equations (45) and (46) are substituted into (47) and integrating, the tangential velocity induced by the bound vortex on one blade becomes

$$u_{\alpha_b} = -\frac{\Gamma x' \cos\theta'}{4\pi R(x'^2 + r'^2 \sin^2\theta')}\left[\frac{1 - r'\cos\theta'}{A} + \frac{r'\cos\theta'}{B}\right] \qquad (48)$$

For an N-bladed rotor,

$$u_{\alpha_b} = \sum_{n=1}^{N}\left[-\frac{\Gamma x' \cos\theta'_n}{4\pi R(x'^2 + r'^2 \sin^2\theta'_n)}\left(\frac{1 - r'\cos\theta'_n}{A} + \frac{r'\cos\theta'_n}{B}\right)\right] \qquad (49)$$

When equations (26) and (49) are combined the total tangential velocity component becomes

$$u_\alpha = -\frac{N\Gamma}{4\pi R r'}\left(\frac{x'}{B} + 1\right) - \sum_{n=1}^{N}\left[\frac{\Gamma x' \cos\theta'_n}{4\pi R(x'^2 + r'^2 \sin^2\theta'_n)}\left(\frac{1 - r'\cos\theta'_n}{A} + \frac{r'\cos\theta'_n}{B}\right)\right] \qquad (50)$$

(iii) Radial Velocity Component, $\bar{u}_r$

From equations (45) and (46) it can be noted that the radial velocity induced by the bound vortex is zero, since

$$u_{r_b} = u_{z_b} \sin\alpha - u_{y_b} \cos\alpha = 0$$

Since the velocity induced by the central vortex is only in the tangential direction, the radial velocity component is induced only by the helical vortex. Assuming furthermore that u_N does not vary appreciably with r', equation (42) reduces to the averaged value given in equation (29). There follows that the radial induced velocity, u_r , is the same as its time-averaged value given in equation (30).

$$u_r = \bar{u}_r = \frac{\bar{u}_0}{2}\left[\frac{r'}{(1+x'^2)^{3/2}}\right] \tag{51}$$

2. Triangular Disk Loading

Based on the results of uniform loading, the normal induced velocity for a triangularly loaded rotor is obtained by superposition of uniformly distributed loadings. In this case, the circulation of the bound vortex along the rotor blade, instead of being constant, will vary along the length of the blade, and helical vortices will be shed all along the blade, thus forming a vortex sheet of helicoid shape. This vortex sheet is generated in a way similar to the flat vortex sheet behind a lifting wing of nonuniform loading. In a triangularly loaded rotor, this helical vortex sheet replaces the blade tip helical vortex and the central vortex which exist in the case of uniform loading, as previously discussed.

a. Time-Averaged, Induced Velocity

(i) Normal Induced Velocity Component, $\bar{u}_N$

This velocity component of a triangularly loaded rotor is obtained from the results derived in uniform loading by a method of superposition. Figure 5 is a graphical representation of a triangularly loaded blade with circulation, $\Gamma=\Gamma_t(r/R)$. The blade tip circulation, Γ_t, may be evaluated since

$$T=\int_0^R N\rho\omega\Gamma dr=N\rho\omega\Gamma_t\frac{R^2}{3}$$

Consequently,

$$\Gamma_t=\frac{3T}{N\rho\omega R^2} \tag{52}$$

It can be seen in Figure 5 that the velocity induced by the triangular loading, $\Gamma=\Gamma_t(r/R)$, can be obtained by the difference between that due to the assumed uniform loading, Γ_t, shown in dotted line in Figure 5, and that due to the integrated loading of $d\Gamma_i$ from $r = 0$ to $r=R$.

The normal average induced velocity of an N-bladed rotor induced by the uniform loading, Γ_t, at point P(x,r) is obtained from equation (29).

$$\bar{u}_{N\,t}=\frac{N\Gamma_t\omega}{4\pi U}\left(1+\frac{x'}{\sqrt{1+x'^2}}\right) \tag{53}$$

Similarly, the normal velocity induced by the differential uniform loading, $d\Gamma_i$, at point P can be expressed as follows:

$$d\bar{u}_{N_i} = \frac{N d\Gamma_i \omega}{4\pi U}\left(1 + \frac{x'_i}{\sqrt{1+x'^2_i}}\right) \tag{54}$$

where

$$d\Gamma_i = \Gamma_t\, d\left(\frac{R_i}{R}\right) \tag{55}$$

$$\left.\begin{aligned} x'_i &= \frac{x}{R_i} = x'\left(\frac{R}{R_i}\right) \\ r'_i &= \frac{r}{R_i} = r'\left(\frac{R}{R_i}\right) \end{aligned}\right\} \tag{56}$$

Substituting equations (55) and (56) into equation (54), we have

$$d\bar{u}_{N_i} = \frac{N\Gamma_t \omega d\left(\frac{R_i}{R}\right)}{4\pi U}\left[1 + \frac{x'\left(\frac{R}{R_i}\right)}{\sqrt{1+x'^2\left(\frac{R}{R_i}\right)^2}}\right] \tag{57}$$

It may be seen (Reference 6) that the velocity induced by a vortex cylinder is discontinuous across the vortex boundary and that outside the boundary the induced velocity is negligible. Thus, the velocity induced at a given radial station is affected only by vortices shed by the blade outside this station. The induced velocity, $\bar{u}_{N_i}$, at point P(x,r) due to the uniformly distributed loadings, $d\Gamma_i$, superimposed along the blade is therefore obtained by integrating equation (57) from $R_i = r$ to $R_i = R$. Thus,

$$\bar{u}_{Ni} = \int_{r'}^{1} \frac{N\Gamma_1 \omega}{4\pi U} \left[1 + \frac{x'}{\sqrt{\left(\frac{R_i}{R}\right)^2 + x'^2}} \right] d\left(\frac{R_i}{R}\right) \tag{58}$$

$$\bar{u}_{Ni} = \frac{N\Gamma_1 \omega}{4\pi U} \left[(1-r') + x' \left(\ln \frac{1+\sqrt{1+x'^2}}{r'+\sqrt{r'^2+x'^2}} \right) \right] \tag{59}$$

The normal velocity, $\bar{u}_N$, induced by the triangular loading, Γ , is therefore obtained from equations (53) and (59) by the relation $\bar{u}_N = \bar{u}_{N_1} - u_{Ni}$. Thus,

$$\bar{u}_N = \frac{N\Gamma_1 \omega}{4\pi U} \left\{ r' + x' \left[\frac{1}{\sqrt{1+x'^2}} - \ln \frac{1+\sqrt{1+x'^2}}{r'+\sqrt{r'^2+x'^2}} \right] \right\} \tag{60}$$

Substituting equation (52) into equation (60), there results that

$$\bar{u}_N = \frac{3T}{4\rho\pi R^2 U} \left\{ r' + x' \left[\frac{1}{\sqrt{1+x'^2}} - \ln \frac{1+\sqrt{1+x'^2}}{r'+\sqrt{r'^2+x'^2}} \right] \right\} \tag{61}$$

Expressing $\bar{u}_N$ in terms of $\bar{u}_0$, equation (61) becomes

$$\bar{u}_N = \frac{3}{2}\bar{u}_0\left\{r' + x'\left[\frac{1}{\sqrt{1+x'^2}} - \ln\frac{1+\sqrt{1+x'^2}}{r'+\sqrt{r'+x'^2}}\right]\right\} \qquad (62)$$

(ii) Tangential Velocity Component, $\bar{u}_a$

In a triangularly loaded rotor, the helical vortex sheet replaces the central vortex which exists in the case of uniform loading. In obtaining the tangential velocity component in a triangularly loaded rotor, the approach utilizing the effect of a central vortex, considered in the case of uniform loading, is therefore not applicable. This velocity component, however, can be obtained by numerically averaging the instantaneous tangential velocity induced by the bound vortex. This instantaneous value is given by equation (72).

(iii) Radial Velocity Component, $\bar{u}_r$

This velocity component is derived similarly to that in the case of a uniformly loaded rotor. Since the average tangentially induced velocity, $\bar{u}_a$, is independent of θ', the radial velocity component, $\bar{u}_r$, is obtained by substituting from equation (62) into the equation of continuity, equation (28). After integrating and with the substitution of the boundary condition, $\bar{u}_r = 0$ at $r = 0$, this velocity is obtained as

$$\bar{u}_r = -\frac{\bar{u}_0}{r'}\left(\frac{3}{2}\right)\left\{\frac{3}{4}x'^2\ln|x'| - \frac{1}{2}r'^2\left[\frac{1}{(1+x'^2)^{3/2}} - \frac{x'^2}{(1+x'^2)^{1/2}(1+\sqrt{1+x'^2})}\right.\right.$$

$$\left.+1-\ln\left(1+\sqrt{1+x'^2}\right)\right] + \frac{3}{4}r'\sqrt{r'^2+x'^2}$$

$$\left.-\left(\frac{1}{2}r'^2+\frac{3}{4}x'^2\right)\ln\left(r'+\sqrt{r'^2+x'^2}\right)\right\} \qquad (63)$$

b. Instantaneous Induced Velocity

(i) Normal Velocity Component, u_N

The instantaneous value of this velocity component is obtained by the same superposition method utilized in deriving the time-averaged value. Referring again to Figure 5, the instantaneous normal velocity, $u_{N\dagger}$, is obtained from equation (42) as

$$u_{N\dagger} = \sum_{n=1}^{N} \left(\frac{\Gamma_\dagger \omega}{4\pi U} \left[1 + \frac{x'}{A} \right] + \frac{\Gamma_\dagger r' \sin\theta'_n}{4\pi R(x'^2 + r'^2 \sin^2\theta'_n)} \left[\frac{1 - r'\cos\theta'_n}{A} + \frac{r'\cos\theta'_n}{B} \right] \right) \qquad (64)$$

The normal velocity induced by the incremental uniform loading, $d\Gamma_i$, is similarly obtained as

$$u_{Ni} = \sum_{n=1}^{N} \left\{ \int_{r'}^{1} \frac{\Gamma_\dagger \omega d\left(\frac{R_i}{R}\right)}{4\pi U} \left[1 + \frac{x'}{\left(\left[\frac{R_i}{R}\right]^2 + x'^2 + r'^2 - 2r'\left(\frac{R_i}{R}\right)\cos\theta'_n \right)^{1/2}} \right] \right.$$

$$\left. + \int_{0}^{1} \frac{\Gamma_\dagger r' \sin\theta'_n d\left(\frac{R_i}{R}\right)}{4\pi R(x'^2 + r'^2 \sin^2\theta'_n)} \left[\frac{\left(\frac{R_i}{R}\right) - r'\cos\theta'_n}{\left(\left[\frac{R_i}{R}\right]^2 + x'^2 + r'^2 - 2r'\left(\frac{R_i}{R}\right)\cos\theta'_n \right)^{1/2}} + \frac{r'\cos\theta'_n}{(x'^2 + r'^2)^{1/2}} \right] \right\} \qquad (65)$$

It should be noted in the above equation that the second part is the velocity induced by the blade bound vortex. This velocity is not affected by the vortex boundary; hence, the integration is performed from blade root to tip where the limits are $\frac{R_i}{R} = 0$ and $\frac{R_i}{R} = 1$.

After integrating equation (65), there results

$$u_{N_i} = \sum_{n=1}^{N} \left\{ \frac{\Gamma_t \omega}{4\pi U} \left[(1-r') + x' \ln(k) \right] + \frac{\Gamma_t r' \sin\theta'_n}{4\pi R \left(x'^2 + r'^2 \sin^2\theta'_n \right)} \left[A \cdot B + \left(\frac{r' \cos\theta'_n}{B} \right) \right] \right\} \qquad (66)$$

where

$$k = \frac{1 - r'\cos\theta'_n + A}{r' \left(1 - \cos\theta'_n \right) + \left[x'^2 + 2r'^2 \left(1 - \cos\theta'_n \right) \right]^{1/2}} \qquad (67)$$

The resultant instantaneous normal induced velocity, u_N , is therefore obtained from equations (64) and (66) by the relation $u_N = u_{N_f} - u_{N_i}$. Thus,

$$u_N = \sum_{n=1}^{N} \left\{ \frac{\Gamma_f \omega}{4\pi U} \left[r' + x' \left(\frac{1}{A} - \ell n\, k \right) \right] \right.$$

$$\left. + \frac{\Gamma_f\, r' \sin\theta'_n}{4\pi R (x'^2 + r'^2 \sin^2\theta'_n)} \left[\frac{1 - r'\cos\theta'_n}{A} - A + B \right] \right\} \qquad (68)$$

(ii) Tangential Velocity Component, u_a

In deriving the instantaneous value of the tangential induced velocity, it will be assumed that the effect of the helical vortex can be neglected. Furthermore, in the case of a triangularly loaded rotor, there exists no central vortex. Hence, the instantaneous tangential velocity component, u_a , is obtained by considering only the effect of the bound vortex. Referring to Figure 5 and equation (49), the tangential velocity induced by the uniform loading, Γ_f , at point P(x,r) can be obtained as follows:

$$u_{a_f} = \sum_{n=1}^{N} - \left\{ \frac{\Gamma_f\, x' \cos\theta'_n}{4\pi R (x'^2 + r'^2 \sin^2\theta'_n)} \left[\frac{1 - r'\cos\theta'_n}{A} + \frac{r'\cos\theta'_n}{B} \right] \right\} \qquad (69)$$

The tangential velocity induced by the incremental uniform loading, $d\Gamma_i$, is similarly obtained to be

$$u_{\alpha_i} = \sum_{n=1}^{N} \left\{ \int_0^1 \frac{\Gamma_t\, x' \cos\theta'_n\, d\left(\frac{R_i}{R}\right)}{4\pi R(x'^2 + r'^2 \sin^2\theta'_n)} \left[\frac{\left(\frac{R_i}{R}\right) - r'\cos\theta'_n}{\left(\left[\frac{R_i}{R}\right]^2 + x'^2 + r'^2 - 2r'\left(\frac{R_i}{R}\right)\cos\theta'_n\right)^{1/2}} + \frac{r'\cos\theta'_n}{\left(x'^2 + r'^2\right)^{1/2}} \right] \right\} \qquad (70)$$

The integration of equation (70) yields

$$u_{\alpha_i} = -\sum_{n=1}^{N} \left[\frac{\Gamma_t\, x' \cos\theta'_n}{4\pi R\left(x'^2 + r'^2 \sin^2\theta'_n\right)} \left(\frac{r'\cos\theta'_n}{B} + A - B \right) \right] \qquad (71)$$

The resultant instantaneous tangential velocity, u_α , is therefore obtained from equations (69) and (71) from the relation $u_\alpha = u_{\alpha_t} - u_{\alpha_i}$. Thus,

$$u_\alpha = -\sum_{n=1}^{N} \left[\frac{\Gamma_t\, x' \cos\theta'_n}{4\pi R\left(x'^2 + r'^2 \sin^2\theta'_n\right)} \left(\frac{1 - r'\cos\theta'_n}{A} - A + B \right) \right] \qquad (72)$$

(iii) Radial Velocity Component, u_r

The method of superposition of uniform loadings is again utilized in deriving this induced velocity component of a triangularly loaded rotor. The radial velocities induced by the uniform loading, Γ_t , and $d\Gamma_i$, at point $P(x, r)$ can be obtained from equation (51)

as follows:

$$u_{r_f} = \frac{N\Gamma_f \omega}{8\pi U}\left[\frac{r'}{\left(1+x'^2\right)^{3/2}}\right] \tag{73}$$

$$u_{r_i} = \frac{N\Gamma_f \omega}{8\pi U}\int_{r'}^{1} \frac{\left(\frac{R_i}{R}\right)^2 r' d\left(\frac{R_i}{R}\right)}{\left[\left(\frac{R_i}{R}\right)^2 + x'^2\right]^{3/2}} \tag{74}$$

The integration of equation (74) yields

$$u_{r_i} = \frac{N\Gamma_f \omega r'}{8\pi U}\left\{-\frac{1}{\left(1+x'^2\right)^{1/2}} + \frac{r'}{\left(r'^2+x'^2\right)^{1/2}} + \ln\left[\frac{1+\left(1+x'^2\right)^{1/2}}{r'+\left(r'^2+x'^2\right)^{1/2}}\right]\right\} \tag{75}$$

Subtracting equation (75) from (73), the resultant instantaneous induced radial velocity component, u_r , becomes

$$u_r = \frac{N\Gamma_f \omega r'}{8\pi U}\left(\frac{2+x'^2}{\left(1+x'^2\right)^{3/2}} - \frac{r'}{\left(r'^2+x'^2\right)^{1/2}} - \ln\left[\frac{1+\left(1+x'^2\right)^{1/2}}{r'+\left(r'^2+x'^2\right)^{1/2}}\right]\right) \tag{76}$$

B. YAWED FLOW

The rotor in yawed flow is shown in Figure 6. It is assumed that the vortices shed from the rotor in the yawed flow condition are shed with a velocity equal to the resultant averaged velocity of the flow through the rotor. This

resultant velocity may be represented by a component, $V\cos\phi + u$, perpendicular to the rotor plane and the component, $V\sin\phi_0$, parallel to the plane. As shown in Figure 6, the rotor wake is therefore swept back at an angle χ with respect to the rotor axis, the value of χ being

$$\chi = \tan^{-1} \frac{V\sin\phi}{V\cos\phi + \bar{u}_0} \tag{77}$$

The resultant normal velocity at the rotor plane, U, in yawed flow condition is given by

$$U = V\cos\phi + \bar{u}_0 \tag{78}$$

where

$$\bar{u}_0 = \frac{T}{2\rho A\sqrt{(V\cos\phi + \bar{u}_0)^2 + (V\sin\phi)^2}} \tag{79}$$

For any given condition of flight, V and ϕ are specified; hence, $\bar{u}_0$ and U can be obtained by the simultaneous solution of equations (78) and (79).

The coordinate system defining the induced velocities in yawed flow condition is shown in Figure 7. X_1, Y_1, and Z_1 are the axes of a coordinate system with the X_1-Z_1 plane rotated an angle χ with the X-Z plane such that the X_1-axis coincides with the axis of the swept-back wake. The angular position of point P is defined by any of the following three angles, respectively:

(i) α = angle defining point P with vertex on X-axis, measured from positive Y-axis parallel to the Y-Z plane.

(ii) $\bar{\alpha}$ = angle defining point P with vertex on X_1-axis, measured from positive Y-axis parallel to the Y-Z plane.

(iii) α_1 = angle defining point P with vertex on X_1-axis parallel to the Y_1-Z_1 plane.

All angles are positive in the direction of ω. The transformation equations between the X_1, Y_1, Z_1 and X, Y, Z systems are given as follows:

$$\left.\begin{aligned} x_1 &= x - z\tan\chi \\ y_1 &= \frac{y}{\cos\chi} \\ z_1 &= x\tan\chi + z \\ r_1^2 &= \left(\frac{y}{\cos\chi}\right)^2 + \left(x\tan\chi + z\right)^2 \\ \tan\alpha_1 &= \left[\left(\frac{x}{z}\right)\sin\chi + \cos\chi\right]\tan\alpha \\ \tan\bar{\alpha} &= -\left[\frac{z + x\tan\chi}{y}\right] \end{aligned}\right\} \qquad (80)$$

The normal velocity component induced by a lifting rotor in the yawed flow condition is derived from the results of the equations in axial flow with an additional parameter χ defined by equation (77). The vortex system assumed in this case is essentially the same as that in axial flow, but located in a differenct position with respect to the rotor. The central vortex is now shed along the X_1-axis, and the helical vortex is shed down from the blade and winds around the X_1-axis. The bound vortex is fixed to the blade and

hence remains in the same position as in the case of the axial flow condition. The velocities induced by these three line vortices are discussed separately as follows:

a. Normal Velocity Induced by the Trailing Helical Vortex

It has been shown in Reference 4 that the normal velocity induced by the trailing vortex at point P, defined by the coordinates $(x_1', r_1', \bar{\alpha})$ in the slipstream of a rotor yawed at an angle χ, is equivalent to the induced velocity existing at the corresponding point $(x' = x_1', r' = r_1', \alpha = \bar{\alpha})$ in an unyawed rotor multiplied by $\cos\chi$. This can be expressed as

$$u_{x_h}(x_1', r_1', \bar{\alpha})_{\chi=\chi} = \cos\chi \left[u_{x_h}(x'=x_1', r'=r_1', \alpha=\bar{\alpha})_{\chi=0} \right] \tag{81}$$

where

$$\left.\begin{aligned} x_1' &= \frac{x_1}{R} \\ r_1' &= \frac{r_1}{R} \end{aligned}\right\} \tag{82}$$

$$R_1^2 = R^2 (1 - \sin^2\bar{\alpha} \sin^2\chi) \tag{83}$$

According to equation (81) and given the coordinates x_1, r_1, and $\bar{\alpha}$ of a given point P in the rotor wake and the wake angle χ, the normal velocity induced by the helical vortex of a yawed rotor at that point can therefore be obtained from the expression derived for the axial flow condition.

b. Velocity Induced by the Central Vortex

In axial flow condition, the central vortex is shed along the X-axis. The velocity induced by the central vortex is therefore in the tangential direction and does not contribute to the normal velocity induced in the rotor wake. In yawed flow condition, however, the central vortex is shed along the X_1-axis, and the velocity induced has a component along the normal direction or the X-axis. This component is given as follows:

$$u_{N_C} = u_{\alpha_1} \cos\alpha_1 \sin X \tag{84}$$

where u_{α_1} is the total velocity induced by the central vortex, and u_{N_C} is the velocity component along the X-axis.

The total induced velocity, u_{α_1}, at point $P(r_1', x_1', \bar{\alpha})$ can be expressed similar to equation (26), as follows:

$$u_{\alpha_1} = -\frac{N\Gamma}{4\pi R r_1'}\left[\frac{x_1'}{\left(x_1'^2 + r_1'^2\right)^{1/2}} + 1\right] \tag{85}$$

Substituting equation (85) into (84) yields the normal component of u_{α_1} along the X-axis:

$$u_{N_C} = -\frac{N\Gamma\cos\alpha_1 \sin X}{4\pi R r_1'}\left(\frac{x'}{B_1} + 1\right) \tag{86}$$

where

$$B_1 = \left(x_1'^2 + r_1'^2\right)^{1/2}$$

c. Velocity Induced by the Bound Vortex

Since the position of the bound vortex is not affected by the yawed flow, the bound vortex-induced velocity derived in axial flow condition is directly applicable in yawed flow condition.

From the above consideration, the normal velocity induced at any point in the wake of a rotor in yawed flight condition can be obtained from those expressions derived for the axial flow condition by introducing a new set of position parameters defining that point and the yawed wake. These parameters are x_1', r_1', α_1, $\bar{\alpha}$, and χ. For a given condition of flight, these parameters can be readily calculated by equations (77), (80), and (82).

1. Uniform Disk Loading

a. Time-Averaged, Normal Induced Velocity $\bar{u}_N$

According to equations (81) and (22), the time-averaged, normal induced velocity, $\bar{u}_N$, can be expressed as follows:

$$\bar{u}_N = \frac{T\cos\chi}{2\rho\pi R^2 U}\left[1+\frac{2x_1'}{\pi b_1}K(k_1)\right] \qquad (87)$$

where b_1 and k_1 are given in equations (16) and (18) in terms of x_1' and r_1'.

From equations (77) and (78), $\cos\chi$ can be expressed as

$$\cos\chi = \frac{U}{\sqrt{(V\sin\phi)^2 + (V\cos\phi + \bar{u}_0)^2}} \tag{88}$$

Substituting equation (88) into (87), we have

$$\bar{u}_N = \frac{T}{2\rho\pi R^2\sqrt{(V\sin\phi)^2 + (V\cos\phi + \bar{u}_0)^2}}\left[1 + \frac{2x_1'}{\pi b_1} K(k_1)\right] \tag{89}$$

Substituting $\bar{u}_0$ of equation (79) into equation (89) and utilizing the approximation, $u_N(r_1', x_1') = u_N(r_1' = 0, x_1')$, equation (89) becomes

$$\bar{u}_N = \bar{u}_0\left[1 + \frac{x_1'}{(1+x_1')^{1/2}}\right] \tag{90}$$

b. Instantaneous Normal Induced Velocity

In the axial flow condition, this velocity component is given by equation (42). In this equation, the first part gives the velocity induced by the helical vortex, whereas the second part gives the velocity induced by the bound vortex. In the yawed flow condition, the bound vortex effect, u_{N_b}, remains the same. Thus,

$$u_{N_b} = \sum_{n=1}^{N} \frac{\Gamma r'\sin\theta_n'}{4\pi R\left(x'^2 + r'^2\sin^2\theta'\right)}\left[\frac{1 - r'\cos\theta_n'}{A} + \frac{r'\cos\theta_n'}{B}\right] \tag{91}$$

The normal velocity induced by the helical vortex, u_{N_h} , however, becomes:

$$u_{N_h} = \sum_{n=1}^{N} \frac{\Gamma \omega \cos\chi}{4\pi U} \left[1 + \frac{x_1'}{A_1} \right] \tag{92}$$

where

$$A_1 = (1 + x_1'^2 + r_1'^2 - 2r_1' \cos\bar{\theta}_n)^{1/2}$$

and

$$\bar{\theta}_n = \theta_n - \bar{\alpha}$$

In addition, the normal component of the central vortex-induced velocity, u_{N_c} , given in equation (86) must be included. The total normal induced velocity in yawed flow condition, u_N , can therefore be obtained as follows:

$$u_N = u_{N_h} + u_{N_b} + u_{N_c}$$

$$u_N = \sum_{n=1}^{N} \frac{\Gamma \omega \cos\chi}{4\pi U} \left[1 + \frac{x_1'}{A_1} \right] + \frac{\Gamma r' \sin\theta_n'}{4\pi R \left(x^2 + r^2 \sin^2\theta_n' \right)} \left[\frac{1 - r' \cos\theta_n'}{A} \right.$$

$$\left. + \frac{r' \cos\theta_n'}{B} \right] - \frac{N\Gamma \cos\alpha_1 \sin\chi}{4\pi R r_1'} \left[\frac{x_1'}{B_1} + 1 \right] \tag{93}$$

2. Triangular Disk Loading

The velocity induced by a triangularly loaded rotor in yawed flight condition can be obtained from those results derived for axial flight condition in exactly the same way as in the case of the uniformly loaded rotor previously discussed. However, the normal velocity induced by the central vortex, u_{N_C}, is neglected in this case due to the fact that for a triangularly loaded rotor there no longer exists a central vortex. The time-averaged and instantaneous normal induced velocity components are thus obtained from equations (62) and (68), respectively, and are presented below.

a. Time-Averaged, Normal Induced Velocity, $\bar{u}_N$

$$\bar{u}_N = \left(\frac{3}{2}\right)\bar{u}_0\left[r_1' + x_1'\left(\frac{1}{\sqrt{1+x_1'^2}} - \ln\frac{1+\sqrt{1+x_1'^2}}{r_1'+\sqrt{r_1'^2+x_1'^2}}\right)\right] \tag{94}$$

where $\bar{u}_0$ is given in equation (79).

b. Instantaneous Normal Induced Velocity, u_N

$$u_N = \sum_{n=1}^{N} \frac{\Gamma_t \omega \cos\chi}{4\pi U}\left[r_1' + x_1'\left(\frac{1}{A_1} - \ln k_1\right)\right]$$

$$+ \frac{\Gamma_t r' \sin\theta_n'}{4\pi R\left(x'^2 + r'^2 \sin^2\theta_n'\right)}\left[\frac{1 - r'\cos\theta_n'}{A} - A + B\right] \tag{95}$$

where

$$k_1 = \frac{1 - r_1' \cos\bar{\theta}_n + A_1}{r_1'\left(1-\cos\bar{\theta}_n\right) + \left(x_1'^2 + 2r_1'^2\left[1-\cos\bar{\theta}_n\right]\right)^{1/2}} \tag{96}$$

C. FUSELAGE EFFECTS

The effect of the fuselage on the induced velocities inside the rotor wake is derived here for uniformly loaded and triangularly loaded rotors in the axial flow condition. The fuselage is represented by a three-dimensional doublet placed in the nonuniform flow field corresponding to the time-averaged, axial-induced velocity in the rotor wake. Using this flow pattern, the strength of the doublet is determined, and the zero streamline of the flow corresponding to the fuselage shape is established. The velocity at a given point in the rotor wake can be computed by the superposition of the velocity induced by the rotor and that induced by the doublet of strength M. In the case of a triangularly loaded rotor, there is an upwash velocity region near the rotor axis and immediately below the rotor plane, as predicted by the flow field analysis of a free rotor. The present analysis of the fuselage effect is applicable only when the fuselage is placed within this upwash region.

1. Uniform Loading

The time-averaged, normal induced velocity in the wake of a free rotor is given in equation (29) as follows:

$$\bar{u}_N = \bar{u}_0\left[1 + \frac{x'}{\sqrt{1+x'^2}}\right] \tag{97}$$

The flow represented by equation (97) in the rotor wake is axisymmetric with respect to the rotor axis. The stream function for such a flow is defined as

$$\bar{u}_N = \frac{1}{2\pi R^2 r'} \left(\frac{\partial \psi_n}{\partial r'} \right) \tag{98}$$

Substituting equation (97) into (98) yields

$$\bar{u}_0 \left(1 + \frac{x'}{\sqrt{1 + x'^2}} \right) = \frac{1}{2\pi R^2 r'} \left(\frac{\partial \psi_n}{\partial r'} \right) \tag{99}$$

Transforming equation (99) into the coordinate system fixed to the fuselage center of gravity shown in Figure 8 yields

$$\bar{u}_0 \left(1 + \frac{(h' + \bar{x}')}{\sqrt{1 + (h' + \bar{x}')^2}} \right) = \frac{1}{2\pi R^2 r'} \left(\frac{\partial \psi_n}{\partial r'} \right) \tag{100}$$

where

$$h' = \frac{h}{R}$$

$$\bar{x}' = \frac{\bar{x}}{R}$$

Integrating the above equation, we have

$$\psi_n = \pi R^2 \bar{u}_0 r'^2 \left[1 + \frac{(h' + \bar{x}')}{\sqrt{1 + (h' + \bar{x}')^2}} \right] \tag{101}$$

Equation (101) represents the stream function of the induced flow inside the wake of a free lifting rotor. The fuselage is now replaced by a three-dimensional doublet located at the center of gravity of the fuselage. Its stream function is given by

$$\psi_d = -\frac{M}{2R}\left(\frac{\sin^2\beta}{s'}\right) \tag{102}$$

where

$$s' = \frac{s}{R}$$

and s is the radial distance measured from the fuselage center of gravity to the point in space.

Combining equations (101) and (102) gives the total stream function inside the wake. Thus,

$$\psi = \psi_n + \psi_0 = -\frac{M}{2R}\left(\frac{\sin^2\beta}{s'}\right) + \pi R^2 \bar{u}_0 r'^2 \left[1 + \frac{(h' + \bar{x}')}{\sqrt{1 + (h' + \bar{x}')^2}}\right] \tag{103}$$

The zero streamline of the flow is obtained from equation (103) letting $\psi = 0$, which yields

$$\frac{M}{2R}\left(\frac{1}{s'^3}\right) - \pi R^2 \bar{u}_0 \left[1 + \frac{(h' + s'\cos\beta)}{\sqrt{1 + (h' + s'\cos\beta)^2}}\right] = 0 \tag{104}$$

It is found in the above equation that s varies only slightly with β . Equation (104) can therefore be simplified by letting $\cos\beta = 0$. Thus,

$$\frac{M}{2R}\left(\frac{1}{s'^3}\right) - \pi R^2 \bar{u}_0\left[1+\frac{h'}{\sqrt{1+h'^2}}\right] = 0 \qquad (105)$$

For an assumed spherical fuselage of radius a, represented by the above zero streamline, the strength M of the three-dimensional doublet is calculated from equation (105) by the substitution S' = a' , where a' = a/R.

$$M = 2\pi R^3 a'^3 \bar{u}_0\left(1+\frac{h'}{\sqrt{1+h'^2}}\right) \qquad (106)$$

Substituting equation (106) into (104) yields the zero streamline or the approximated fuselage shape as follows:

$$\cos\beta = \frac{h'}{s'} - \frac{K\left(\frac{a'^3}{s'^3}\right) - 1}{\left(\frac{Ka'^3}{s'}\left[2-K\left(\frac{a'^3}{s'^3}\right)\right]\right)^{1/2}} \qquad (107)$$

where

$$K = 1 + \frac{h'}{\sqrt{1+h'^2}}$$

The normal velocity induced by the doublet of strength M given in equation (106) can be expressed in terms of its stream function as follows:

$$\bar{u}_{x_d} = \frac{1}{2\pi R^2 r'} \frac{\partial \psi_d}{\partial r'} \tag{108}$$

Substituting equation (102) into (108) yields

$$\bar{u}_{x_d} = -\frac{M}{2\pi R^3} \left[\frac{\bar{x}'^2 - \frac{1}{2} r'^2}{\left(\bar{x}'^2 + r'^2\right)^{5/2}} \right]$$

$$= -\frac{M}{2\pi R^3} \left\{ \frac{\left(x'-h'\right)^2 - \frac{1}{2} r'^2}{\left[\left(x'-h'\right)^2 + r'^2\right]^{5/2}} \right\} \tag{109}$$

For a given fuselage of equivalent radius, a, the doublet representing this assumed fuselage is defined by its strength M, given in equation (106). The normal velocity induced in the rotor is obtained simply by adding the velocity induced by the free rotor and that induced by the doublet given in equation (109). Though equation (109) is derived from time-averaged, induced velocity, it is assumed to be applicable also for instantaneous velocity induced inside the rotor wake.

2. Triangular Loading

As previously stated, this analysis of the fuselage effect for the case of triangular loading is applicable only when the fuselage is placed within the upwash region near the rotor axis. This is due to the fact that the zero streamline of the combined flow, that due to the free rotor and the assumed doublet, is no longer a closed surface where reverse flow exists. The fuselage shape therefore cannot be established in this case. However, if the equivalent radius of the fuselage, a, is within the upwash region, the fuselage effect can be analyzed similar to the case of uniform loading.

The normal average velocity induced by a triangularly loaded rotor is given in equation (62) as

$$\bar{u}_x = \frac{3}{2}\bar{u}_0\left[r' + x'\left[-\frac{1}{\sqrt{1+x'^2}} - \ln\left(\frac{1+\sqrt{1+x'^2}}{r'+\sqrt{r'^2+x'^2}}\right)\right]\right] \tag{110}$$

where

$$x' = (h' + \bar{x}')$$

The upwash region can be easily determined by computing a value of r' from equation (110) corresponding to the condition $\bar{u}_x = 0$ at $\bar{x}' = 0$. If $a' \leq$ the computed value of r', then the following analysis is applicable.

The combined stream function of the flow induced by the free rotor and the doublet located on the rotor axis at the fuselage center of gravity is derived similar to that of uniform loading and is obtained as follows:

$$\psi = -\frac{M}{2R}\left[\frac{r'^2}{\left(r'^2+\bar{x}'^2\right)^{3/2}}\right] + \frac{3}{2}(2\pi)\bar{u}_0 R^2\left\{\frac{r'^3}{3} + \frac{(h'+\bar{x}')r'^2}{2\sqrt{(h'+\bar{x}')^2+1}}\right.$$

$$-\frac{(h'+\bar{x}')}{2}r'^2\ln\left(1+\sqrt{1+(h'+\bar{x}')^2}\right) + (h'+\bar{x}')\left[\left(\frac{r'^2}{2}+\frac{(h'+\bar{x}')^2}{4}\right)\right.$$

$$\left.\ln\left[r'+\sqrt{r'^2+(h'+\bar{x}')^2}\right] - r'\frac{\sqrt{r'^2+(h'+\bar{x}')^2}}{4}\right]$$

$$\left.-\frac{(h'+\bar{x}')^3\ln(h'+\bar{x}')}{4}\right\} \tag{111}$$

For $\psi = 0$, $\bar{x}' = 0$, and $r' = a'$, the strength of the doublet, M, is obtained graphically from equation (111). Once the strength of the doublet is defined, the velocity induced by the doublet is calculated from equation (109), and the total induced velocity at a given point in the rotor wake is computed by the superposition of the velocity induced by the rotor and that induced by the doublet.

D. GROUND EFFECT

A lift device operating in the proximity of the ground experiences a reduction in the induced velocity. An indication of the reduction of the magnitude of the time-averaged, normal induced velocity is shown in test data such as those in References 7 and 8. In order to account for this reduction, a correction factor, k_g, has been obtained empirically by use of the data given in the above two references. This factor is obtained as

$$k_g = 1 - 0.9e^{-2\frac{H}{R}} \tag{112}$$

The induced velocity in ground effect can then be computed from the out-of-ground value as follows:

$$u_{IGE} = k_g u_{OGE} \tag{113}$$

E. WAKE CONTRACTION

The analysis presented above incorporates the assumptions that the vortices shed at any point from the blade remain at a constant strength with time and form a helical path on a cylinder of constant radius. The latter assumption implies that the effect of wake contraction is neglected. Wake contraction is only of minor importance in high forward or

climbing speed conditions, but it is a significant factor in the hovering flight condition.

One method of including the effect of rotor contraction for the hovering flight condition consists simply of assuming that the induced velocities at any radial location r/R can be computed on the basis of the local wake radius, R_e, i.e., $u\left(\frac{r}{R}\right)_{CORR} = u\left(\frac{r}{R_e}\right)$. A more logical method of accounting for wake contraction is illustrated in Figure 9. The induced velocities at any point experience the strongest effect by those vortices which are nearest to them. Let it therefore be assumed, in order to obtain the velocities at a point $P_1(x_1/R_1, r_1/R)$, that the outer radius of the cylinder which incloses the shed vortices is equal to that of the local wake radius, $R_e(X_1)$. Referring again to Figure 9, this then implies that the distance between the point P_1 and A, located at an axial position smaller than X_1, is larger than that used in the calculations. On the other hand, the distance between the point P_1 and the vortex element B, located at an axial position longer than X_1, is smaller than that used in the calculations.

The induced velocities can then be computed using the previous theory by replacing R by R_e, i.e.,

$$u\left(\frac{x_1}{R}, \frac{r_1}{R}\right)_{CORRECTED} = u\left(\frac{x_1}{R_e}, \frac{r_1}{R_e}\right) \tag{114}$$

The values of R_e can be obtained from experimental data, such as those presented in Reference 9.

III. THE TEST PROGRAM

Experimental data were obtained for both instantaneous and time-averaged, induced velocities for several flight conditions of a full-scale helicopter. The details of the test program are described in this section.

A. TEST HELICOPTER

The aircraft utilized for the test program was a commercial Hughes helicopter, Model 269-A (Army designation TH-55A). This helicopter was chosen for this program for the following reasons:

1. Low vibration and noise levels.
2. Adequate cabin room for recording instrumentation.
3. Unobstructed 360° visibility in cabin.
4. Compact in size.
5. Acceptable handling qualities in hovering and forward flight.
6. Small fuselage size to minimize fuselage effects.

Table I presents the principal dimensions and physical characteristics of the Hughes 269-A test helicopter.

B. TEST INSTALLATION

The test rig utilized to measure rotor velocities is shown mounted on the test helicopter in Figure 10. The test rig consists of a rectangular frame with its vertical members parallel to the rotor shaft. Attached to the vertical members of the frame are two horizontal booms (one on each side of the helicopter), upon which are mounted the probes which measure time-averaged and instantaneous induced velocities.

1. Support Structure

The boom support structure, a space framework, was attached to the helicopter at existing hard points, i.e., the rotor mast shelf, skid gear cross beam, and the tail cone fuselage cluster, with a minimum amount of alteration to the existing structure.

The rotor mast shelf was backed up with an additional shelf structure that was attached by picking up existing rivet patterns. This shelf backup supported the upper portion of the forward vertical columns. The lower supports for these columns were provided by modifying the step structure which replaced the existing steps. The aft support for the framework was accomplished with a clamp collar that fitted the tail boom at the fuselage. The structure installation is shown in Figure 11.

2. Instrument Support Booms

The velocity probe booms were attached to the vertical support columns with clamp fittings to allow for changes in azimuth and height positions. The booms were fixed in azimuth position with additional tube structure, as shown in Figure 11. The booms span approximately 90 percent of the rotor radius. The natural frequency of the booms was measured to assure that it did not coincide with the rotor harmonics. The maximum vertical test height of the probe from the rotor blades was based on a blade tip to tail boom clearance of 12.0 inches, as established by structural considerations. The horizontal support booms could be moved aft of the rotor shaft and fixed in the required position for recording data in skewed wakes generated at forward speeds.

C. INSTRUMENTATION

A block diagram of the instrumentation system utilized to obtain the required data is shown in Figure 12. This system includes data sensing, recording, and playback equipment.

1. Data Sensing Equipment

a. Time-Varying Velocities

Two-dimensional "X" configuration quartz-coated cylindrical hot film sensors (mounted on 6-inch-stem-length probes) were utilized to sense the rotor wake time-varying induced velocities. The principle of operation is the same as that of a hot wire sensor.

The hot film sensors with a .006-inch diameter and a .125-inch length, Model TSI-DYN, were made by Thermo-Systems Incorporated. The sensors were mounted on the horizontal booms adjacent to the three-dimensional pitot probes for correlation. A typical installation is shown in Figure 13.

The sensors are designed for use with a constant-temperature anemometer circuit, which measures the instantaneous heat transfer rate between the heated sensor and the surrounding air. The circuit includes an electrical current through the sensor to correspond to the cooling effect of the flowing air while maintaining the sensor at a constant resistance and temperature.

These six anemometer circuits were packaged in module form and were supplied with DC power from a Thermo-Systems module power supply. In order to reduce system weight, a time-sharing system of anemometer modules was used. As will be discussed subsequently, three probes (six channels of data) on one side of the helicopter (left boom) were used through the anemometer circuits fed through voltage-controlled oscillators, multiplexed, and recorded for 30 seconds. Then by electronic switching, the three probes on the other side of the helicopter (right boom) were fed through the same anemometer circuits and recorded for the next 30 seconds.

b. Steady-State Velocities

Three-dimensional, directional pitot probes, United Sensor and Control Corporation Model DA-125 modified, were used to measure time-averaged velocities. The probes with a stem length of 6 inches and 1/8-inch diameter have a five-hole, prism-shaped measuring

head. The installation of a three-dimensional probe is shown in Figure 13.

c. Flight Parameters

(i) Altitude - An absolute pressure transducer, Statham Model P968-154-350, was used for altitude sensing. Installation of this unit is shown in Figure 14.

(ii) Airspeed - A differential pressure transducer, Statham Model PM96TC±.5-350, was used for sensing airspeed. This unit was coupled into the existing pressure lines of the test vehicle airspeed system. Installation is shown in Figure 14.

(iii) Normal Acceleration - A Statham temperature-controlled linear accelerometer, Model AJ17-1-350, was used to measure the normal acceleration of the test vehicle. The range of the instrument is ±1.0 g, and it has a natural frequency of 35 c.p.s. Structural accommodation necessitated that the accelerometer be mounted on the aft gear cross strut (station 116). Location of the accelerometer is shown in Figure 11.

(iv) Engine r.p.m. - An Electro Products Laboratories electromagnetic pickup, Model 3015A, was used to monitor the engine speed at the output shaft. Magnetic field interruption at 1/rev. was provided by an existing tab washer on the shaft. The installation is shown in Figure 15.

(v) Rotor r.p.m. - The sensor used for the measurement was the same type as that for measuring engine r.p.m. Field interruption at 3/rev. was provided by an arm on the rotating swash plate. The installation is shown in Figure 16.

(vi) Manifold Pressure - An absolute pressure transducer, Statham Model PA208TC-15-350,

was used to measure the manifold pressure. This unit was coupled into the existing manifold pressure line in the helicopter. The installation is shown in Figure 14.

(vii) Fuselage Pitch Attitude - An attitude gyro, Giannini Model 3111C-1, was used to measure the fuselage pitch attitude. This unit was installed on the pilot side of the cabin floor, as shown in Figure 17.

(viii) Longitudinal Cyclic Displacement - A position indicator, Lockheed Model WR8, was used to measure the longitudinal cyclic control input in inches of stick travel. The transducer was mounted on the cabin floor and coupled to the long cyclic control shaft.

(ix) Collective Stick Displacement - The transducer used for this measurement is the same as that used for the longitudinal cyclic. The transducer was mounted on the pylon shelf and tied to the extension shaft of the collective stick as shown in Figure 14.

2. Data Recording Equipment

a. Hot Film Data

A two-track tape recorder, Viking Model 230, was utilized to record the multiplexed, time-varying velocity data on magnetic tape. Figure 18 shows the recorder installation. As was previously mentioned, the six, two-component velocity sensors comprising twelve data channels were time-shared. This reduced the amount of circuitry required, thereby reducing the required size of the recording instrumentation package. The switching circuitry, anemometer modules, and tape recorder package are shown in Figure 19.

b. Time-Averaged Pressure Data

A 32-tube inclined manometer bank photo panel was used to depict the time-averaged pressure data sensed by the three-dimensional pressure probes positioned in the rotor downwash. These data were recorded by the use of a Graphlex camera equipped to handle Polaroid film. Figure 18 shows the manometer box installation in the helicopter.

c. Oscillograph

A recording oscillograph, Century Electronics Corporation Model 409E, coupled to a Century Model 1809 bridge control unit, was used for recording the flight parameters given on page 48. The paper speed used was from 10 in./sec. to 1/2 in./sec., depending upon the tests. Figure 17 shows the oscillograph installation.

3. Calibration of Instrumentation

a. Transducer Bench Calibration

A summary of the transducer calibration is presented in Table II. The transducer bench calibration was performed as follows:

(i) Altitude

Static calibrations were performed by utilizing a vacuum pump and a barometer. The calibration curve is shown in Figure 20.

(ii) Airspeed

Airspeed calibrations were performed on the pressure transducer utilizing a variable pressure air supply and a manometer. The calibration curve is shown in Figure 21.

(iii) Normal C.G. Accelerometer

Static calibration was obtained by measuring the accelerometer output for the normal and inverted positions. Zero output was obtained by placing the accelerometer on its side normal to the direction of excitation. The calibration is shown in Figure 22.

(iv) Rotor r.p.m., Engine r.p.m.

No calibrations were conducted since outputs were read off the oscillogram as interruptions per unit time.

(v) Manifold Pressure

The manifold pressure transducer was calibrated using a vacuum pump and a manometer. The calibration is shown in Figure 23.

(vi) Pitch Attitude Gyro

Static calibrations were performed on an attitude table for several angles with a range of $\pm 16°$. The calibration curve is shown in Figure 24.

(vii) Collective Pitch and Cyclic Stick Displacement

The electrical output of the potentiometer bridge circuit versus stick motion was measured on the helicopter for both control sticks by displacement of the control sticks from one extreme to the other. The calibration curves of the collective and cyclic stick are shown in Figures 25 and 26, respectively.

(viii) Hot Film Anemometer

The anemometer system was bench-calibrated

using the probe calibrator, Thermo-Systems Model 1125, for a velocity ranging from 0 to 5000 f.p.m. The probe calibrator consists of a pressure chamber of low turbulence supplied with high-pressure air and a test nozzle. The probe to be calibrated is placed at the nozzle, and velocities are applied by adjusting a pressure valve on the high-pressure air input. The velocity at the probe (or nozzle) is measured on an inclined manometer. The voltage-controlled oscillators (VCO's) were set to measure center frequency at 3000 f.p.m., in order to obtain the best operation in the useable portion of the VCO's. The probe output voltage per channel was measured with a Fluke meter and plotted versus f.p.m. Hot film calibrations are given in Figures 27 through 32.

(ix) Three-Dimensional Pitot Sensors

The United Sensor three-dimensional pressure probes were calibrated by the manufacturer. A typical set of calibration curves is shown in Figures 33 through 35.

b. System Calibration and Operation

Ground calibration of the helicopter instrumentation was conducted prior to each sequence of flight tests. All systems were turned on, set on standby, and allowed a 30-minute warm-up period to stabilize the transducer circuits. All transducer outputs were recorded by the Century oscillograph with the exception of the probes.

Those transducers monitored with the oscillograph were resistance-calibrated using the manual triggering circuit of the Model 1809 Bridge control unit. There was no resistance calibration for the r.p.m. circuits since they were self-energizing. The anemometer circuits were calibrated for zero velocity over the probes using manual triggering of the individual circuits. The calibrations were recorded on magnetic tape.

The instrumentation system was manually activated prior to the test flights. Once the helicopter had become stable in the airborne test condition, a remote control switch on the cyclic stick was pilot-actuated to operate the recorders. Turning the recorders off at termination of the test actuated the automatic Rcal sequencing switch, thereby giving in-flight resistance calibration.

D. TEST PROCEDURES

The complete test program is presented in Table III. The test procedure for each flight test condition was as follows:

1. Evaluation of Helicopter Gross Weight

The empty weight and balance of the instrumented helicopter were determined from actual weight reactions measured at the prescribed jack points. The maximum gross weight attainable within the center of gravity limits was then calculated. A typical weight and balance statement is shown in Table III for the balance diagram in Figure 36.

Prior to each day of flight tests, and as determined by the cumulative number of test hours completed, the fuel load was topped off, giving a known test gross weight. Having the known gross weight, the total elapsed time, and the required gallons of fuel to fill the tank for the given number of hours flown, an average fuel consumption rate was calculated for determination of test gross weight per flight. The flight test configurations tabulated in Table IV were conducted at a nominal gross weight of 1600 pounds. The pressure probes and hot film sensors were aligned as shown in Figure 13.

2. Checkout of Instrumentation

The instrumentation recorders and the transducer bridge circuits were subjected to a 1/2-hour warm-up period to stabilize the circuitry. Instrument zeros and resistance calibrations were then measured and manually recorded. The zeros and resistance calibrations were conducted prior to each test flight.

The instrumentation was activated by ground personnel prior to each flight, and the instrument recorders were activated during flight by a toggle switch which was attached to the cyclic control stick. The recording sequence conducted by the pilot was as follows:

a. Activate recorders by placing switch in up position.

b. After a period of approximately 30 seconds, as advised by ground control, move switch to full-down position to activate photo manometer camera.

c. Immediately return switch to full-up position; record for 30 seconds.

d. Return switch to off position. Returning the switch to off position activated a time-delay relay, allowing the resistance calibration auto-sequencing switch to complete its full cycle.

At the termination of each test, the transducer and Rcal zeros were recorded manually. The magnetic tape footage used during each test was also recorded.

3. Flight Test Procedure

a. Hovering Out of Ground Effect

The measurements of instantaneous and average induced velocities were made at the specified flight conditions, at three vertical locations and six azimuthal positions. The measurements were investigated simultaneously with time-sharing, as discussed in Section III. C. Longitudinal and lateral balance was provided by testing azimuthal position 1A with 1R, 2A with 2R, and 3A with 3R, as shown in Figure 37. The test rig was mounted along the centerline of the helicopter lateral axis, parallel to the rotor shaft. The horizontal booms were fixed in vertical position I and azimuthal positions 1A and 1R. The helicopter then ascended to the test altitude of 5000 feet. When the helicopter was trimmed out at a steady-state hovering condition, the data were taken. The helicopter then landed for the next test.

While on the ground, the horizontal booms were rotated and fixed in azimuthal positions 2A and 2R at the same vertical position I, and the complete procedure was repeated. These series were repeated for different vertical heights and azimuthal positions, as given in Table IV.

b. Hovering In Ground Effect

An indexed drag chain attached to the skid was used as a visual reference to determine altitude during hovering tests while in ground effect. Thus, the ground observer, in audio control with the pilot, was able to direct his hovering altitude. Hovering altitudes of zero, 3, and 7 feet were used for testing, as shown in Table IV. The procedure and data obtained are similar to those of the OGE tests.

c. Forward Speed

The test procedure for forward speed was essentially the same as that for hovering. Since in forward flight the rotor wake was skewed at an angle to the vertical shaft line, the test rig was moved to longitudinal station II in order to obtain measurement in the rotor wake.

4. Flight Test Log

A flight test data sheet, as shown in Figure 38, was logged for each test giving the flight number, weather, configuration, helicopter parameters, estimated gross weight, and elapsed time of the test. The helicopter parameters were obtained from the pilot via radio communication during flight. However, this practice was discontinued partway through the hovering test sequence at the request of the field control tower. Subsequent data was received from the pilot at the termination of each test.

For each of the flight conditions described in item (3) above, the following helicopter flight parameters were recorded:

a. altitude
b. airspeed
c. normal acceleration
d. engine r.p.m.
e. main rotor r.p.m.
f. manifold pressure
g. fuselage pitch altitude
h. longitudinal cyclic stick position
i. collective pitch stick position

E. DATA REDUCTION

1. Time-Varying Velocities

The hot film anemometer signal data were obtained from the magnetic tape by playing the multiplexed signals through a selector bandswitching discriminator, Sonex Model 34, and by recording the selected channel output with a Brush recorder, Model Mark II.

The discriminator center frequency settings used were those set during the bench test calibrations. A fluke meter was used to set the zero-velocity output levels.

Two Brush recorder speeds were used in the data recovery. All test data obtained were reduced at a paper speed of 2.0 mm./sec.; selected tests were recorded at 50.0 mm./sec. to facilitate frequency and peak measurements of the flow velocity. Typical Brush recordings are shown in Figure 39. The characteristics of the flow field can be obtained as follows, referring to Figure 39:

> The readings obtained from channels 1 and 2 at a time t_1 from the correlation pulse are 3.7 and 3.9 volts, respectively. As can be seen from the calibration curves for this probe, Figure 27, zero velocity is represented by a 5-volt level; therefore, the velocity voltages for channels 1 and 2 would be 5 volts-2.5 volts and 5 volts-3.9 volts or 2.5 and 1.1 volts, respectively. These voltages represent velocities of 600 ft./min. and 1300 ft./min. for channels 1 and 2, as obtained from Figure 27. The instantaneous velocity at t_1 is given by

$$V = \sqrt{V_1^2 + V_2^2}$$

$$= \sqrt{600^2 + 1300^2}$$

$$= 1430 \text{ ft/min}$$

2. Steady-State Velocities

The three-dimensional probe data were recovered from measurements of the manometer tube fluid levels recorded on Polaroid film. A typical data photograph is shown in Figure 40. The data were processed by the following equation to obtain flow directions and average pressure:

Measured values uncorrected for manometer board incliniation:

P_1 1.0

P_2 -0.27

P_3 0.378

P_4 0.97

P_5 0.594

The yaw angle ϕ is determined from the ratio

$$\frac{P_2 - P_3}{P_1 - \bar{P}} = 0.685$$

where

$$\bar{P} = \frac{P_2 + P_3}{2}$$

$$= 0.054 \qquad (115)$$

Referring this ratio to the typical calibration curve in Figure 33, the yaw angle ϕ is found to be -12.0°. The pitch angle θ is determined from the ratio

$$\frac{P_4 - P_5}{P_1 - \bar{P}} = 0.397 \qquad (116)$$

Referring this ratio to the calibration curve in Figure 34 and using the above angle ϕ , the pitch angle θ is found to be -12.8°.

The dynamic pressure coefficient q was determined from the ratio

$$\frac{P_0 - P}{P_1 - \bar{P}} \qquad (117)$$

where

$$q = P_0 - P \qquad (118)$$

Having the values of θ and ϕ, the ratio for equation (117) was found to be 1.23 from Figure 35.

The test dynamic pressure $\bar{q}$ was calculated from

$$\bar{q} = A q S_f \rho\omega \tag{119}$$

where

A = correction factor for manometer inclination of 30° = 1/2

q = 1.162

S_f = specific gravity of fluid = .826

ρ_ω = density of water

Thus,

$$\bar{q} = 3.0 \text{ lb./ft.}^2$$

The velocity is given by

$$V = \sqrt{\frac{2}{\rho}\bar{q}} \tag{120}$$

where

$$\rho = \rho_0 \left(\frac{T_0}{T}\right)^{1/2} \tag{121}$$

The velocity is calculated to be

$$V = \sqrt{\frac{2}{.00238}(3.0)}$$

$$= 50.2 \text{ ft/sec} \quad \text{for } T = 75°F$$

3. Helicopter Parameters

The transducer data measurements of the helicopter parameters were recorded with the Century oscillograph. The resulting oscillograms were reduced in the conventional manner using the calibration data in Table II and in Figures 20 through 26, as applicable, and corrected for Rcal deflections in a given test. A typical oscillogram is shown in Figure 41.

IV. TEST RESULTS AND CORRELATION WITH THEORY

A. HOVERING OUT OF GROUND EFFECT

1. Experimental Data

The results of the hovering tests out of ground effect are presented in Figures 42, 43, and 44. Pressure data as well as time-averaged hot film data are also included in these figures. The induced velocity components presented are nondimensionalized by the average normal induced velocity at the rotor center, $\bar{u}_0$, as given by equati n (79).

The normal induced velocity ratio, $\bar{u}_N/\bar{u}_0$, is seen to increase with radial distance, r/R. The magnitude at any radial distance is seen to increase with axial distance aft of the rotor, x/R. Maximum values of 2.0 $\bar{u}_0$ were measured. The different values of the data for different azimuth positions are believed to be due to the ambient wind conditions encountered during the tests. The time-averaged hot film data indicate similar variations with r/R, but are of lower magnitude than the data obtained from the pressure measurements. In part, this may be due to the fact that the hot film probes are two-dimensional as compared to the three-dimensional pressure probes. The magnitude of the tangential induced velocities is on the order of 0.1. The critical effect of ambient wind conditions limited the quantity of useful data. The negative sign of the tangential induced velocities indicates that the rotor wake turns in the direction of the propeller rotation.

The radial induced velocity data show an increasing trend with radial distance, and a decreasing trend with axial distance, from the rotor plane. Maximum values of approximately 0.5 $\bar{u}_0$ were obtained.

Hot film data for the induced velocities are presented in Figures 45 through 57. Each figure presents the two-channel data for three radial positions. The actual velocities can be obtained by use of the calibration data presented in Figures 27 through 32 and equations in Section III. Average values of the normal induced velocities are indicated in each figure. These average values together with the pressure-derived data are also plotted on Figures 42, 43, and 44. The

double amplitudes of the fluctuations from the average values are approximately 3 ft./sec. No harmonic analyses have been made of the data. Predominant frequencies, however, appear to be at approximately 8 and 21 cycles per second, which correspond to 1 and 3 cycles per rotor revolution.

2. Correlation of Theory With Test Data

Figure 43 presents a comparison of the theory discussed in Section II with the test data. Examining the calculated values for the normal induced velocities, $\bar{u}_N$, it is noted that the triangular blade-loading theory, as expected, gives results which more closely agree with the trend of the experimental data. The constant blade-loading theory results in a constant value of $\bar{u}_N$. The correction for wake contraction is obtained by use of the data of Reference 9. For an axial distance $x/R = 0.26$, the wake radius is given as approximately 85% of the blade radius. Performing the radial correction only, i.e.,

$$\left(\frac{x}{R}, \frac{r}{R}\right)\left(\frac{\bar{u}_N}{\bar{u}_0}\right)_{\text{CORRECTED}} = \left(\frac{\bar{u}_N}{\bar{u}_0}\right)\left(\frac{x}{R}, \frac{r}{R_e}\right)$$

no change in the velocity results, but of course, the constant value goes only up to 0.85 R. The use of the axial as well as the radial correction, i. e.,

$$\frac{u_{N\,\text{CORRECTED}}}{\bar{u}_0}\left(\frac{x}{R}, \frac{r}{R}\right) = \frac{\bar{u}_N}{\bar{u}_0}\left(\frac{x}{R_e}, \frac{r}{R_e}\right)$$

results in a slight increase of the velocity ratio. More significant changes are seen to occur with the use of the triangular blade loading theory. Without correction for wake contraction, the ratio $u_N/\bar{u}_0$ is seen to follow the test data trend of an increase with r/R but with appreciably lower values. Using the radial wake correction only results in substantially better correlation with the test data. The values obtained by using both x/R_e and r/R_e in the calculations provide the best correlation with the average of the

test data. It is of interest to note here that although in accordance with the data of Reference 9 a wake radius of 0.85 has been utilized in the calculations, the present pressure data show that the wake radius for $x/R = 0.26$ is equal to or larger than 0.9 R.

A comparison of the theory with test data shows that the calculations performed with x/R_e and r/R_e result in the lowest values of the tangential velocity ratio $u_a/\bar{u}_0$. The correlation with the limited test data is seen to be fair. It should be noted in this context that the theory does not account for the swirl effects resulting from the profile drag. It is therefore expected that the test data give higher negative values of u_a than those computed.

The variation of the radial induced velocity ratio with r/R for the different analytical approaches is also shown in Figure 44. In comparing the various analytical approaches, in particular for the normal induced velocity ratio, it is concluded that the method using x/R_e and r/R_e wake correction provides the best correlation with the test data for the hovering condition. This method is also used in the comparisons with the test data shown in Figures 42 and 44. It may be seen that, considering the scatter of the experimental data, the calculated values provide a fair to good prediction of the velocities induced in the rotor wake of a helicopter hovering out of ground effect.

Also shown in Figures 42 and 44 are the digital computer-derived results of Reference 1 for $\bar{u}_N/\bar{u}_0$. It may be noted that the results of the much simpler theory presented herein compare well with those of Reference 1.

The blade position indicator used during the testing unfortunately gave erratic readings, and hence it is not possible to compare the calculated and the measured values for the same blade position. The average values and the fluctuation from the average can, however, be used to obtain an indication of the accuracy of the theory.

The calculated instantaneous values for three blade positions corresponding to Flight No. 5 ($x/R = 0.26$, $\psi = 150°$) are presented in Table VI. The corresponding hot film data are shown in Figure 49a. Comparing the calculated values of $u_N/\bar{u}_0$

with the test data, it may be noted that fair to good agreement is obtained for both average values and double amplitude of the velocity fluctuations from the average values.

B. HOVERING IN GROUND EFFECT

1. Experimental Data

The pressure data of the normal induced velocity of the rotor hovering at three altitudes in ground effect are presented in Figure 58. Also presented are the corresponding values obtained for the out-of-ground-effect condition. The data are given for each of the radial and azimuth positions tested. The test data show that, as expected, the normal induced velocity decreases with a decrease of hovering altitude. The variation with radial distance is not as significant in ground effect as it is out of ground effect. Again, changes due to azimuth position are noted. These changes are primarily due to the prevailing surface winds which were on the order of 0 to 12 ft./sec. The radial and tangential velocities in the rotor wake are much more affected by the ambient wind conditions because of their relatively smaller magnitudes. The inaccuracies experienced in the measurement of these velocity components therefore did not warrant the presentation of these data.

Hot film data of the induced velocities in ground effect are presented in Figures 59 to 61. Again, the velocity fluctuations are seen to be relatively small.

2. Correlation of Theory With Test Data

In Reference 10, an empirical relationship of the ratio between the average normal induced velocities at the rotor plane in ground effect and out of ground effect was presented. This relationship, which was based on the data of References 7 and 8, was represented by a factor $kg = 1-0.09e^{-2(H/R)}$. A plot of kg is shown in Figure 62. Also shown in this figure are values of kg obtained from the pressure data of the present program.

It may be noted that good agreement is obtained for the data closest to the rotor plane, $x/R = 0.22$. For a given hovering height, H/R, the normal induced velocity is seen to decrease with axial distance behind the rotor. This is consistent

with the fact that the actual wake expands as the flow approaches the ground. For the same mass flow, this expansion, of course, results in a reduced velocity.

C. FORWARD FLIGHT

1. Experimental Data

The time-averaged values of normal $\bar{u}_N$, longitudinal $\bar{u}_L$, and lateral $\bar{u}_y$ velocities obtained from the flight test are presented in Figures 63 through 68. The data are presented for forward flight speeds of 20 m.p.h. and 46 m.p.h. The velocities are nondimensionalized by $\bar{u}_0$, as obtained from equation (79), and are presented versus radial position measured from the hub centerline.

These data were obtained with the pressure probes aligned with the flight direction for all azimuth positions. Hence, the velocity components measured are parallel to the rotor shaft, $\bar{u}_N$, and in the longitudinal and lateral directions, $\bar{u}_L$ and $\bar{u}_y$, respectively. These velocity measurements are for the total velocity components and hence include the induced velocities as well as the components of the forward flight speed. The helicopter flight and control parameters associated with these data are presented in Table VII. The data of the velocity component normal to the fuselage, $\bar{u}_N$, for $\psi = 30°$ and $x/R = 0.22$, show maximum values of $2.5\ \bar{u}_0$ and $4.0\ \bar{u}_0$ for forward speeds of 20 and 46 m.p.h., respectively. The corresponding velocities at the other azimuth positions are substantially lower. The fuselage attitude during these tests was on the order of one degree, and hence the forward speed contribution to these measurements is relatively small. At larger distances below the rotor, i.e., for increasing values of x/R, the variation of $\bar{u}_N/\bar{u}_0$ with azimuth is seen to decrease. The longitudinal velocity measurements are generally seen to be on the order of the forward speed, V. Some reductions from the value of V are noted. These are believed to be primarily due to the effect of flow retardation caused by the rotor drag.

The lateral velocities, $\bar{u}_y$, include only a minor component of the forward speed. In fact, if it is assumed that rotor lateral flapping can be neglected, $\bar{u}_y = \sqrt{\bar{u}_r^2 + \bar{u}_a^2} \approx \bar{u}_r$.

The measured value of the ratio $\bar{u}_y / \bar{u}_0$ is on the order of 0.4, which is similar to that measured for the hovering conditions.

Hot film data for the two forward speeds are presented in Figures 63 through 68. The average values of these data are generally in agreement with the pressure data. The fluctuations from the average values are seen to be smaller than those measured for the hovering flight conditions.

2. Correlation of Theory With Test Data

Some theoretical values of $\bar{u}_N / \bar{u}_0$ were computed, and the results are shown in Figure 63 for ψ = 30 and 270°. As expected, this theory, which does not account for azimuthal variation of vortex strength, fails to predict the rather large variation of induced velocities as measured. The calculated values are lower for ψ = 30° and higher than the test data for ψ = 270°, and appear to give an average of the measured values. As the axial distance from the rotor increases, the applicability of the theory may be expected to increase. This is also borne out by the previously mentioned decrease of the azimuthal variations for increasing x/R.

Some computed instantaneous values for the normal induced velocities are presented in Table VIII. It may be noted that the fluctuations from the average values are smaller than those computed for the hovering conditions. This seems to be confirmed also by the test data of Figures 69 through 71.

u_N AXIAL VELOCITY COMPONENT

u_α TANGENTIAL VELOCITY COMPONENT

u_r RADIAL VELOCITY COMPONENT

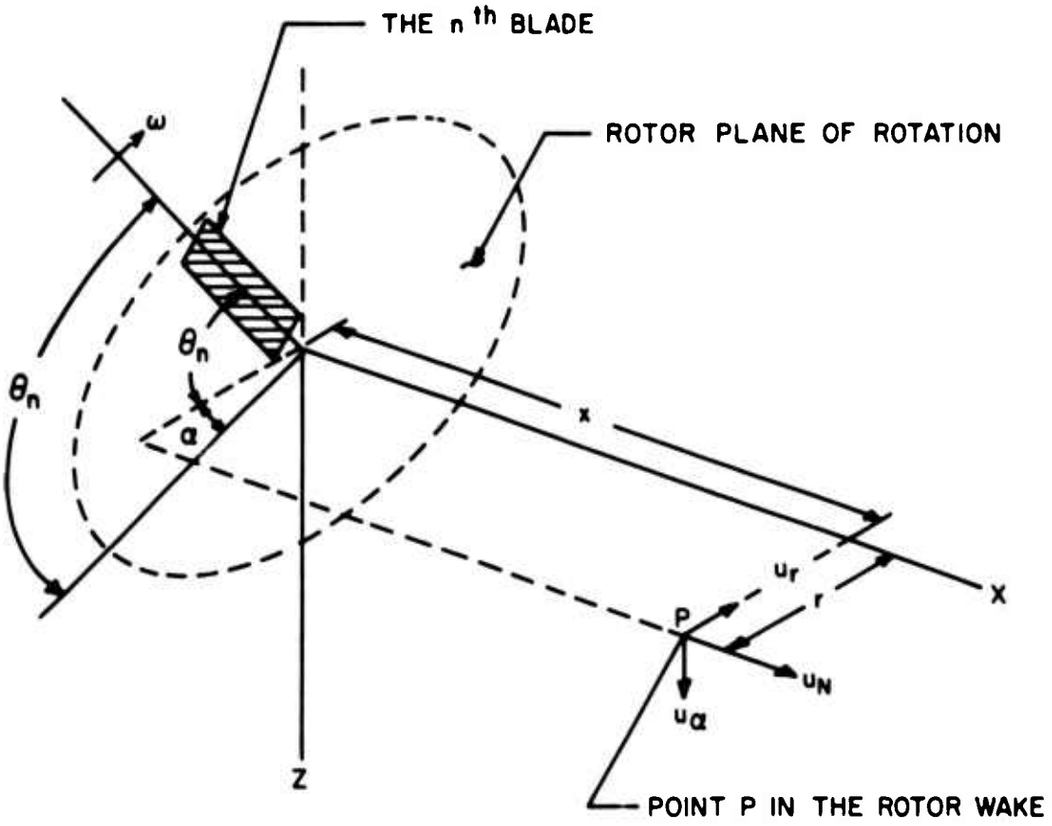

Figure 1. Definitions of Velocity Components and Coordinates of Point P in the Rotor Wake for Axial Flow Conditions.

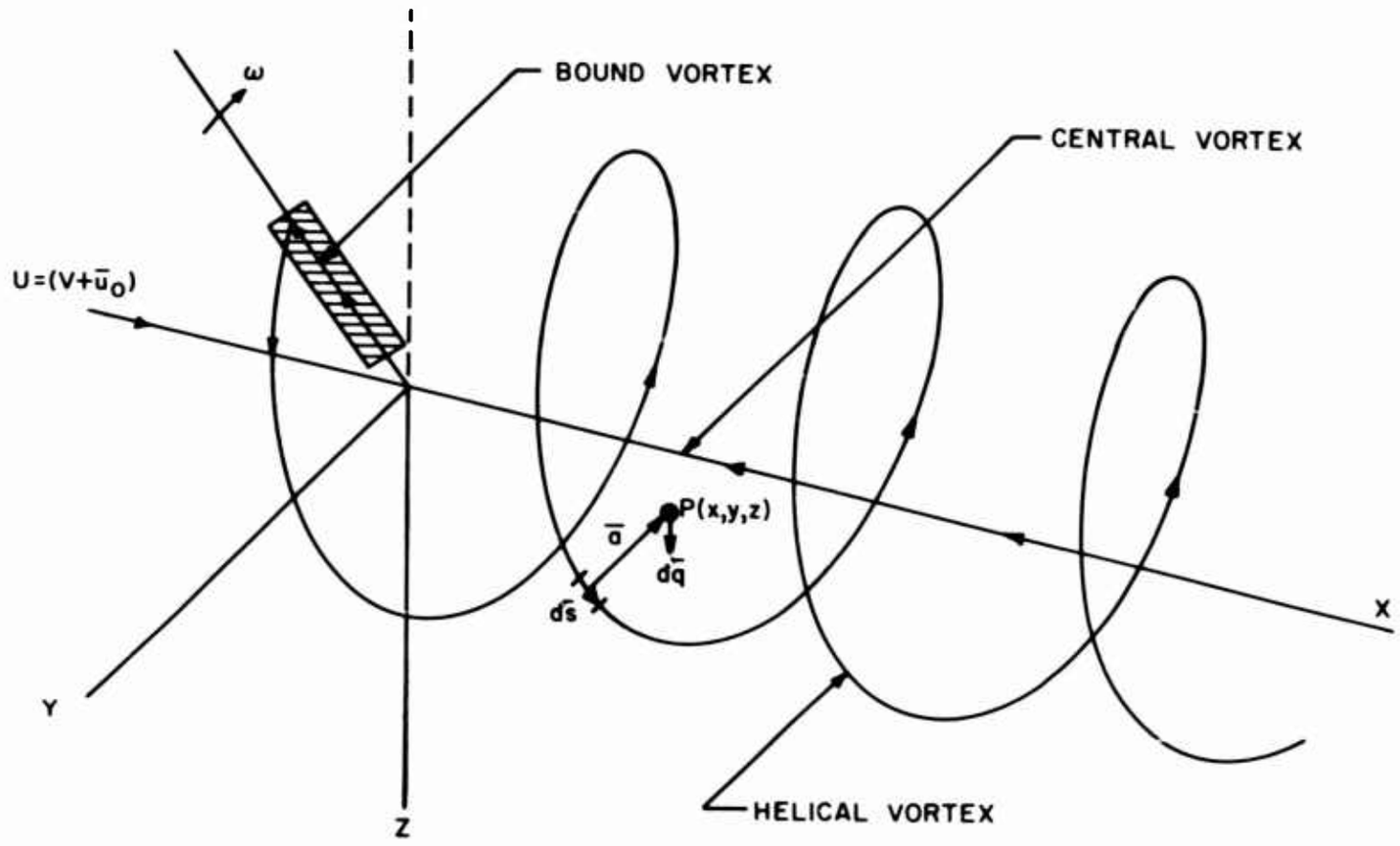

Figure 2. Representation of the Flow Field of a Rotor Blade by a Vortex System - Axial Flow.

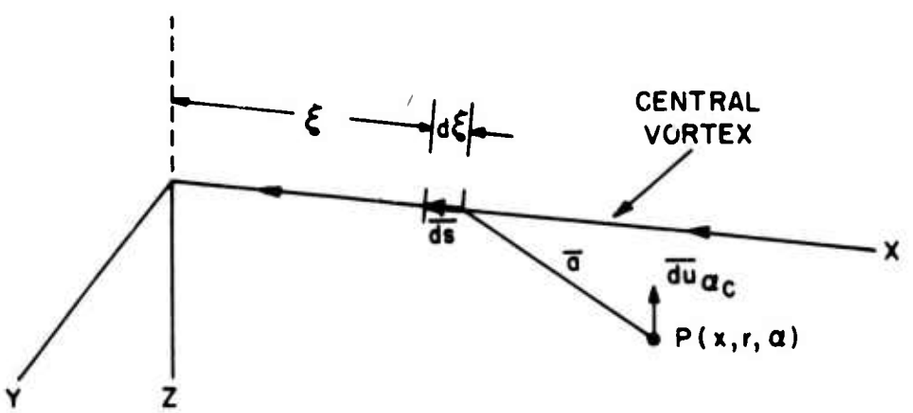

Figure 3. Velocity Induced by the Central Vortex at Point P.

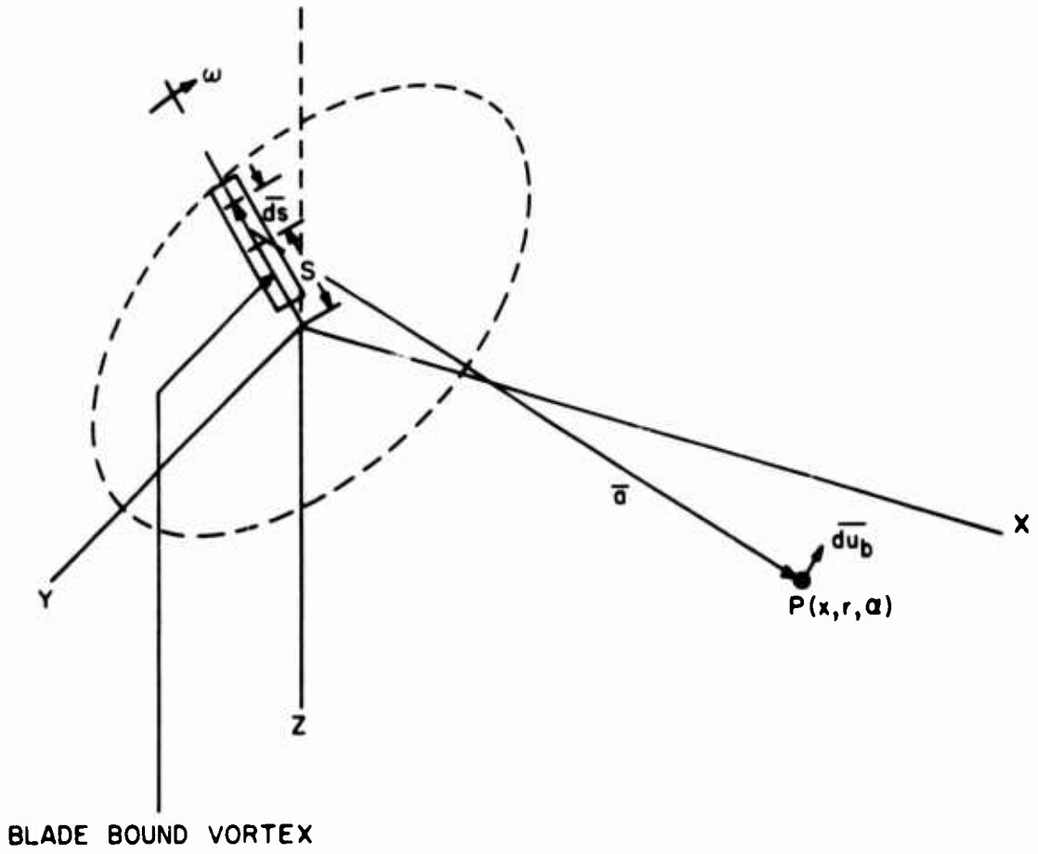

Figure 4. Velocity Induced by the Blade Bound Vortex at Point P.

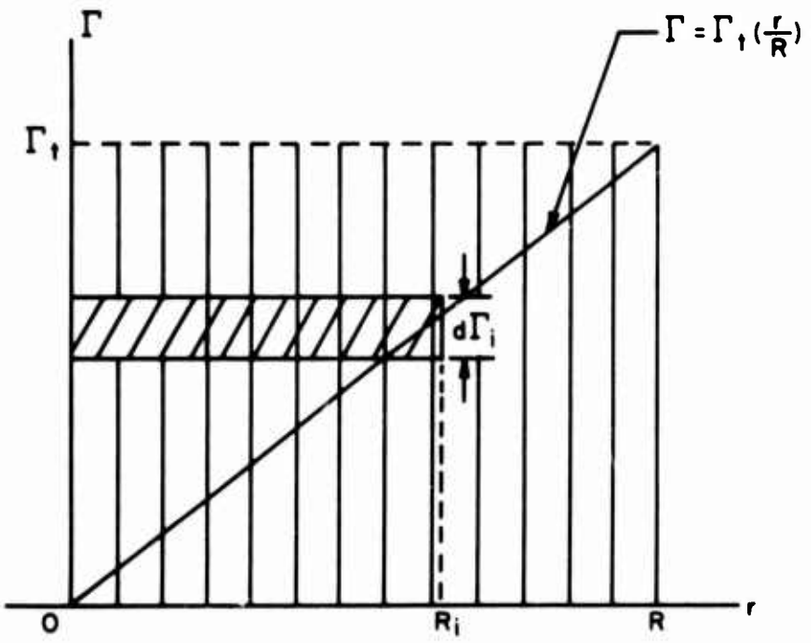

Figure 5. Graphical Representation of a Triangularly Loaded Blade.

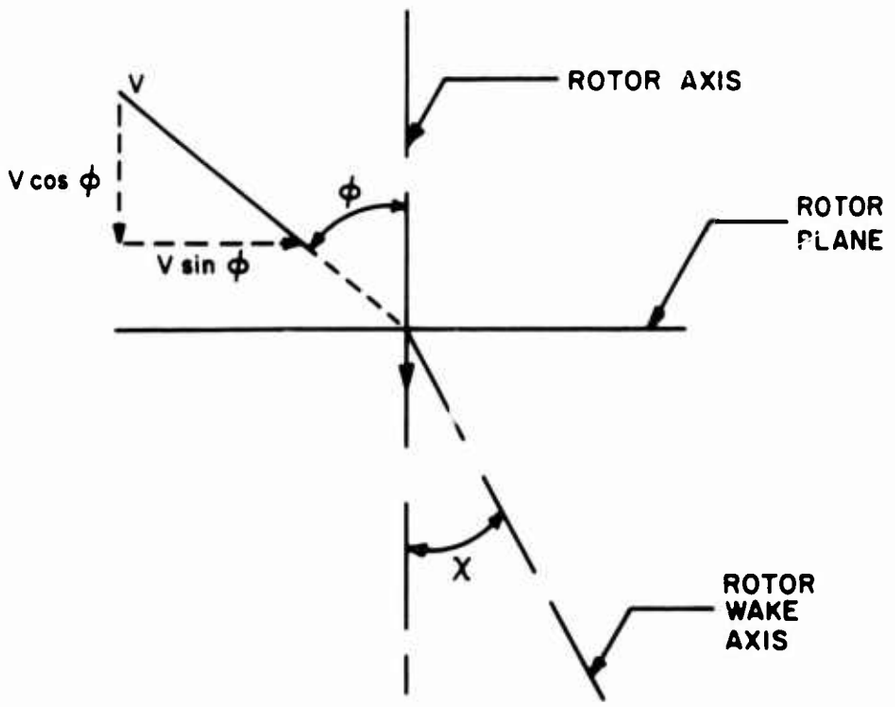

Figure 6. Rotor in Yawed Flow.

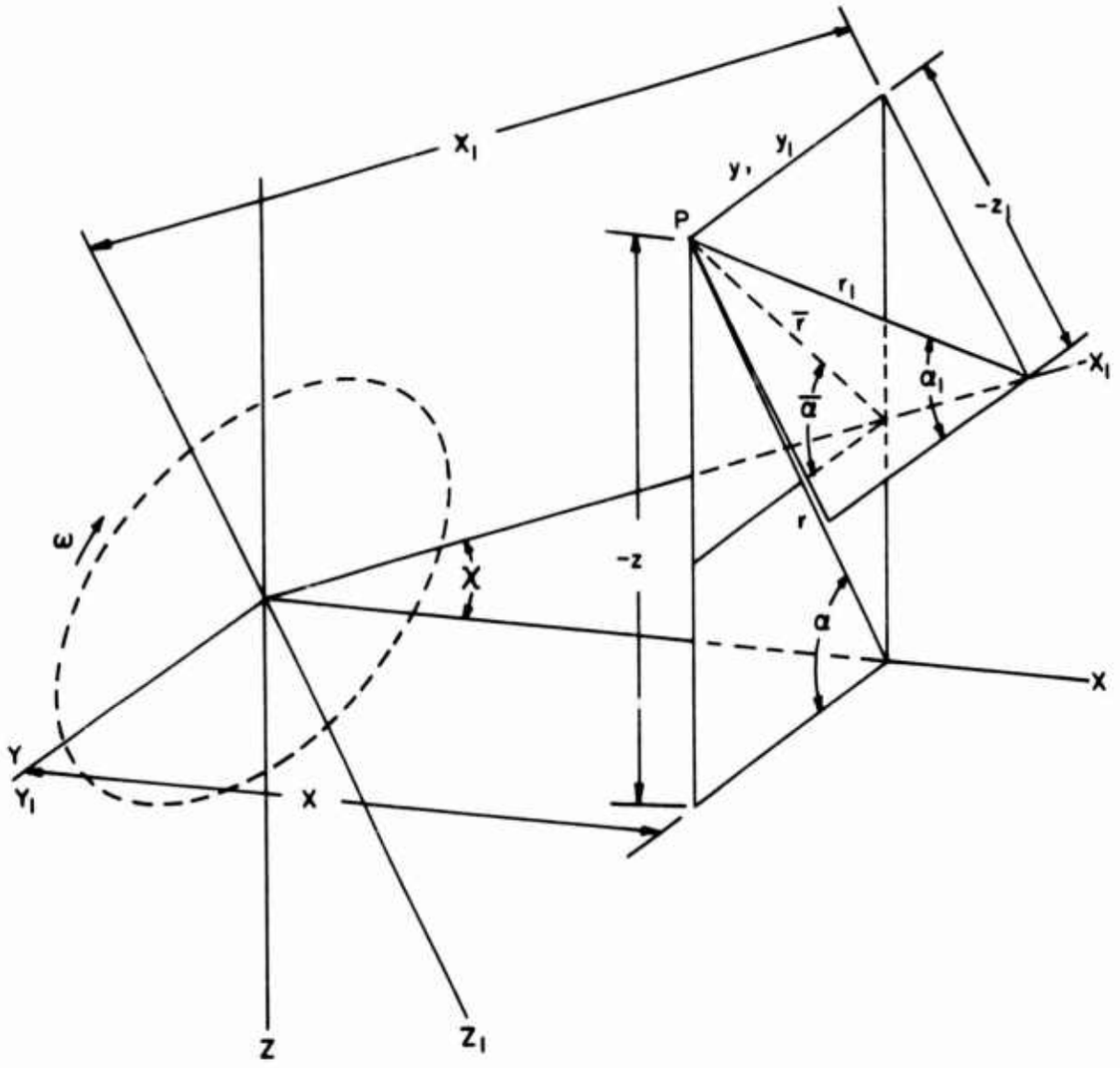

Figure 7. Definitions of Velocity Components and Coordinates of Point P in the Rotor Wake for the Yawed Flow Condition.

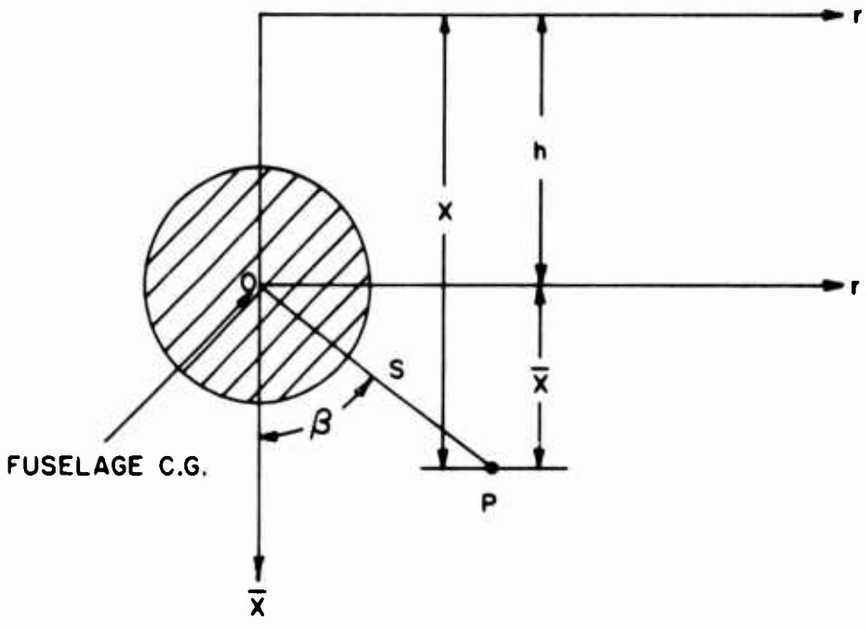

Figure 8. Coordinate System Fixed to the Fuselage Center of Gravity.

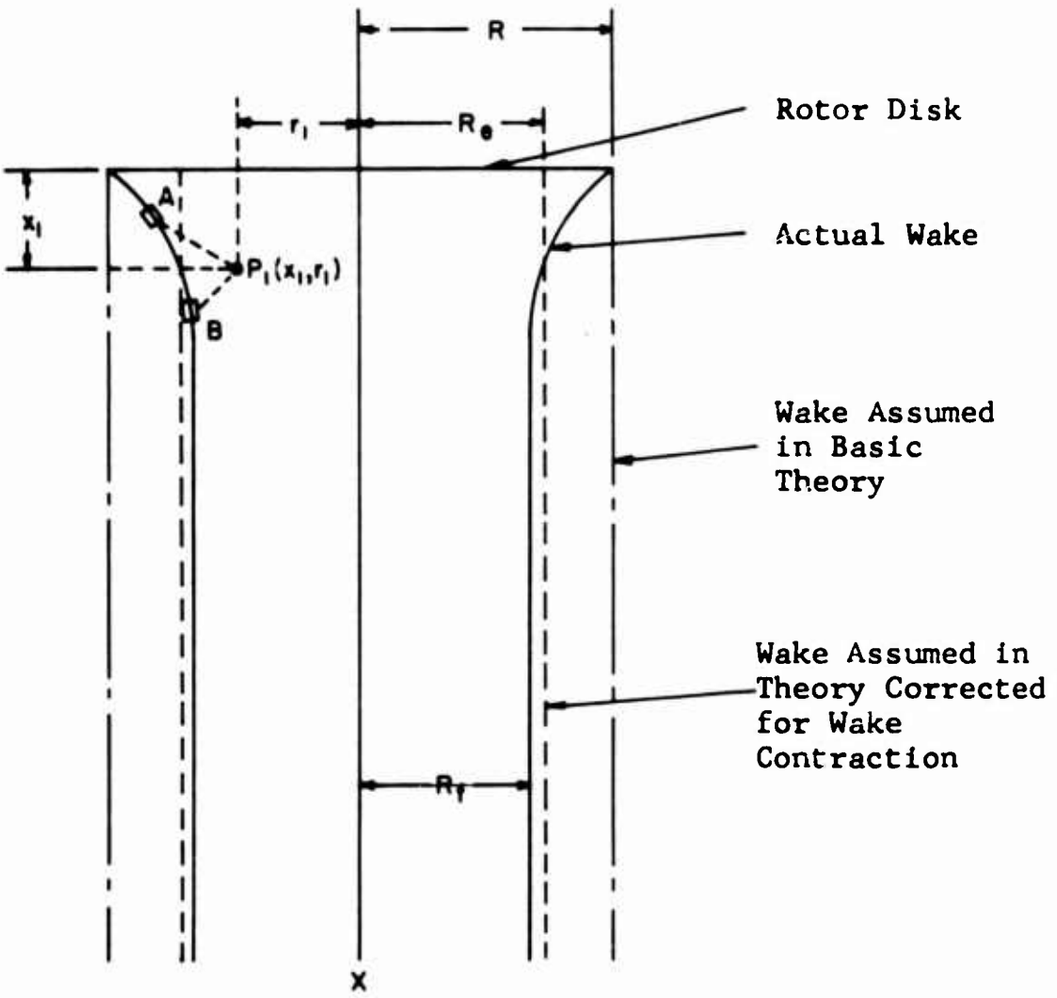

Figure 9. Graphical Representation of Wake Contraction.

Figure 10. Installation of Test Booms and Support Structure on Test Helicopter, Side View.

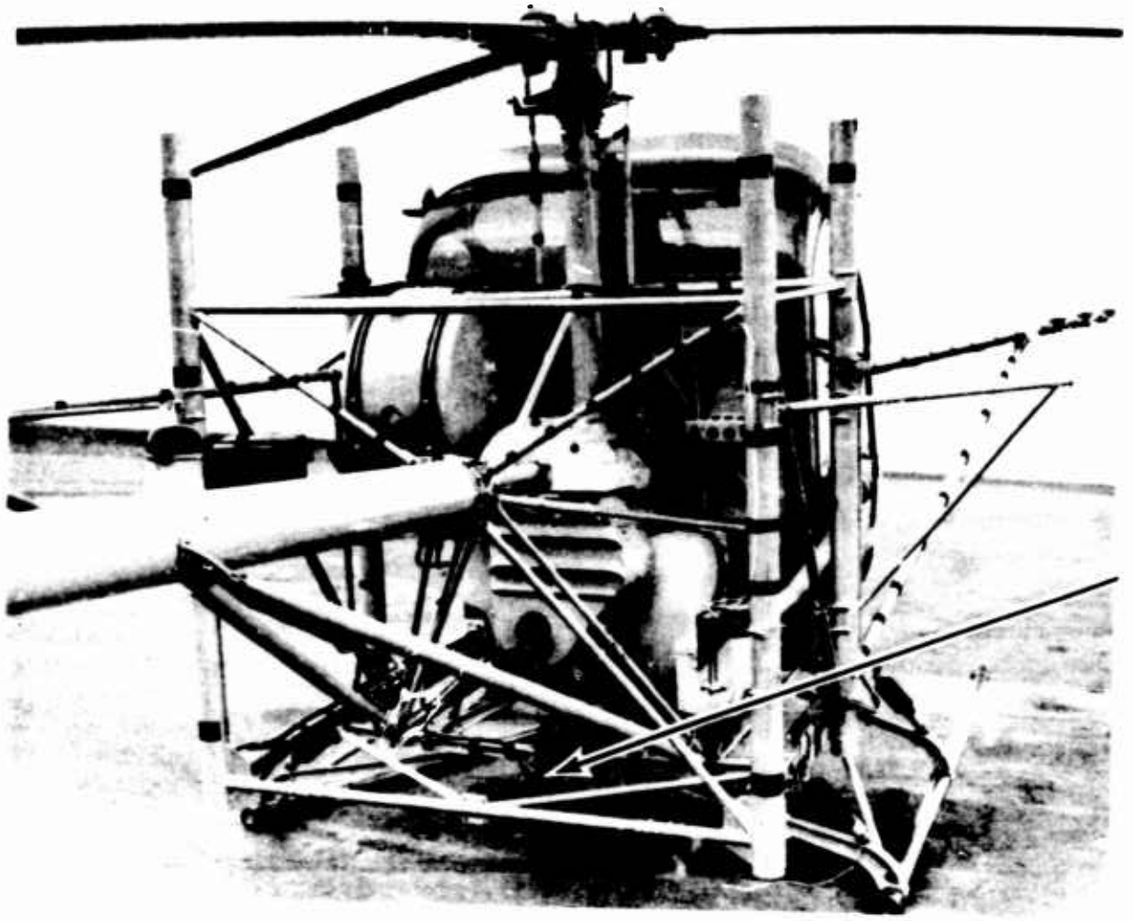

Accelerometer

Figure 11. Installation of Test Booms and Support Structure on Test Helicopter, 3/4 Rear View.

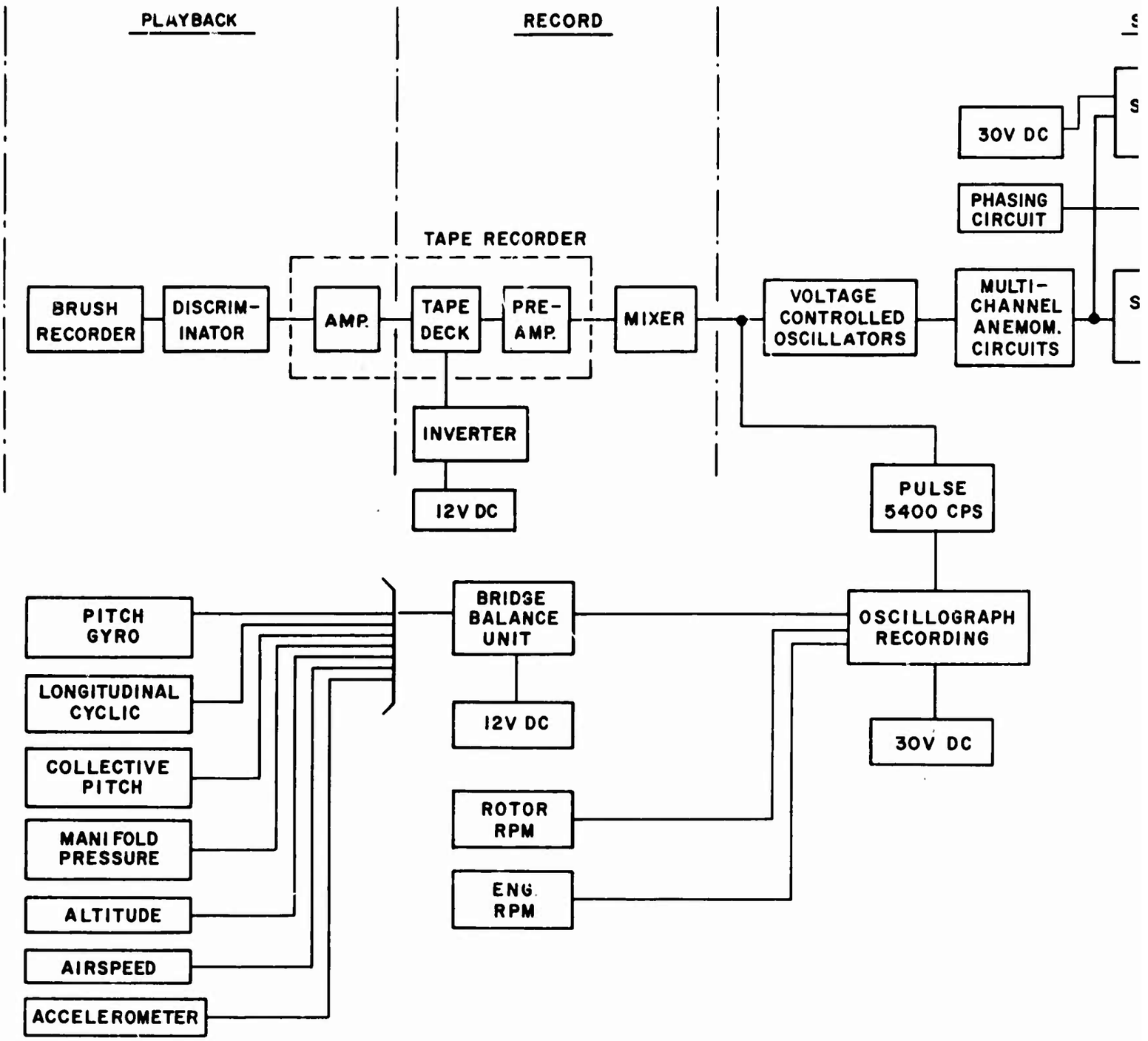

Figure 12. Data Sensing and Acquisition System.

A

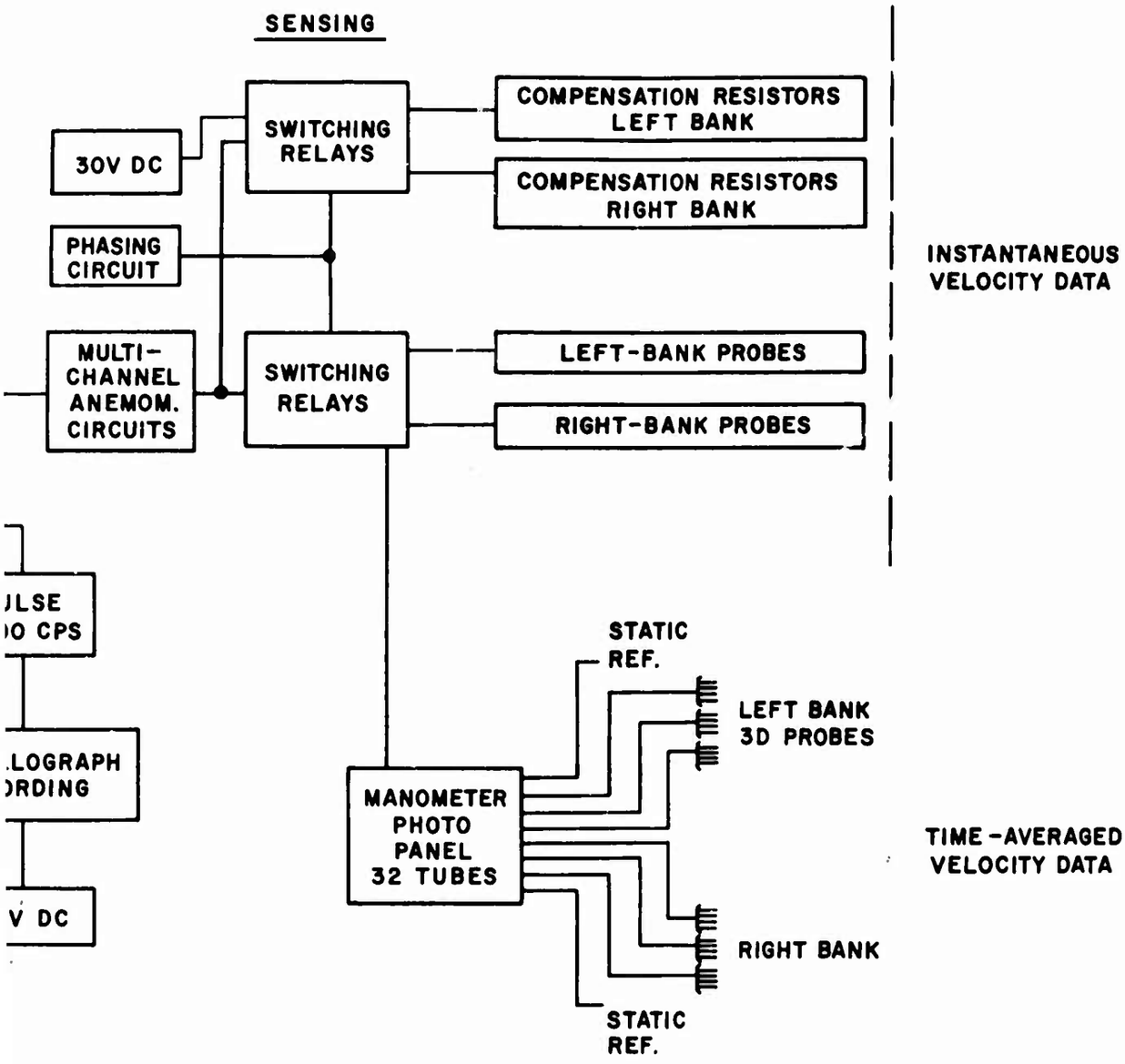
SENSING
30V DC
SWITCHING RELAYS
COMPENSATION RESISTORS LEFT BANK
COMPENSATION RESISTORS RIGHT BANK
PHASING CIRCUIT
INSTANTANEOUS VELOCITY DATA
MULTI-CHANNEL ANEMOM. CIRCUITS
SWITCHING RELAYS
LEFT-BANK PROBES
RIGHT-BANK PROBES
ULSE
)0 CPS
.LOGRAPH
)RDING
V DC
STATIC REF.
LEFT BANK 3D PROBES
MANOMETER PHOTO PANEL 32 TUBES
TIME-AVERAGED VELOCITY DATA
RIGHT BANK
STATIC REF.

B

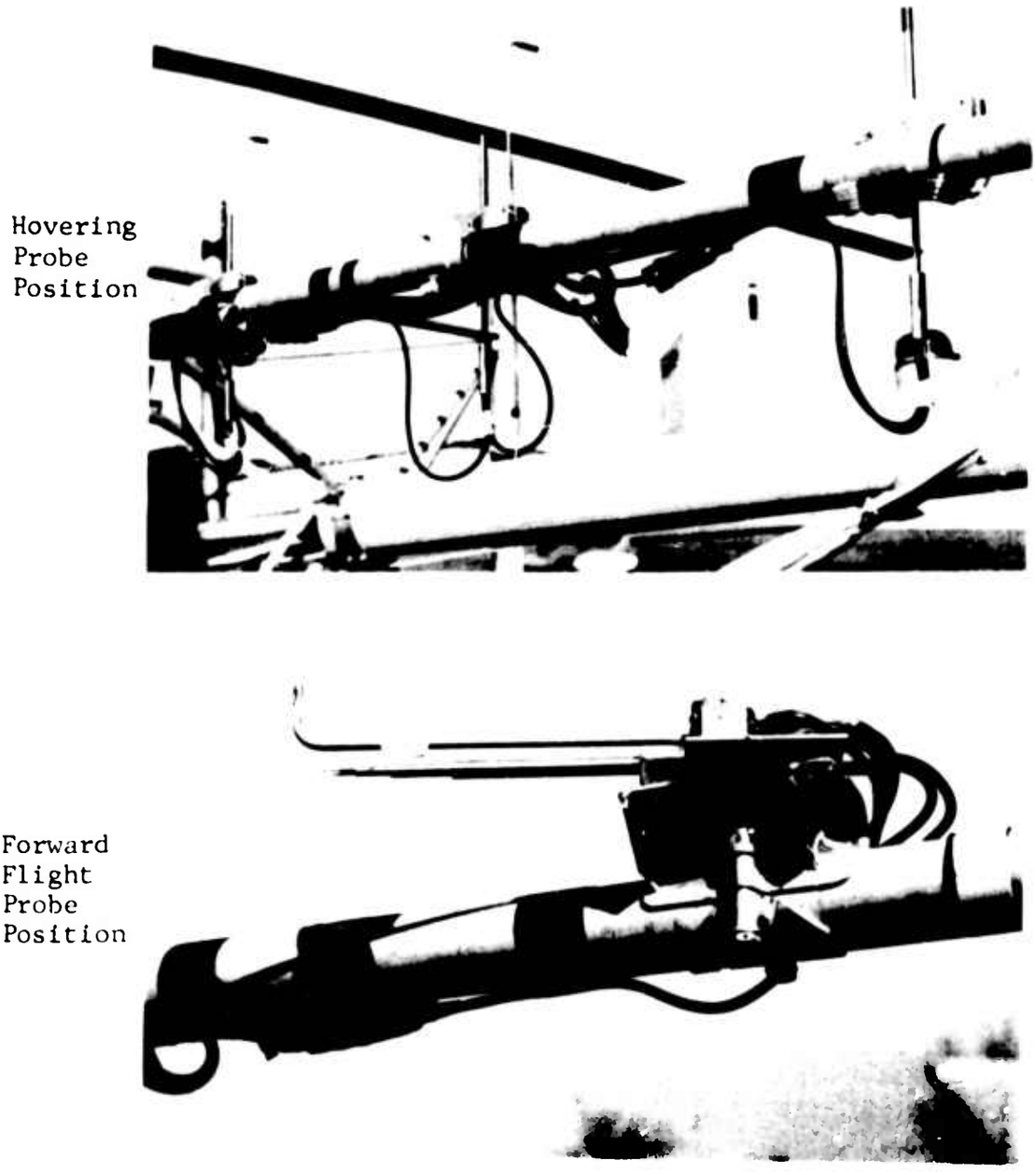

Figure 13. Velocity-Sensing Probes Mounted on Horizontal Boom.

Figure 14. Recording Instrumentation Mounted in Cabin of Hughes-269 Helicopter.

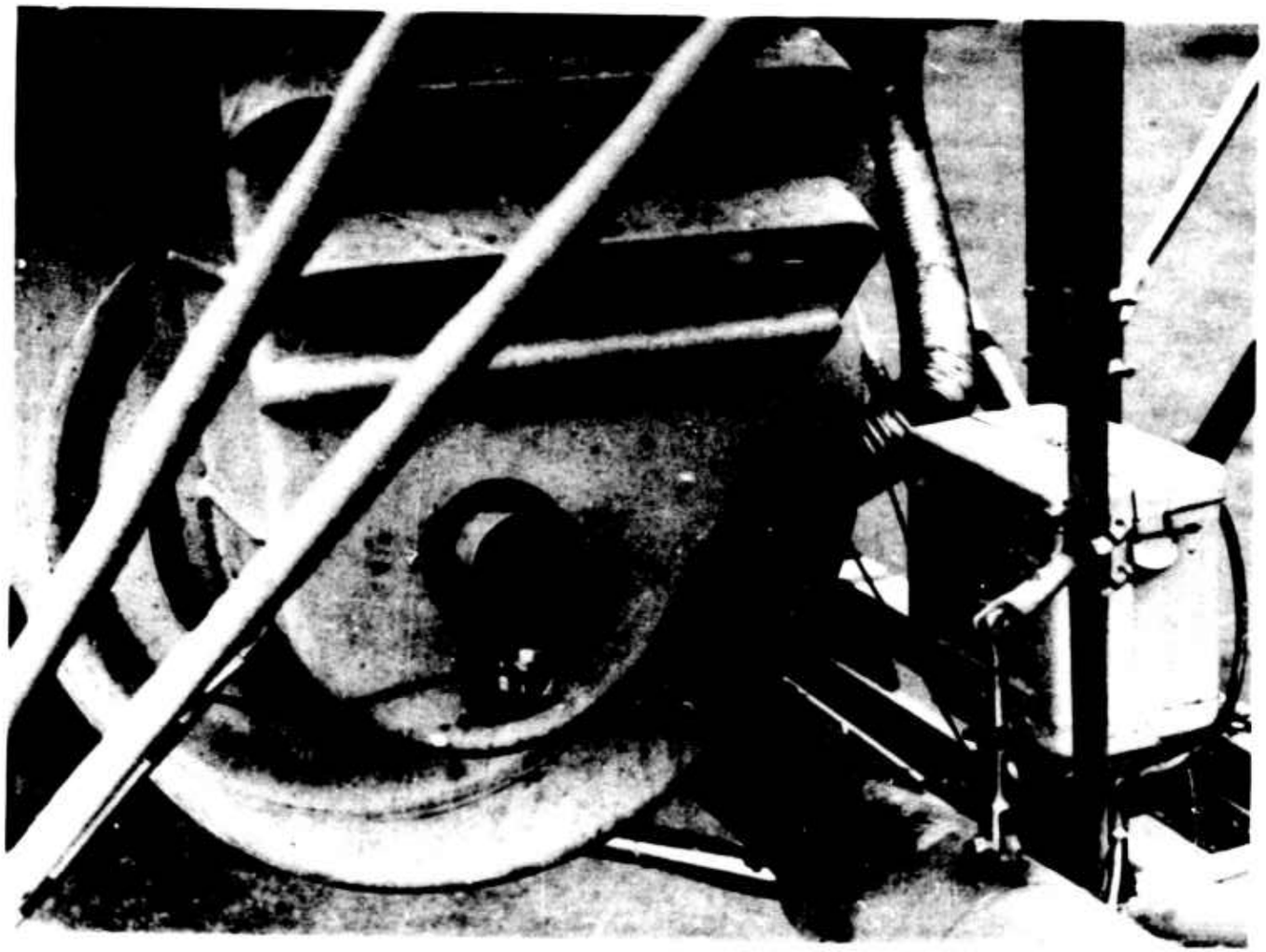

Figure 15. Engine R.P.M. Magnetic Pickup Instrument on Output Shaft.

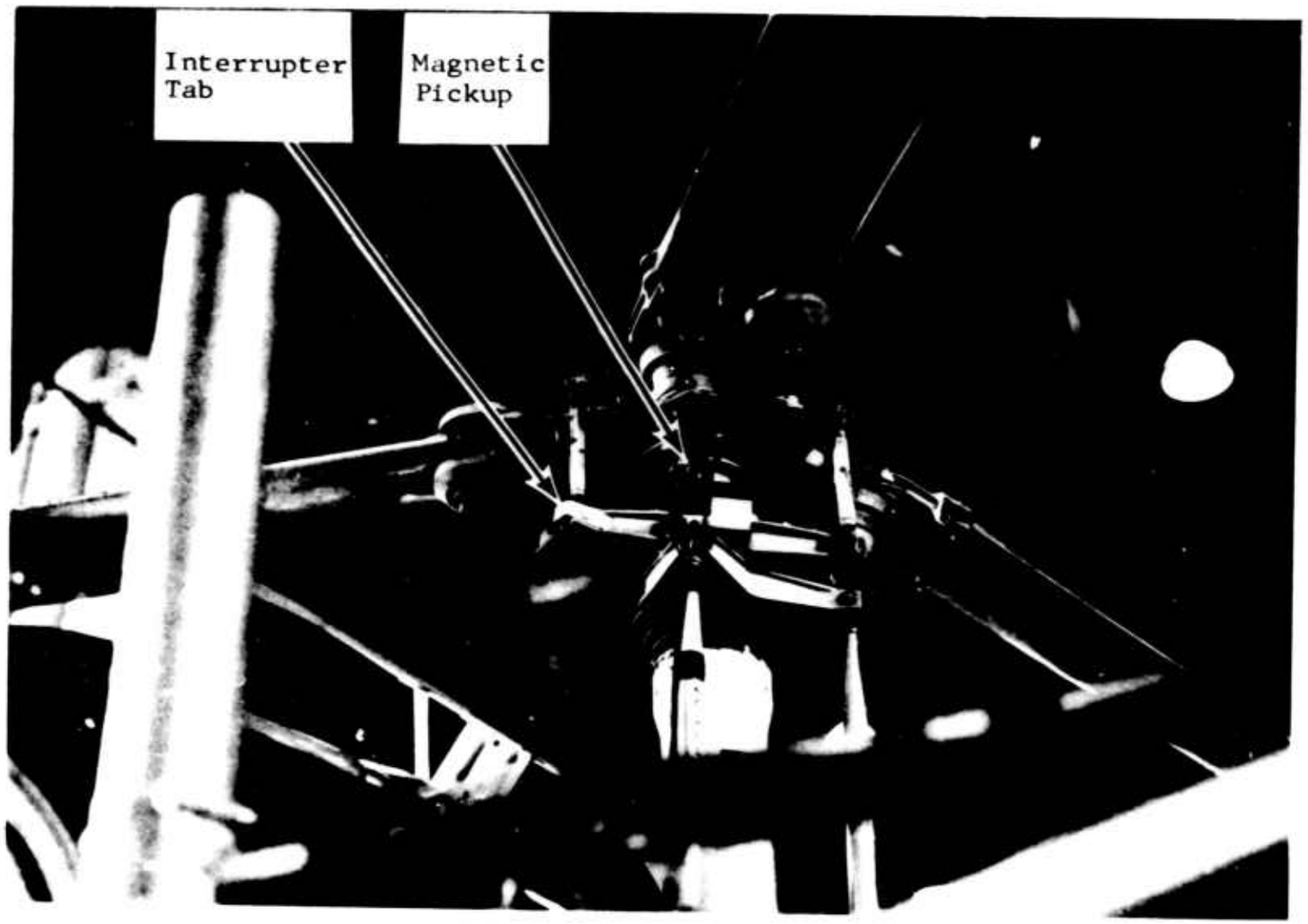

Figure 16. Rotor R.P.M. Magnetic Pickup Instrument on Swash Plate.

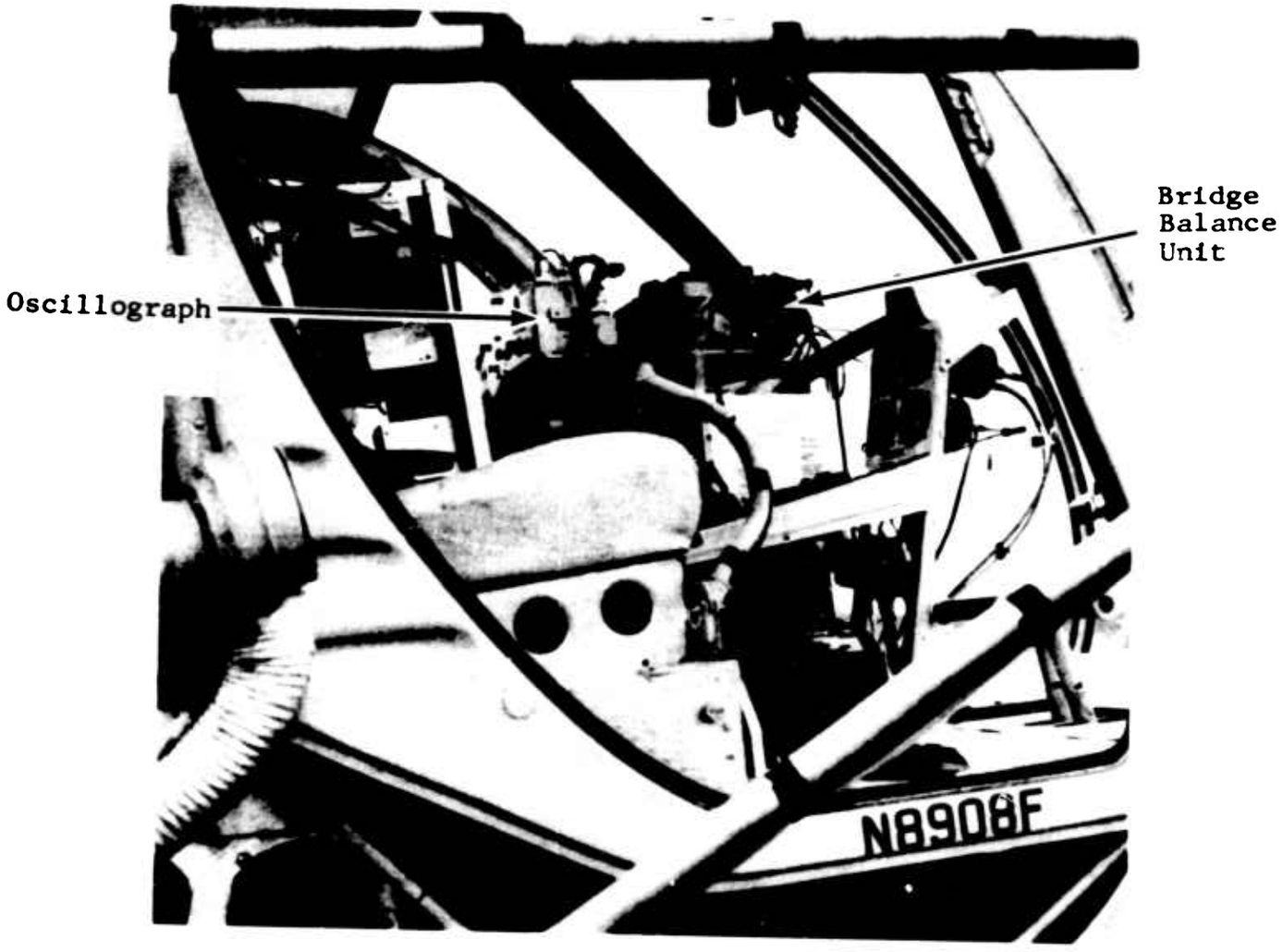

Figure 17. Fuselage Pitch Gyro Mounted on Cabin Floor.

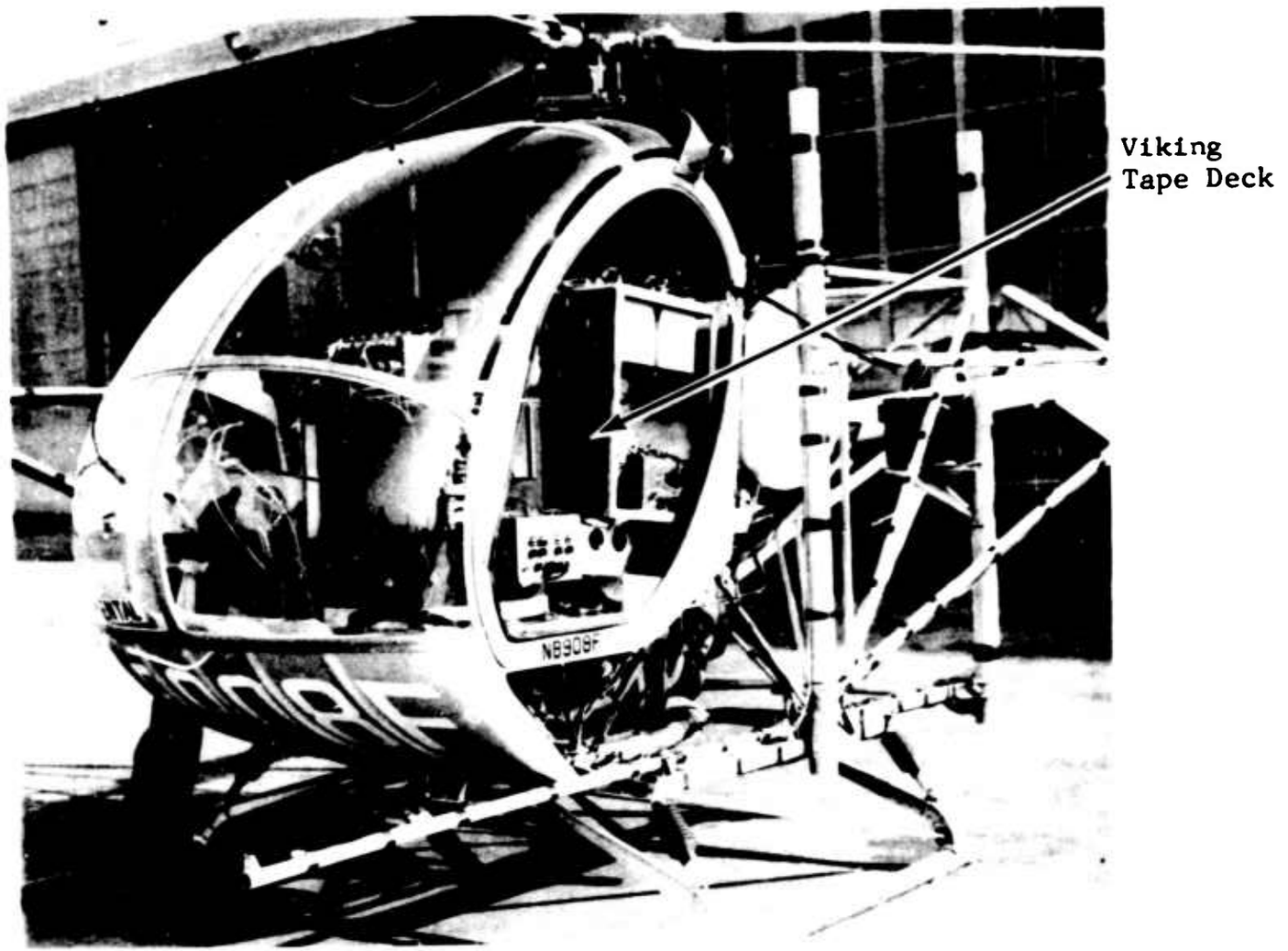

Figure 18. Installation of Recording Equipment in Cabin.

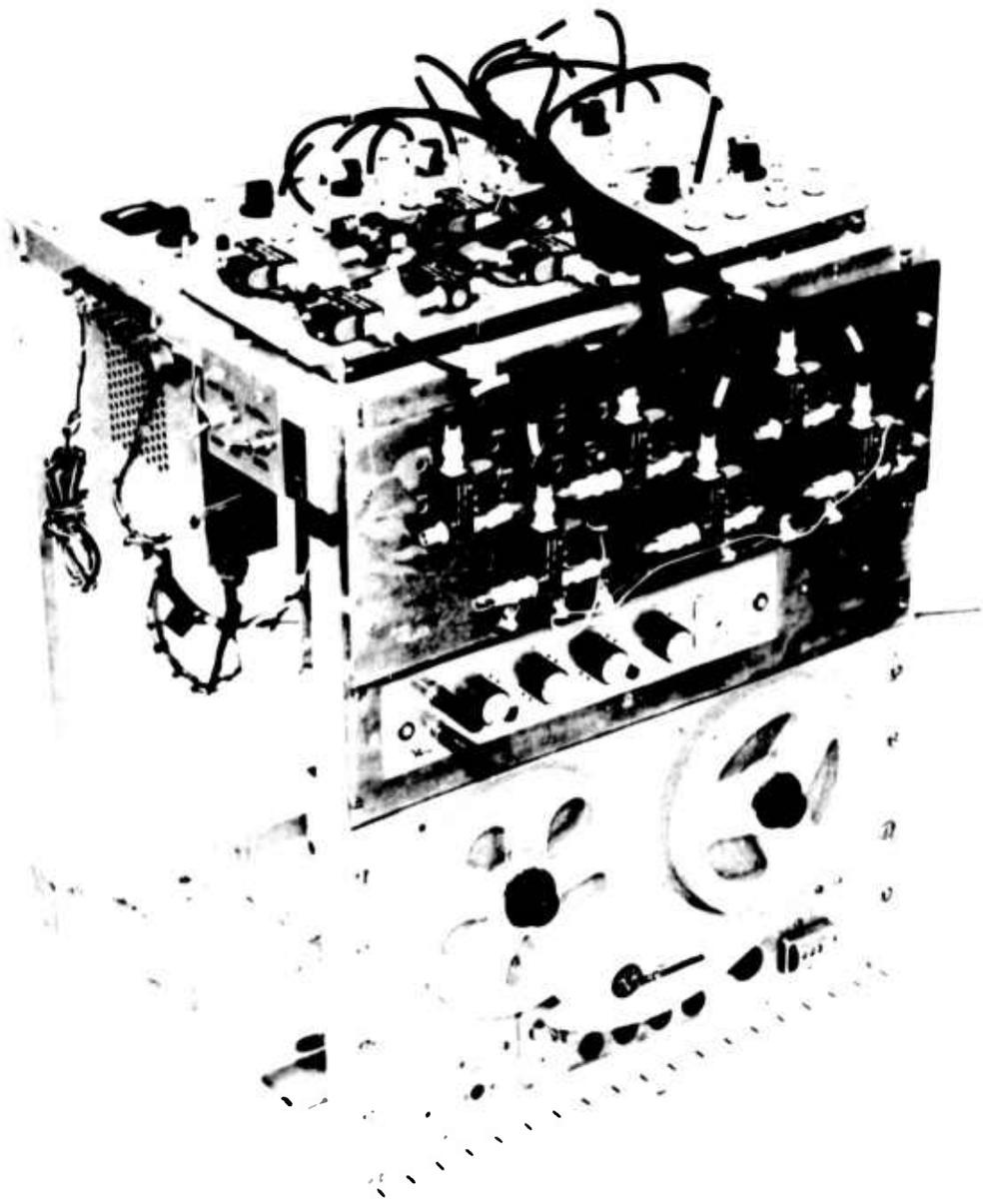

Figure 19. Recorder and Anemometer Module Package.

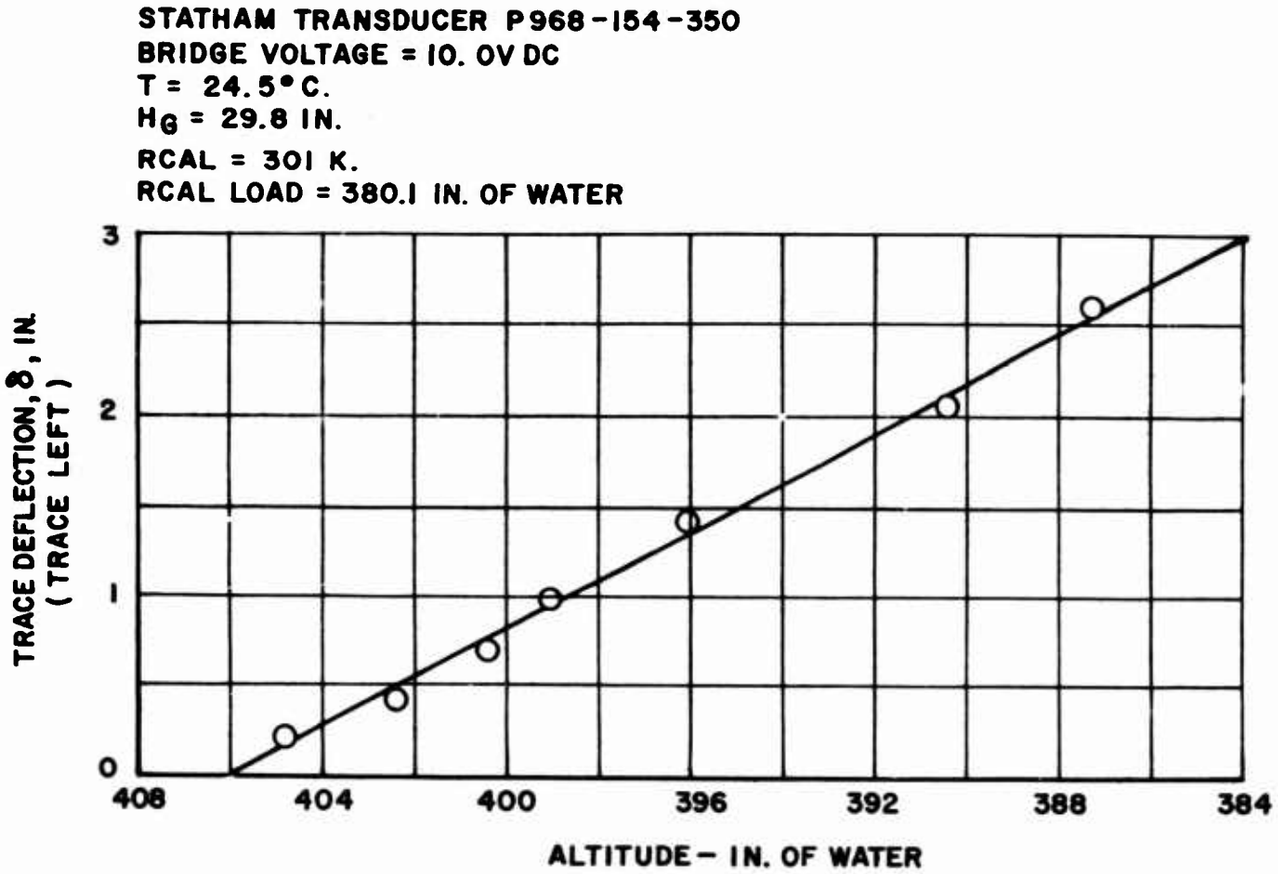

Figure 20. Altitude Calibration.

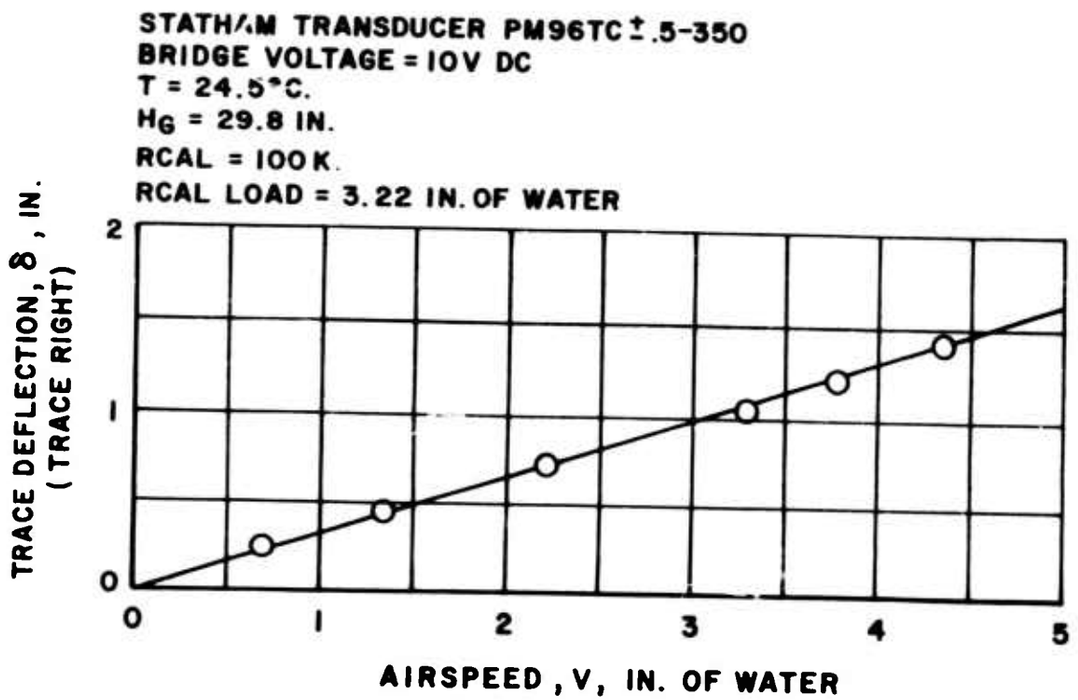

Figure 21. Airspeed Calibration.

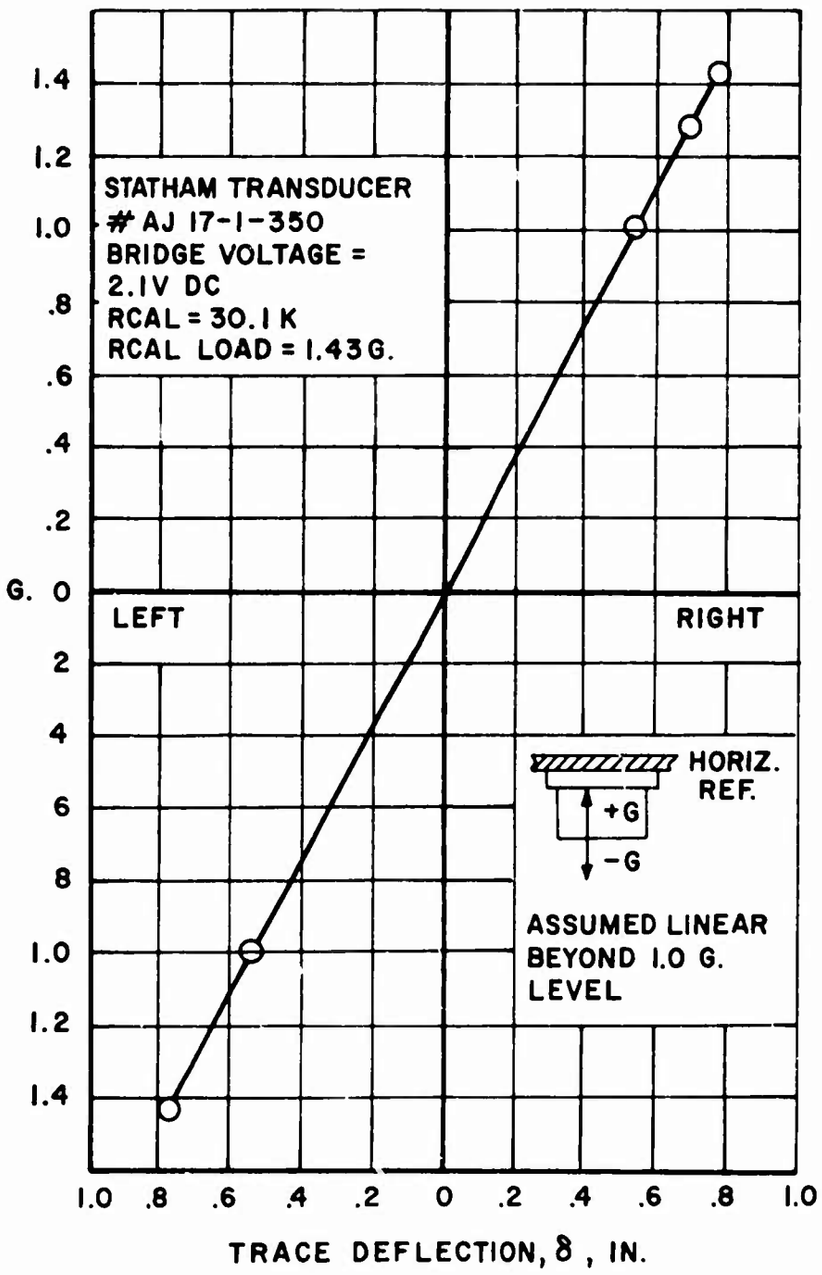

Figure 22. Accelerometer Calibration.

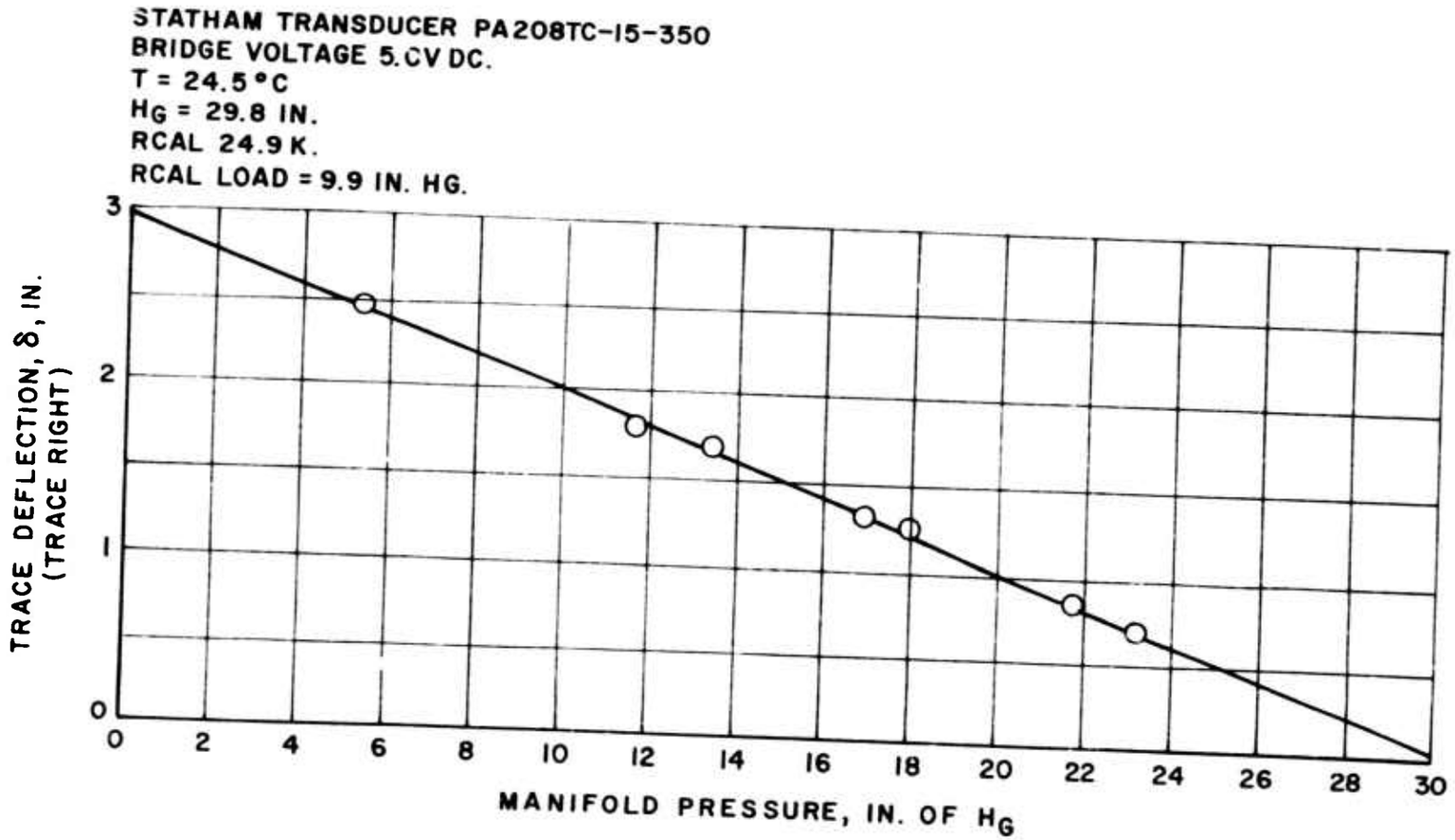

Figure 23. Manifold Pressure Calibration.

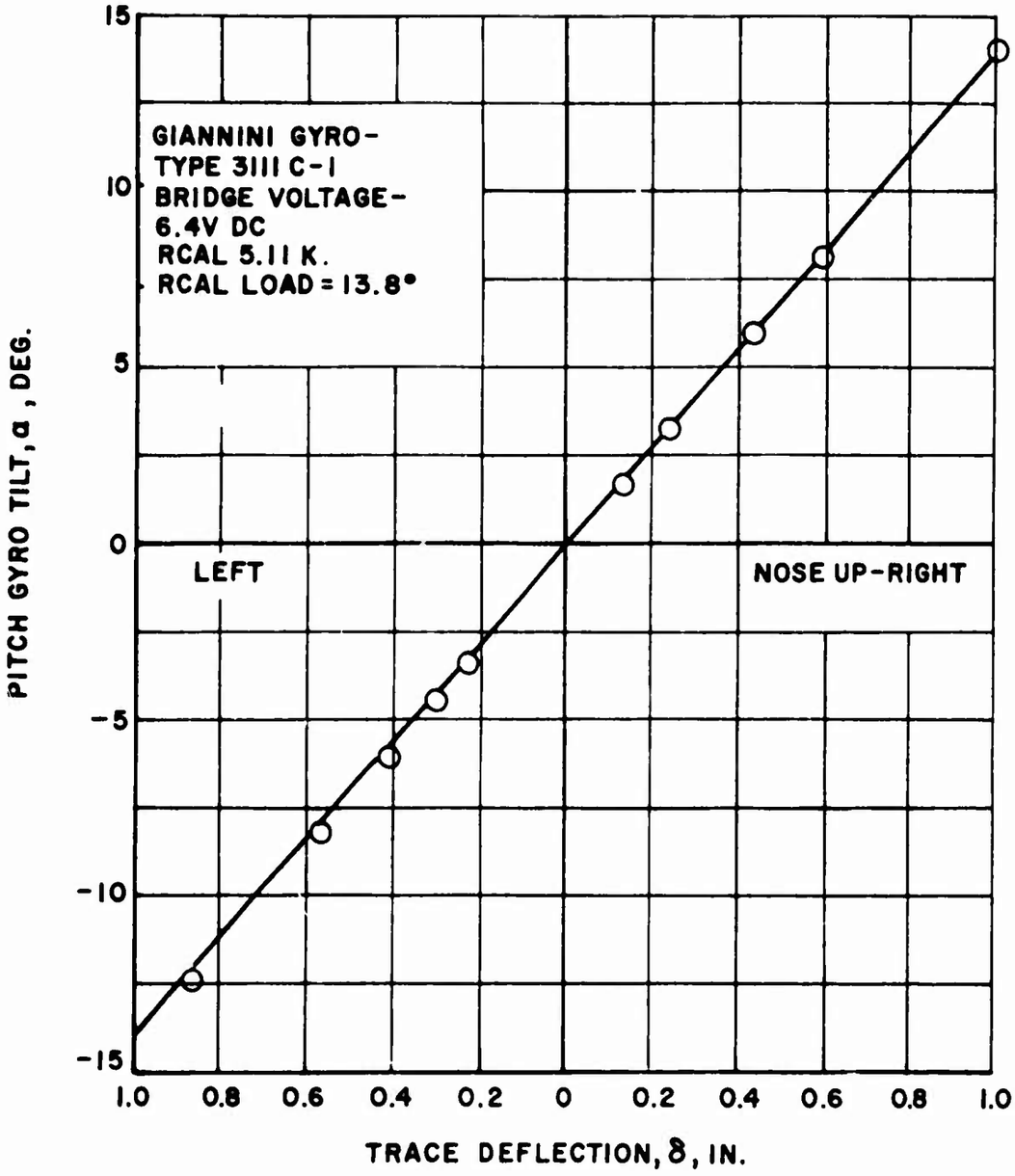

Figure 24. Helicopter Fuselage Pitch Calibration.

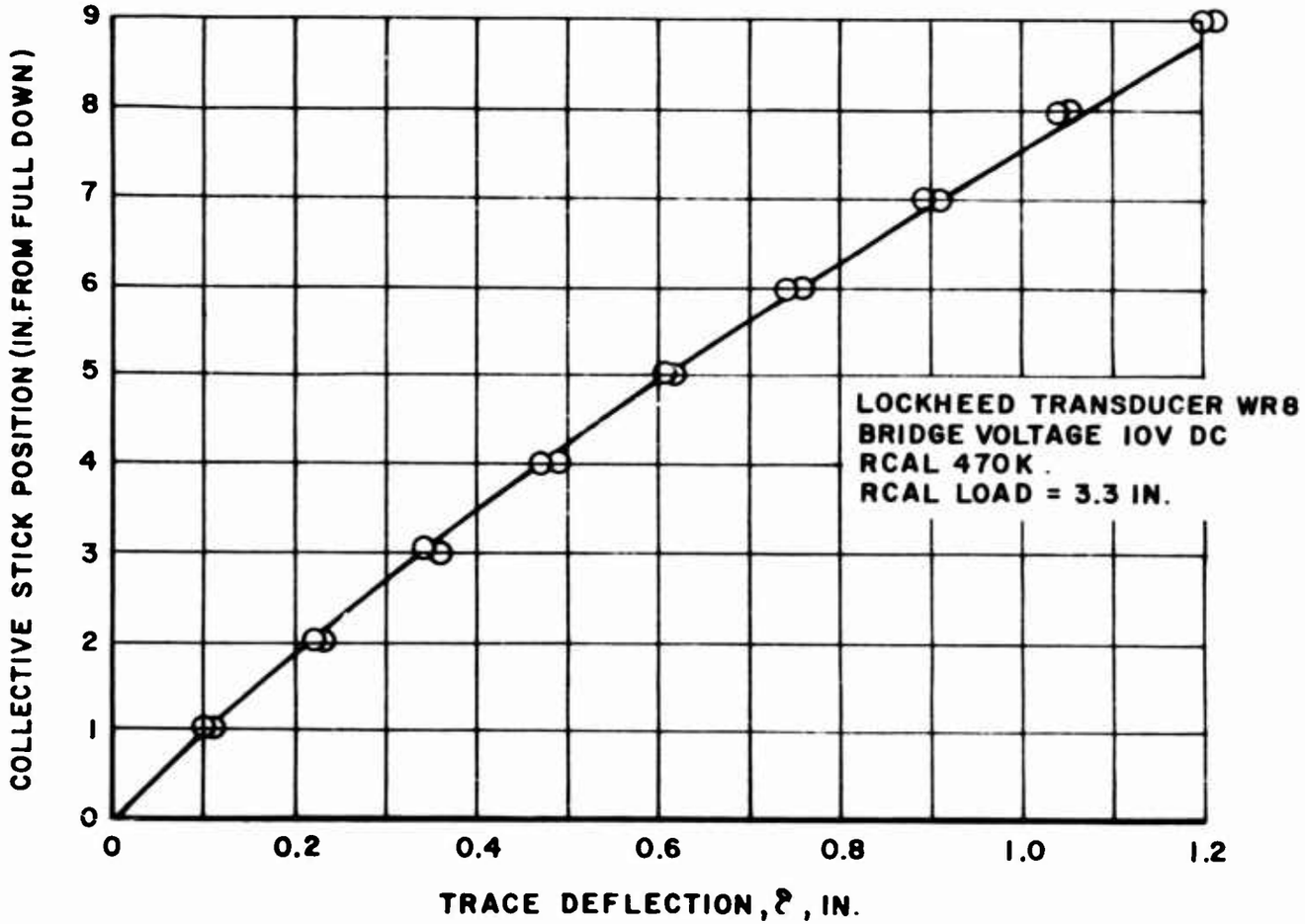

Figure 25. Collective Stick Calibration.

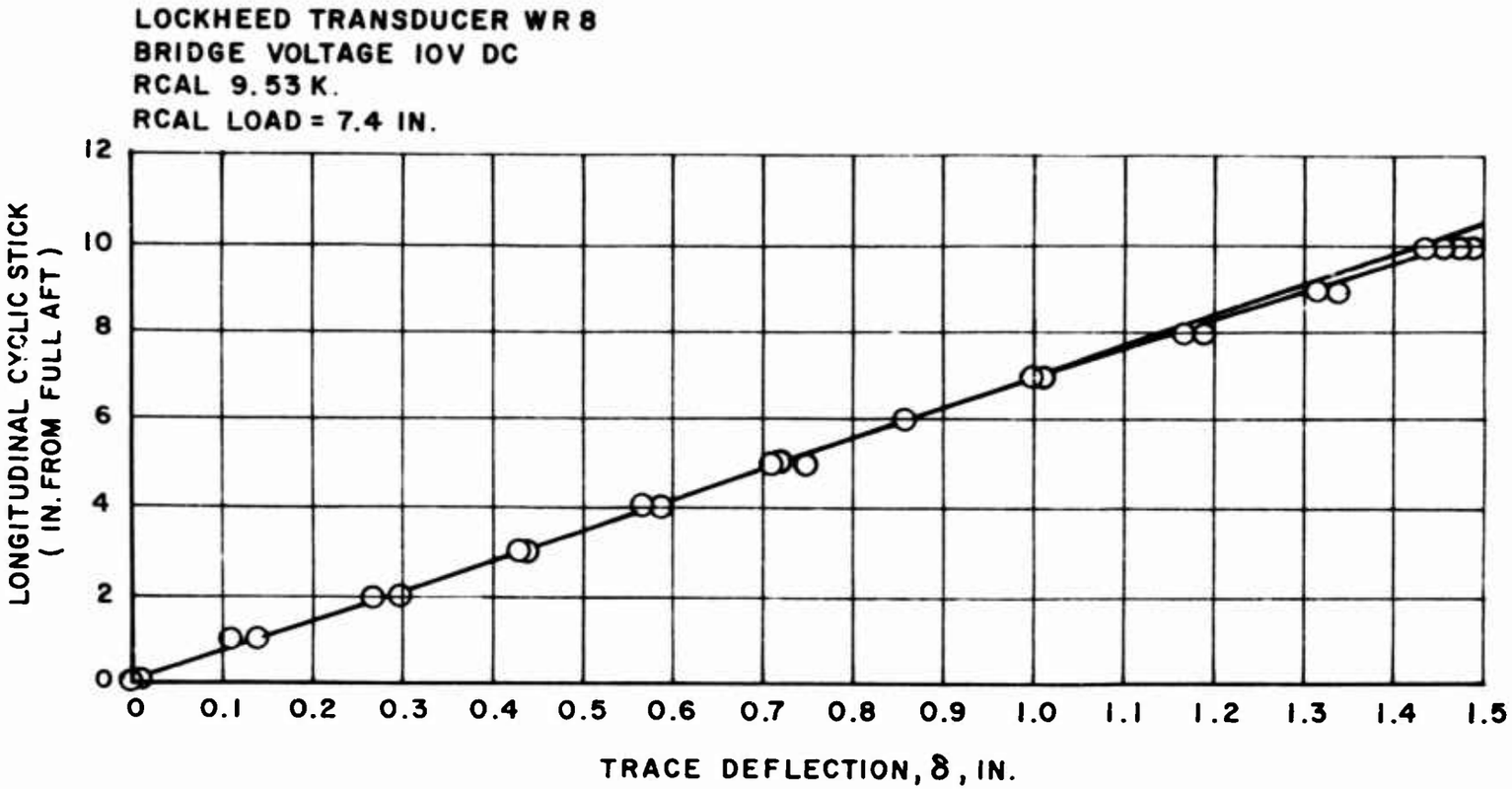

Figure 26. Longitudinal Cyclic Stick Calibration.

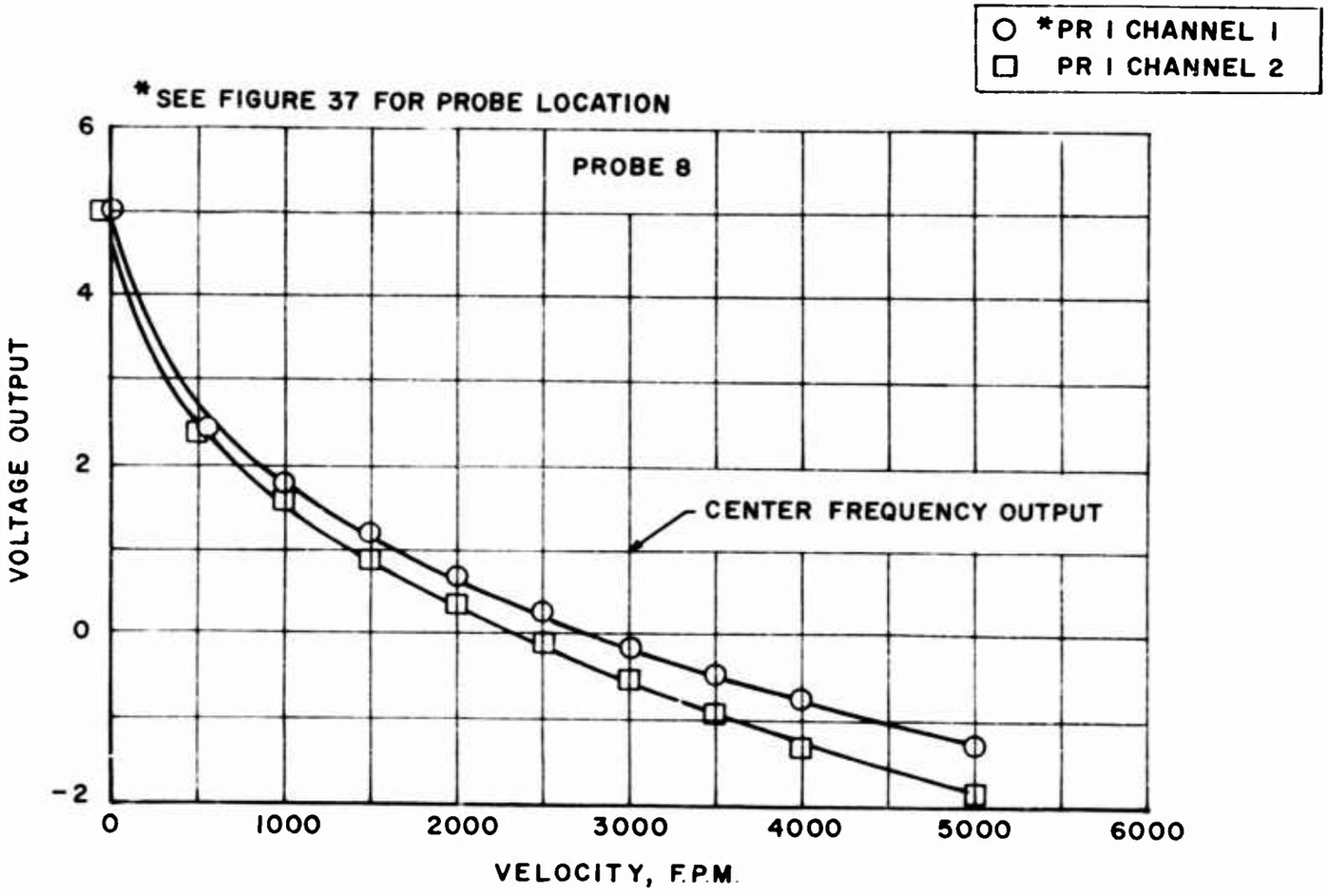

Figure 27. Hot Film Anemometer Calibration, Probe No. 8.

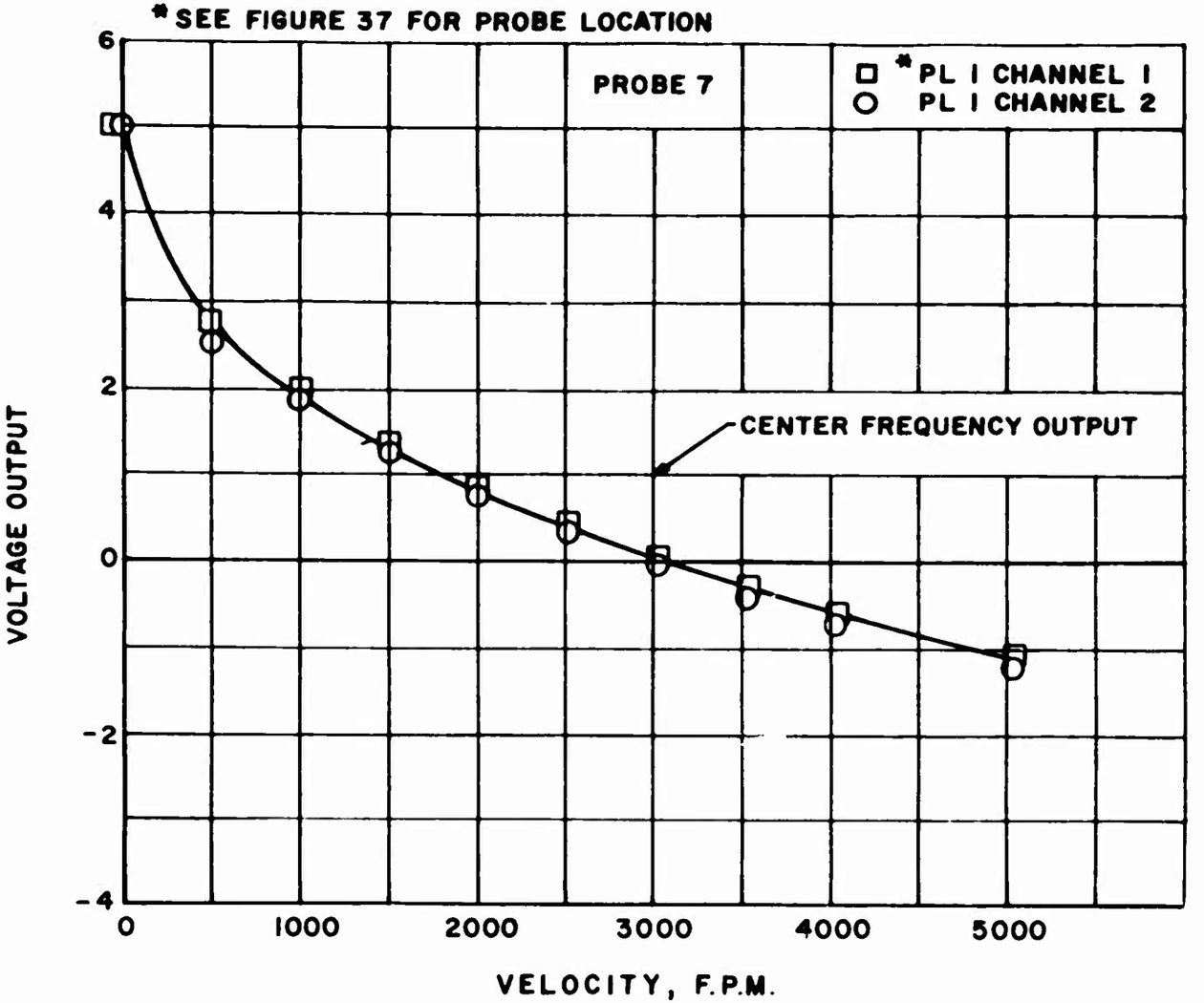

Figure 28. Hot Film Anemometer Calibration, Probe No. 7.

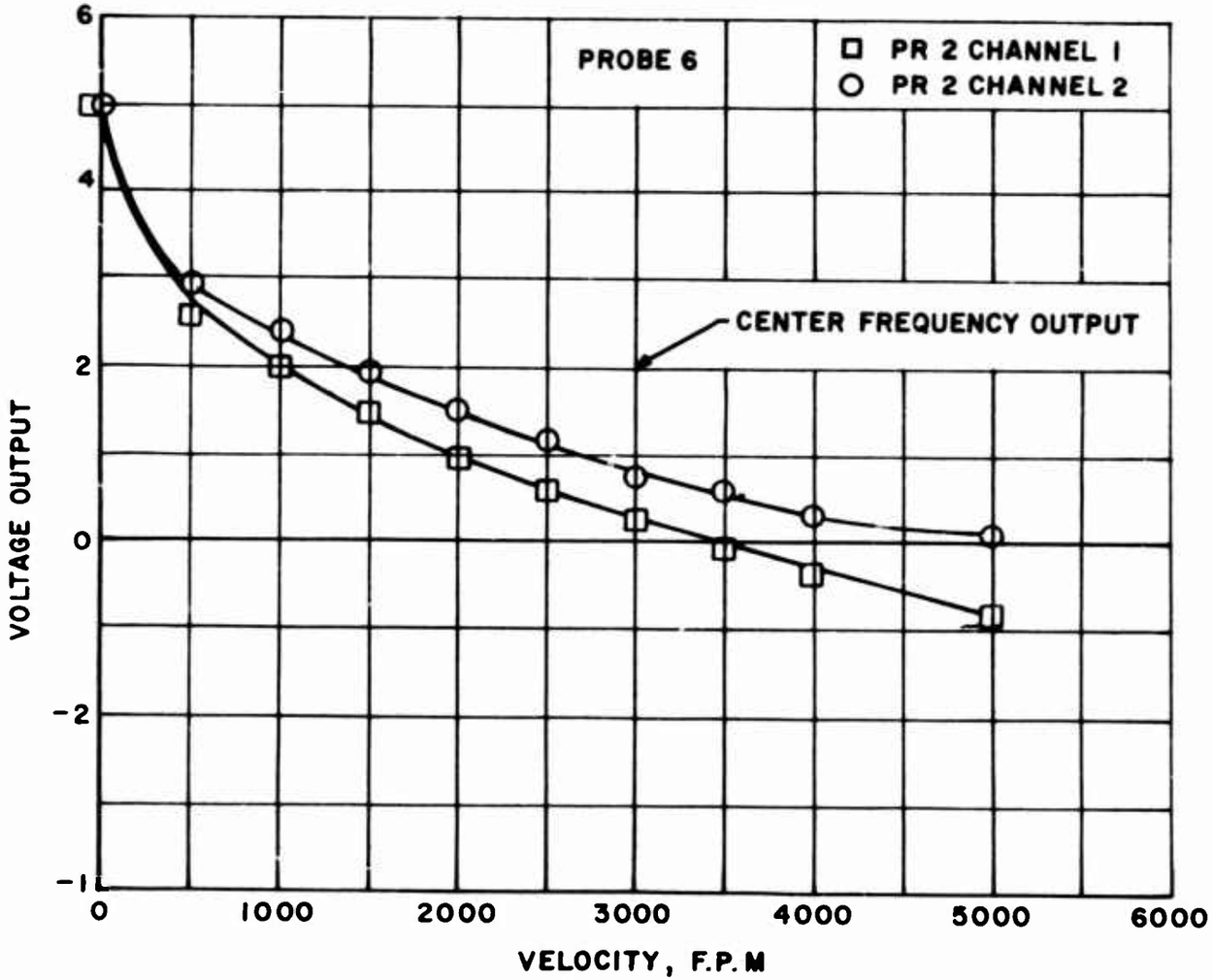

Figure 29. Hot Film Anemometer Calibration, Probe No. 6.

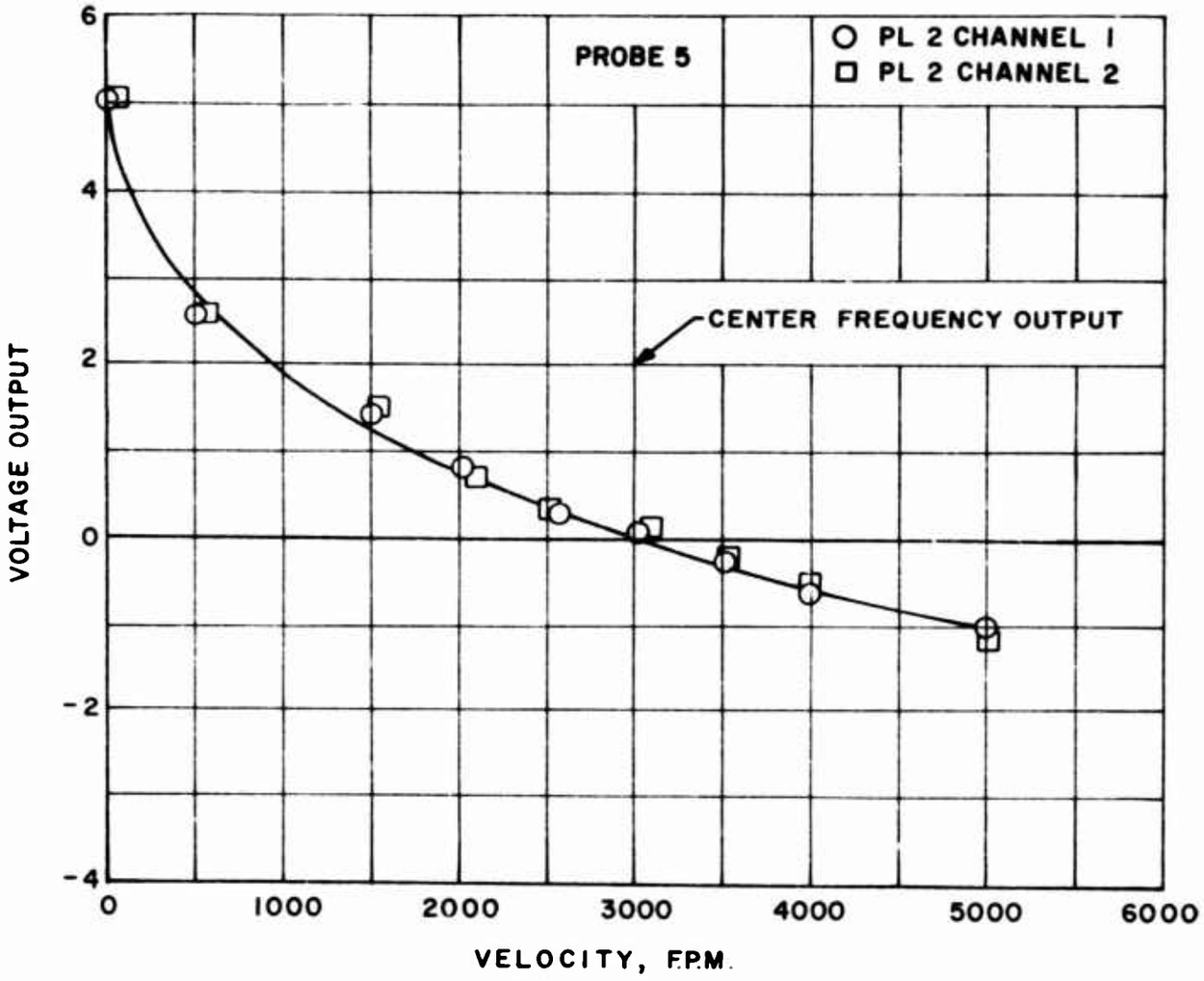

Figure 30. Hot Film Anemometer Calibration, Probe No. 5.

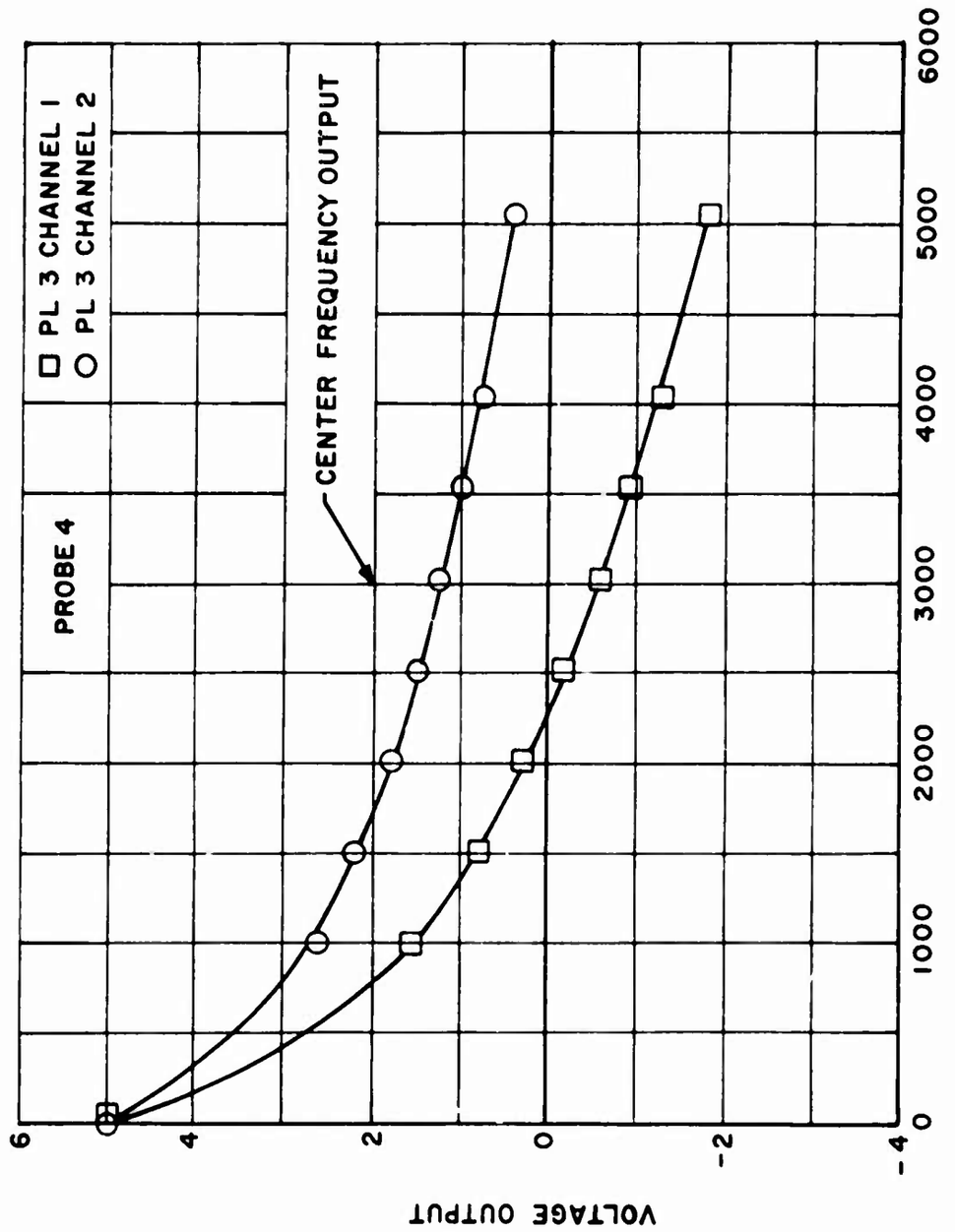

Figure 31. Hot Film Anemometer Calibration, Probe No. 4.

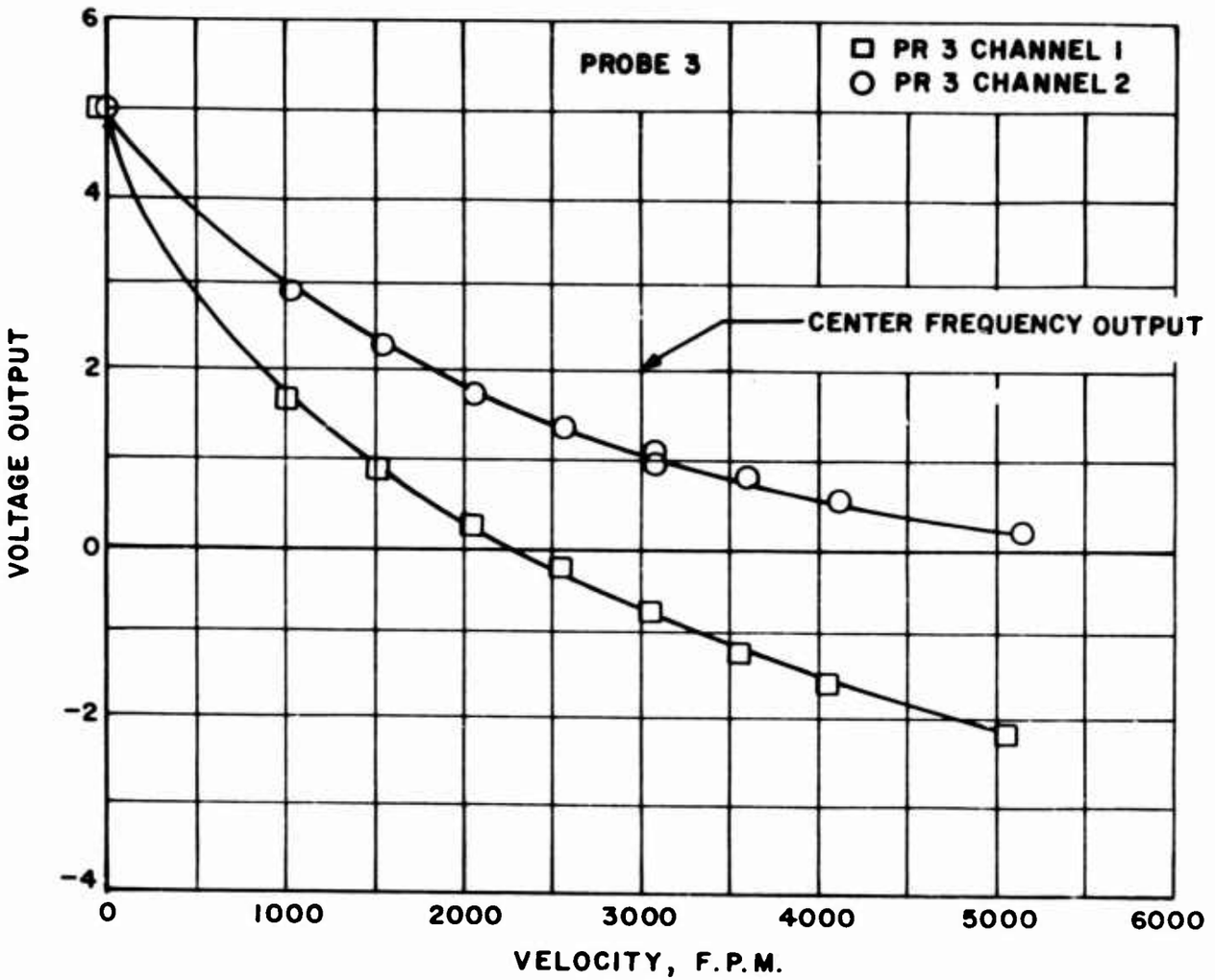

Figure 32. Hot Film Anemometer Calibration, Probe No. 3.

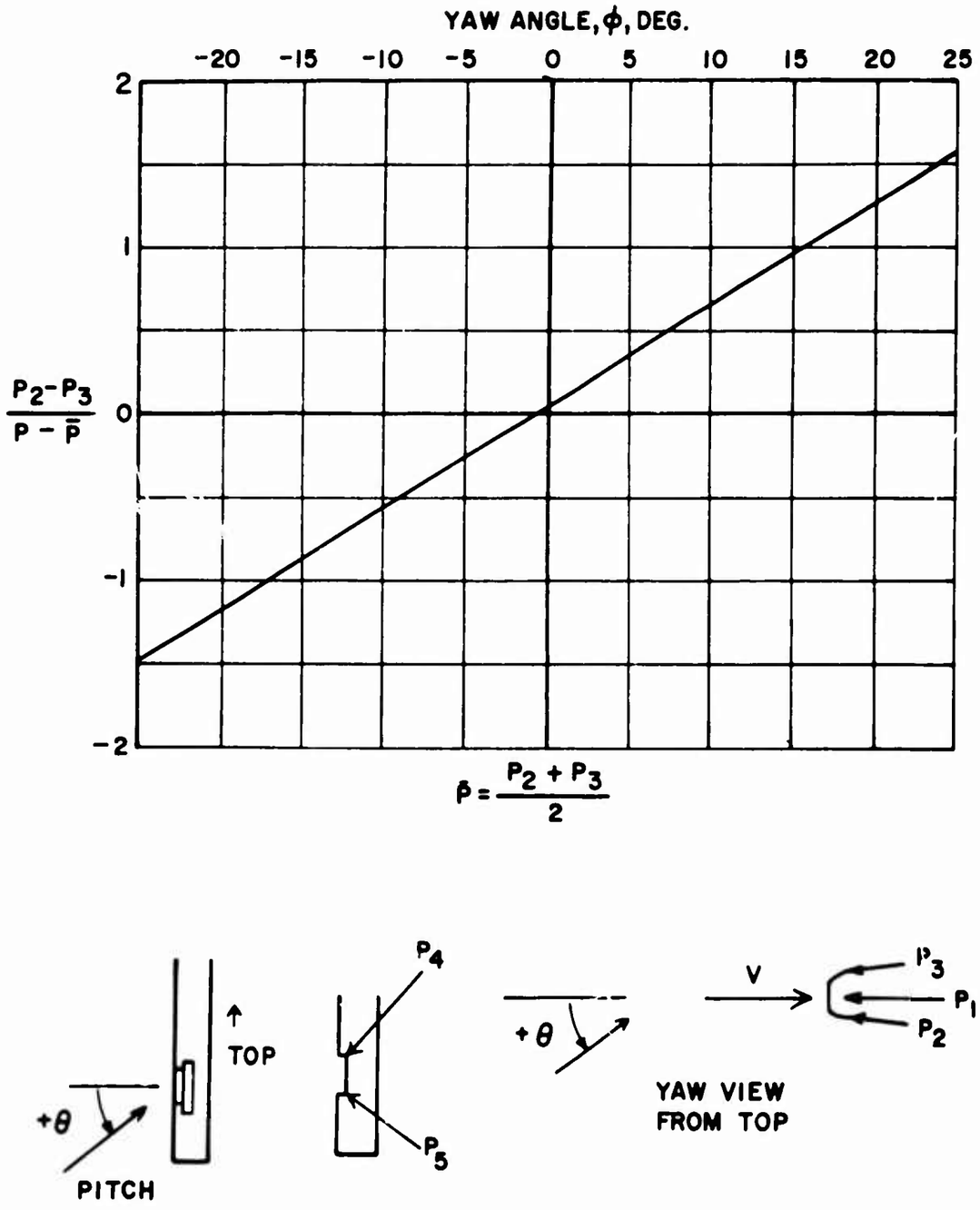

Figure 33. 3-D Pressure Probe, Yaw Angle Calibration.

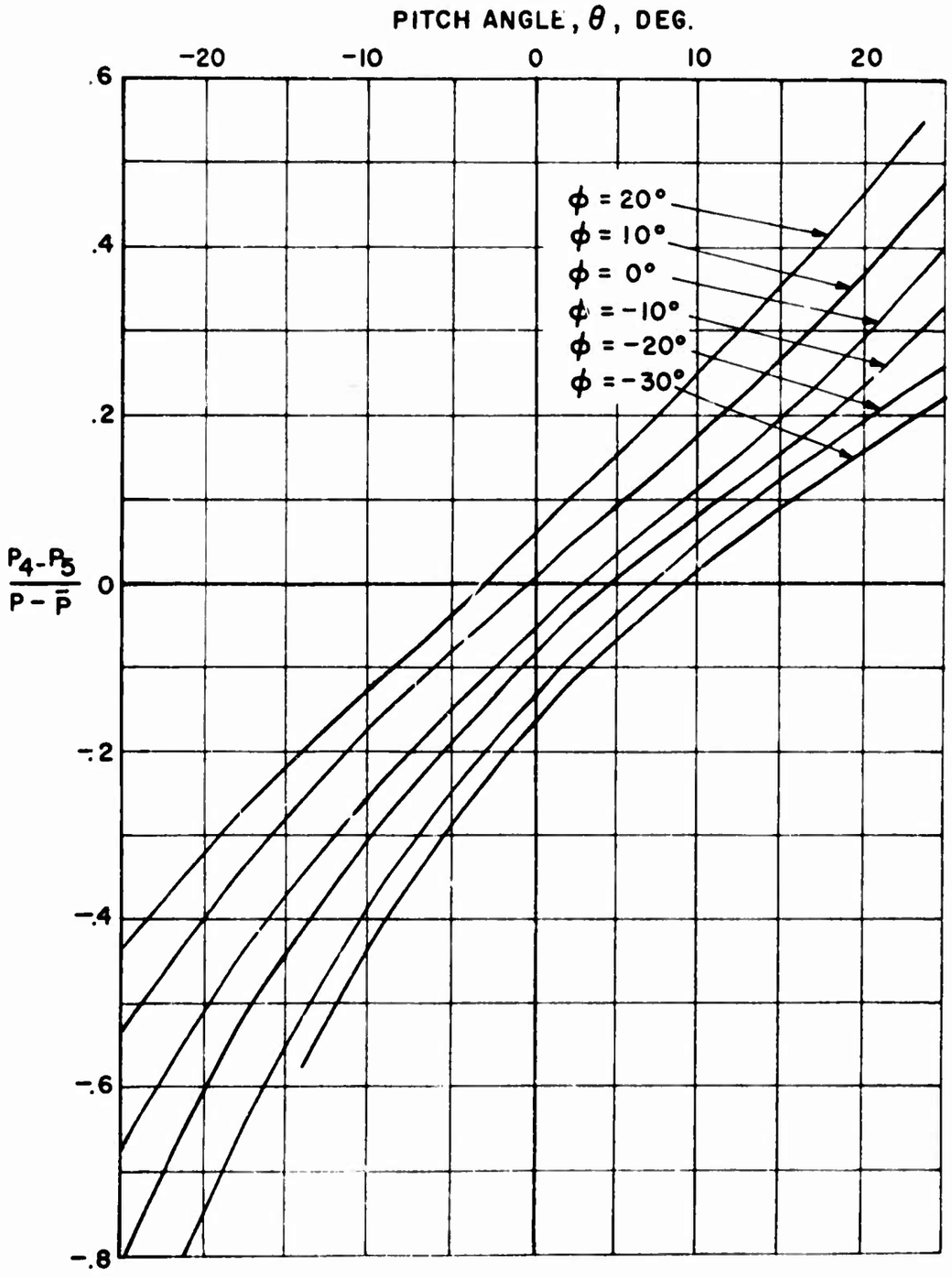

Figure 34. 3-D Pressure Probe, Pitch Angle Calibration.

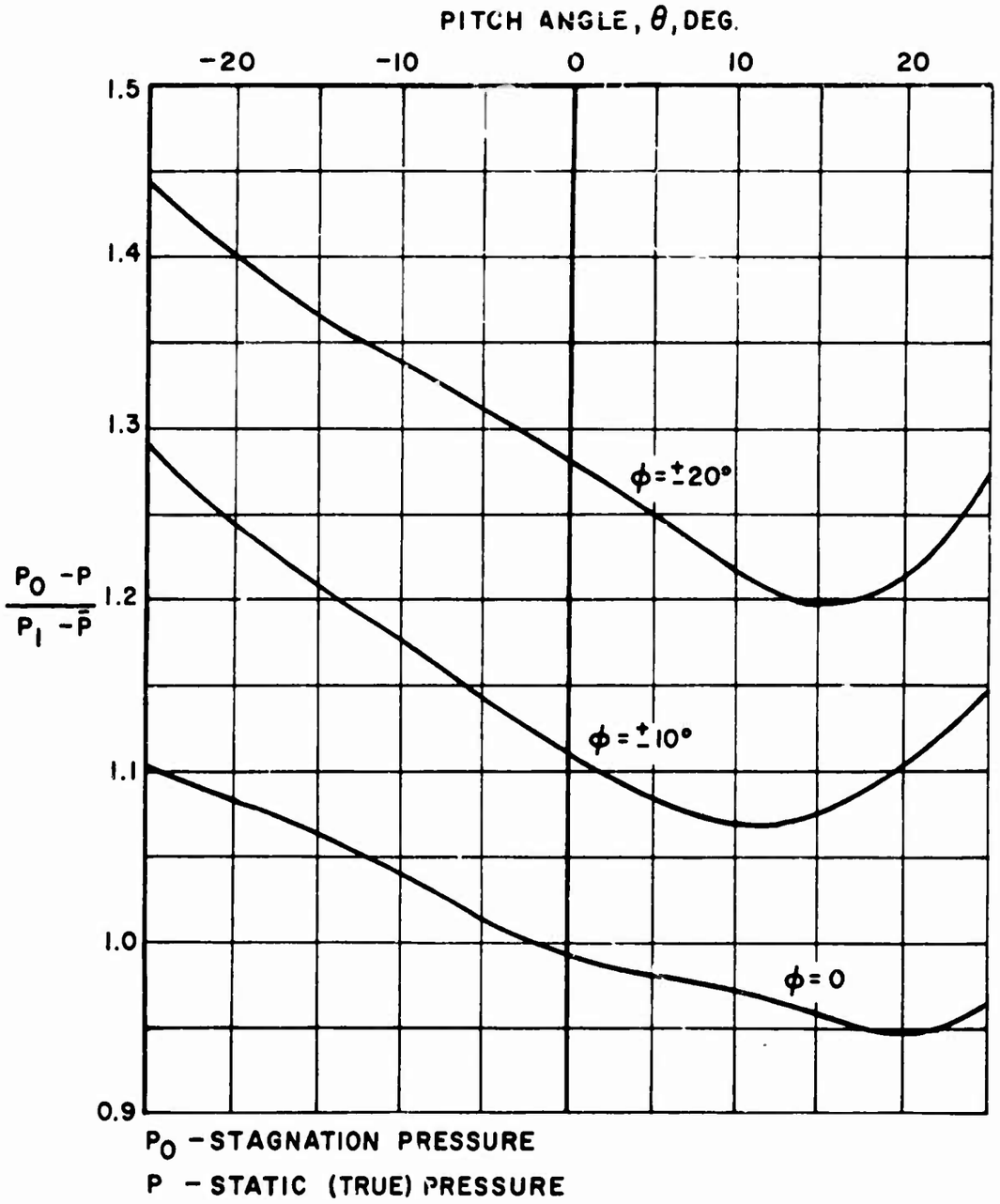

Figure 35. 3-D Pressure Probe, Velocity Head Calibration.

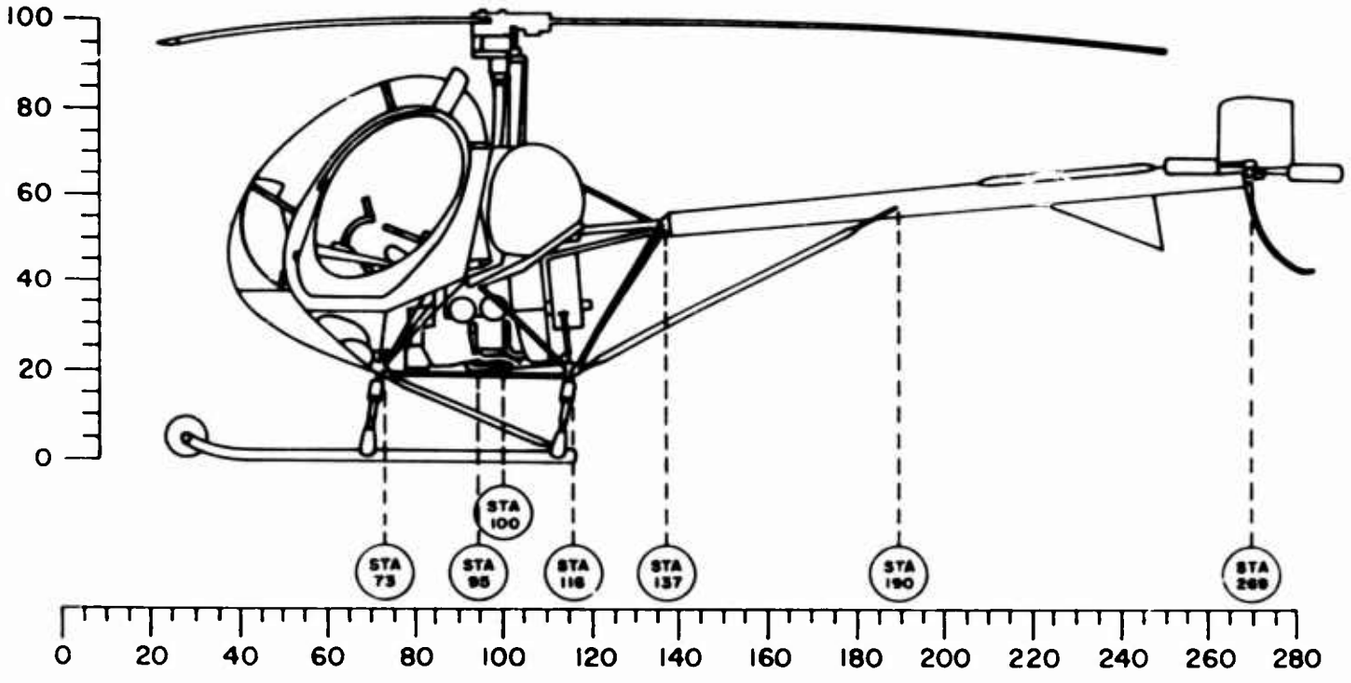

Figure 36. Balance Diagram.

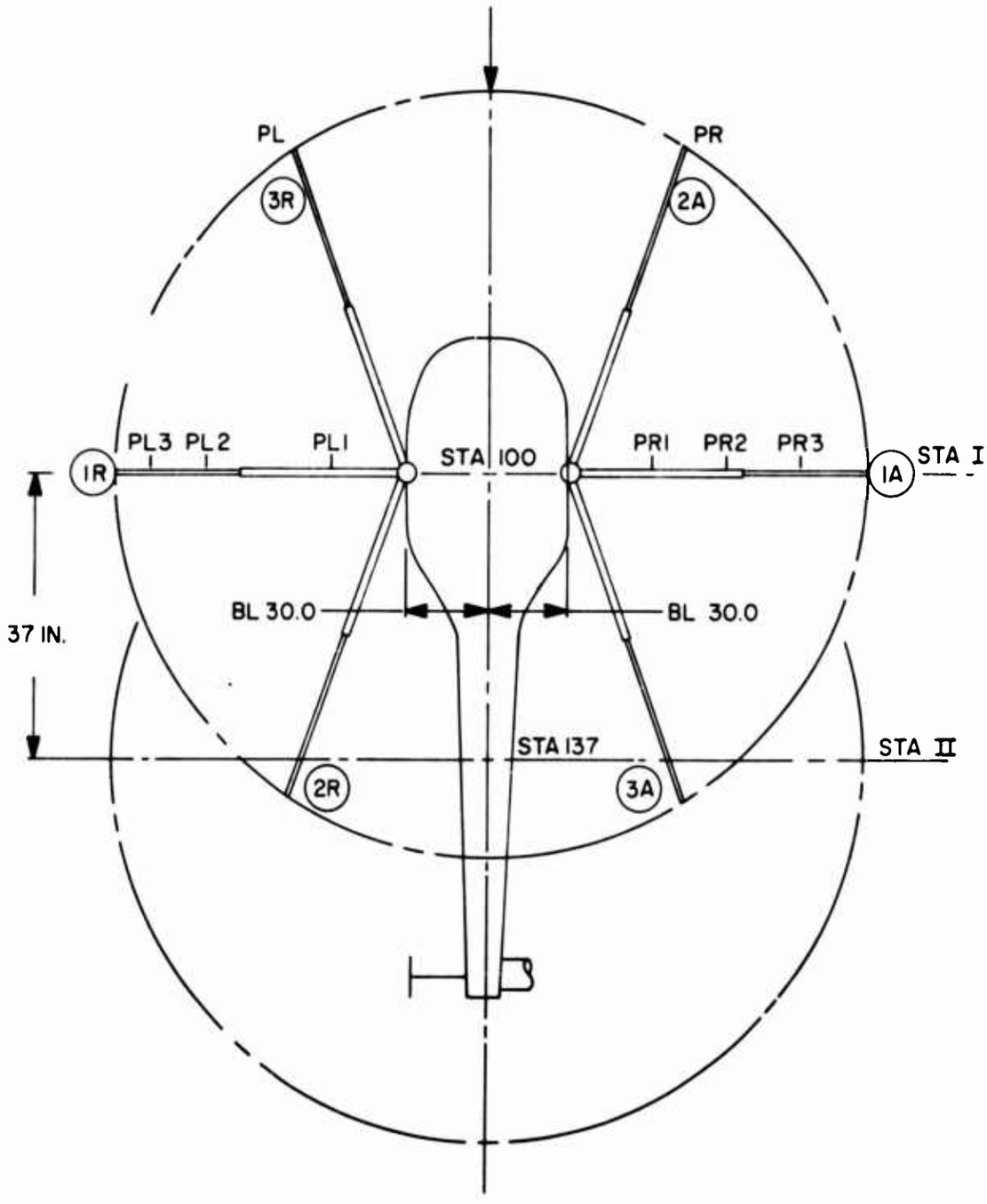

Figure 37. Schematic Diagram of Azimuthal Test Positions.

FLIGHT TEST REPORT

Aircraft Type _____ Flight No. _____

Flight From _____ To _____ Date _____

Time _____ Arrive

Total Gross Weight _____ _____ Leave

Flight Conditions: Altitude _____ Feet

Cruising Speed _____ MPH

Outside Air Temperature _____ °F

Rotor r.p.m. _____

Engine r.p.m. _____

Manifold Pressure _____

Ground Conditions: Ambient Pressure _____ In. Hg.

Ambient Temperature _____ °F

Wind: Direction _____,

Velocity _____

Conditions:

Clear _____ Rain _____

Dusty _____ Snow _____

Cloudy _____ Hail _____

Other _____

Boom Configuration:

Remarks:

Figure 38. Flight Test Data Sheet

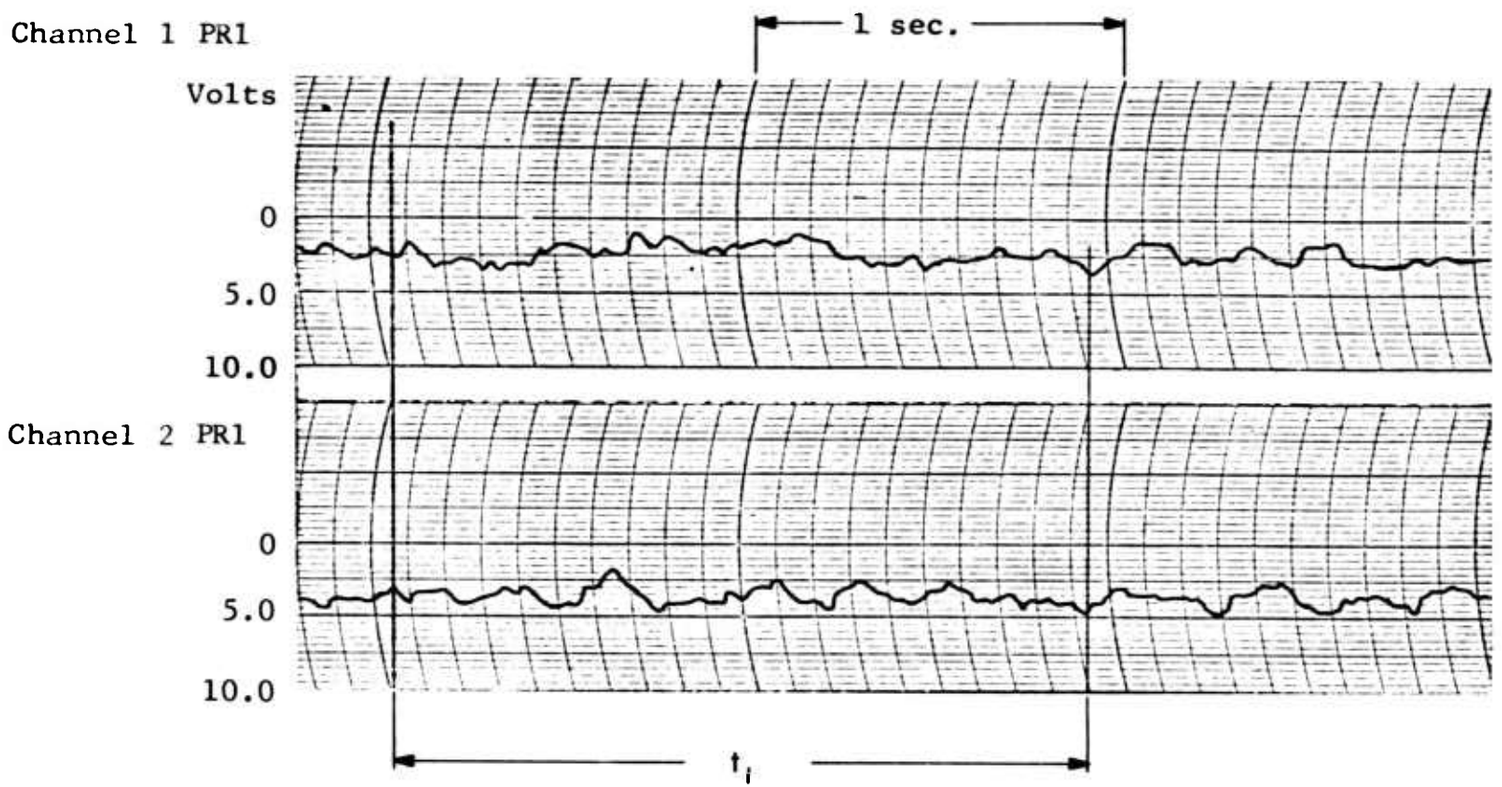

Figure 39. Typical Brush Recordings of Hot Film Data.

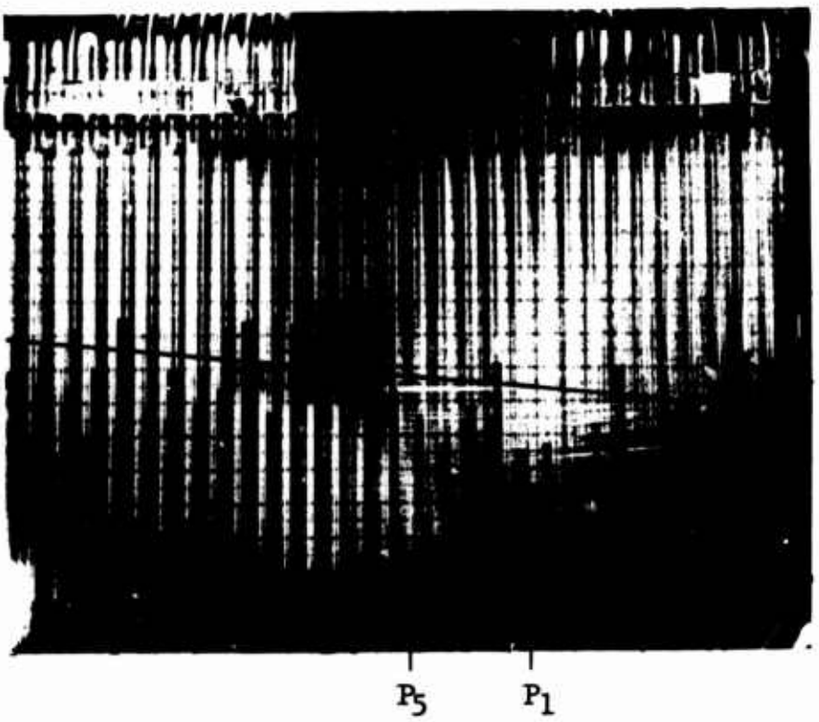

Figure 40. Typical Photograph of Steady-State Velocity Data.

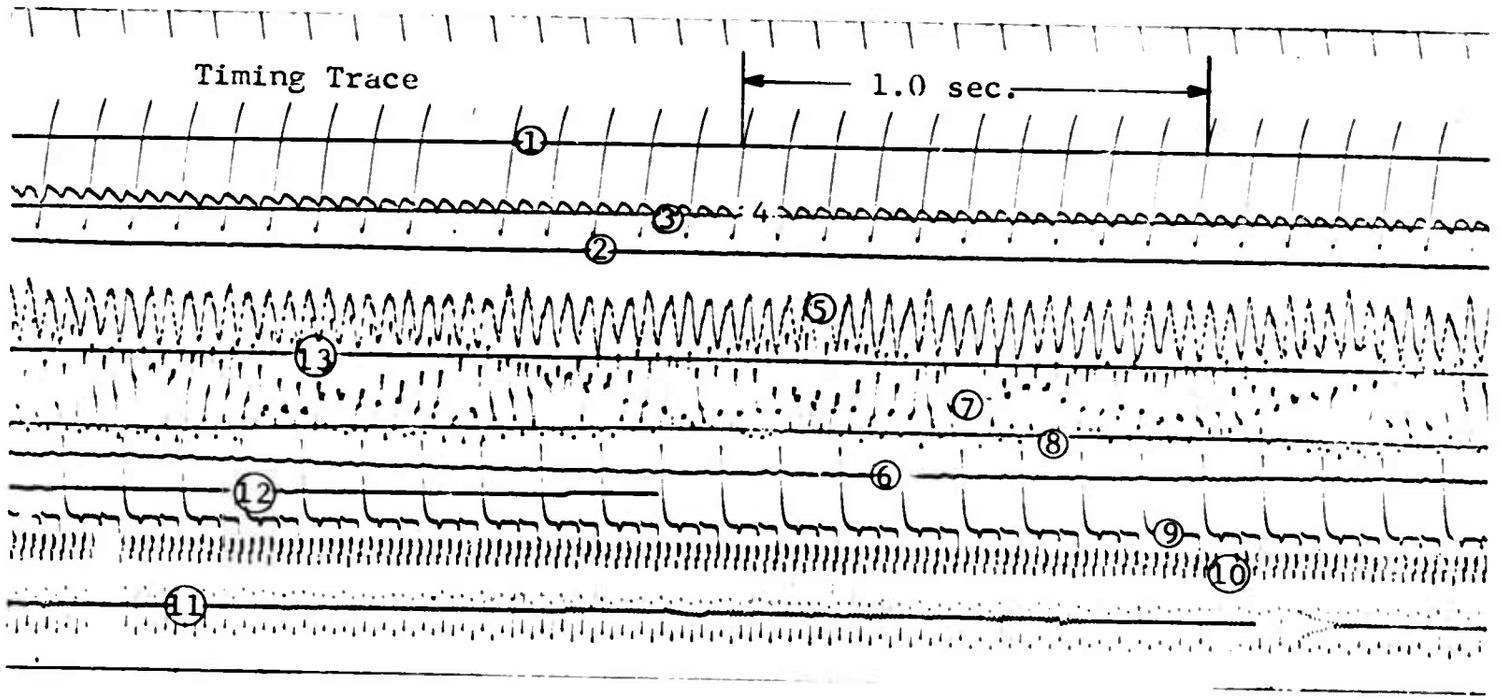

Legend:

1. Reference
2. Collective Stick
3. Altitude
4. Manifold Pressure
5. Airspeed
6. Fuselage Attitude
7. Accelerometer
8. Longitudinal Cyclic
9. Rotor r.p.m.
10. Engine r.p.m.
11. Common Time
12. Probe Correlation
13. Reference

Figure 41. Typical Oscillogram of Helicopter Parameters.

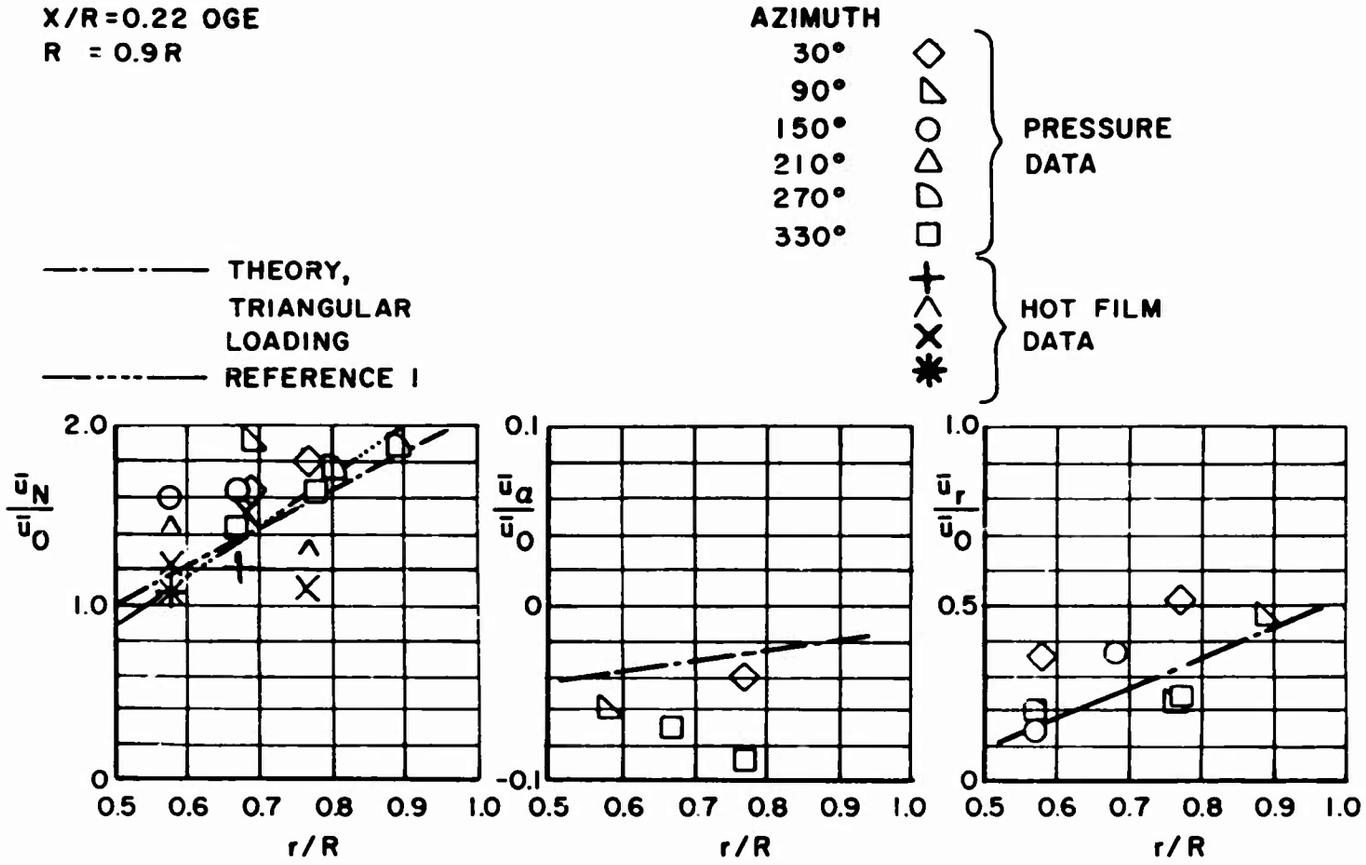

Figure 42. Measured Induced Velocities in the Rotor Wake, Hovering, x/R = 0.22 (Time Averaged).

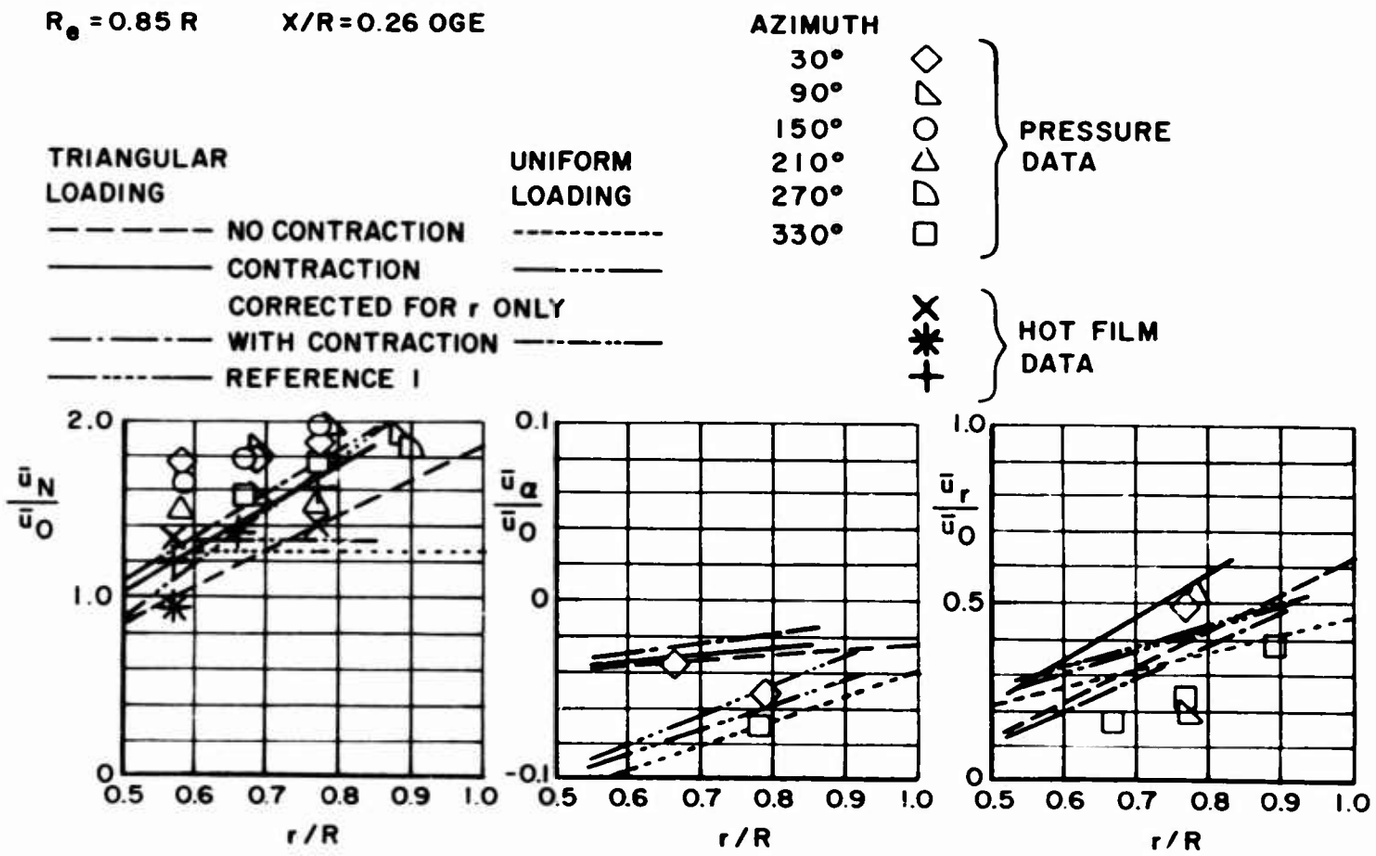

Figure 43. Measured Induced Velocities in the Rotor Wake, x/R = 0.26 (Time Averaged).

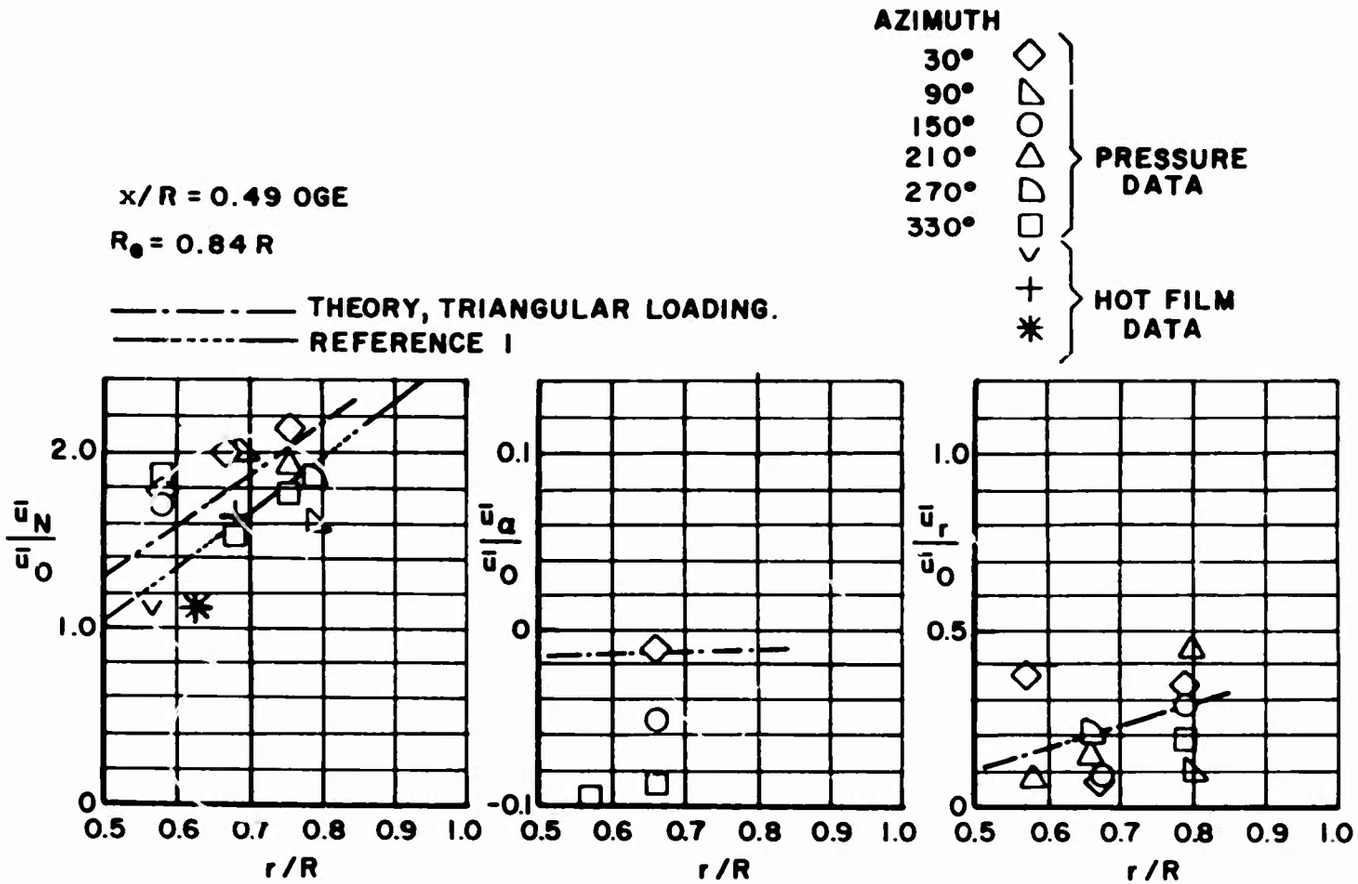

Figure 44. Measured Induced Velocities in the Rotor Wake, Hovering, x/R = 0.49 (Time Averaged).

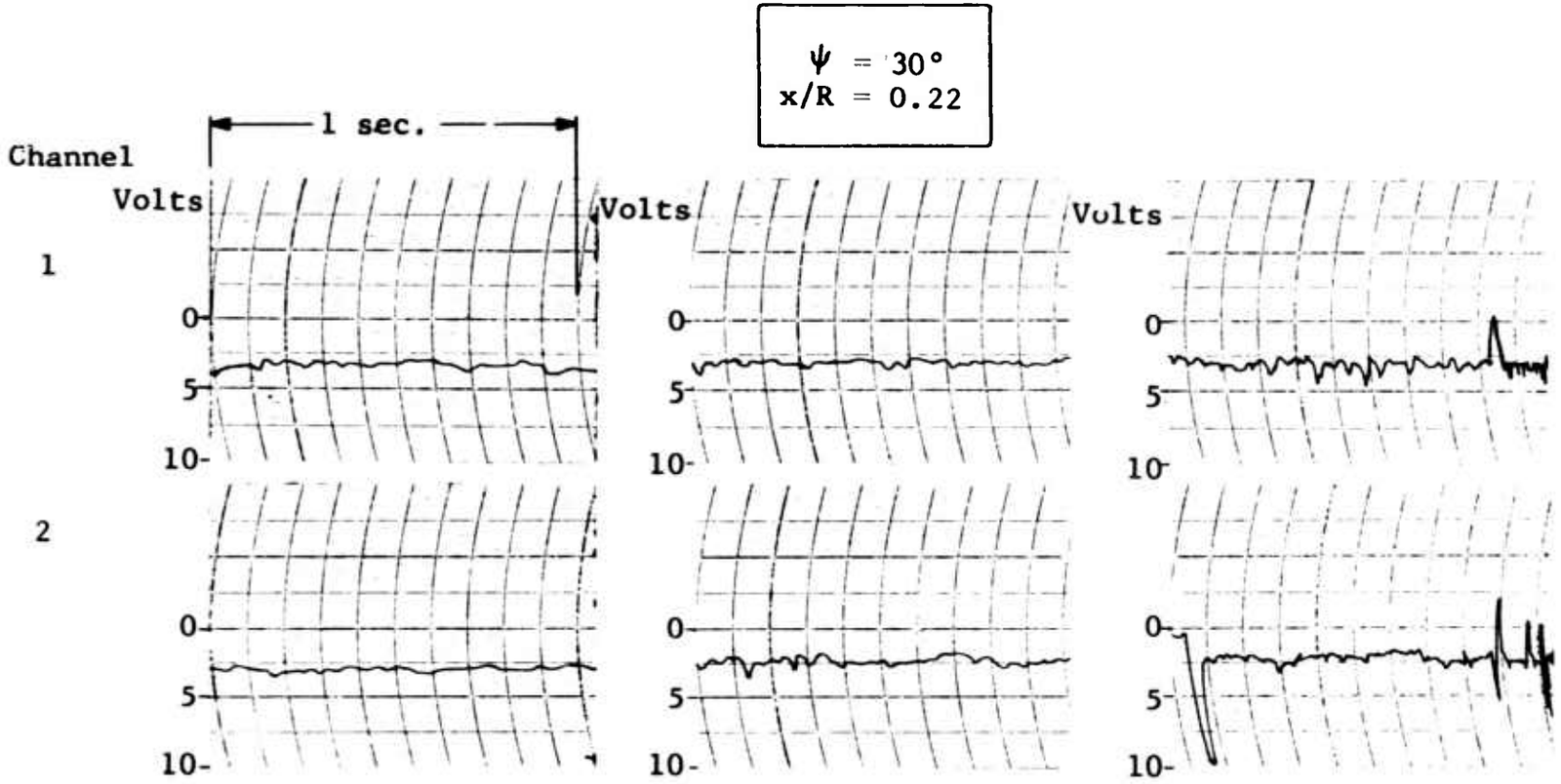

Figure 45. Variation of Instantaneous Velocity During Hovering, OGE, $\psi = 30°$, $x/R = 0.22$.

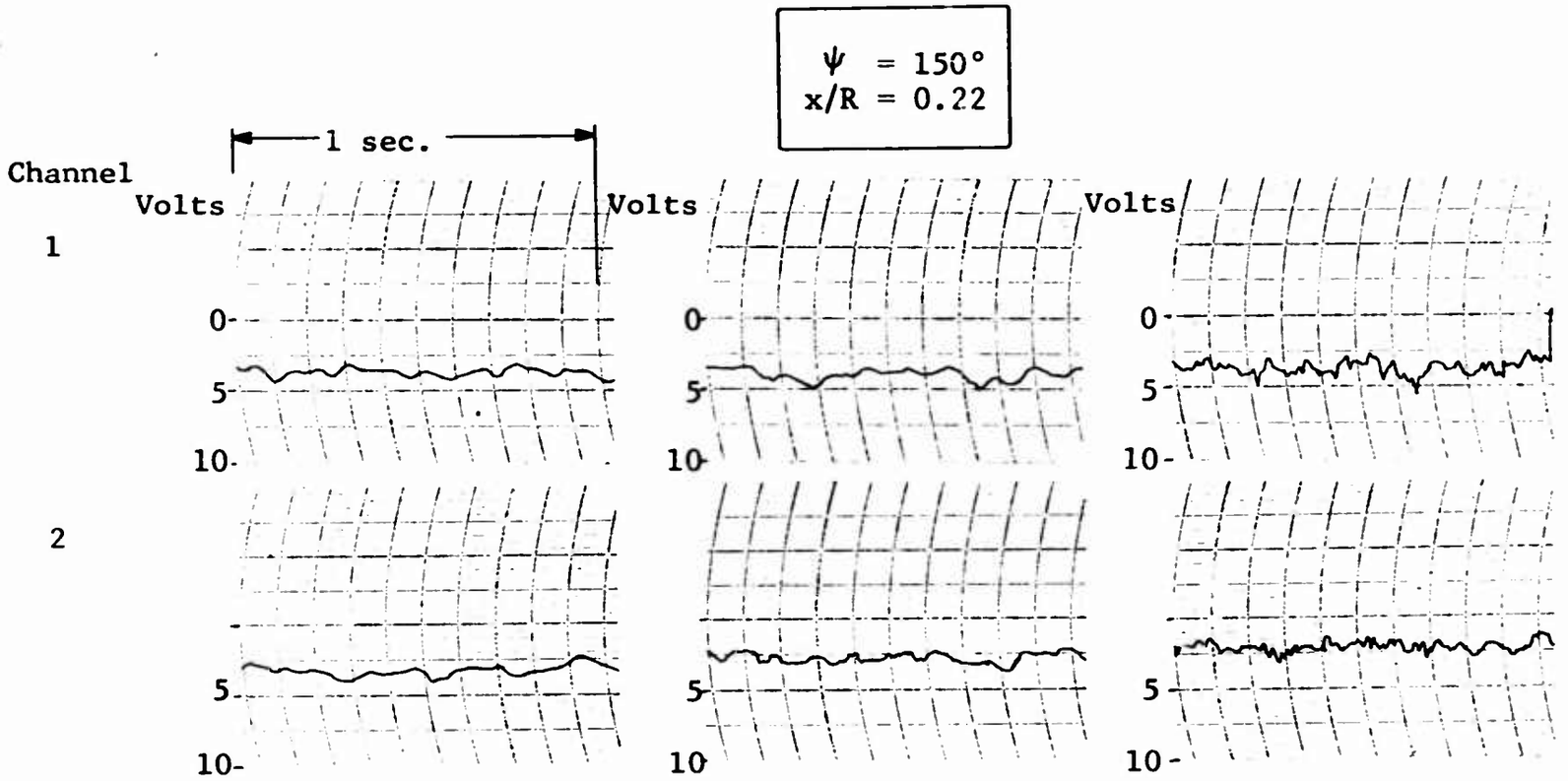

Figure 46. Variation of Instantaneous Velocity During Hovering, OGE, ψ = 150°, x/R = 0.22.

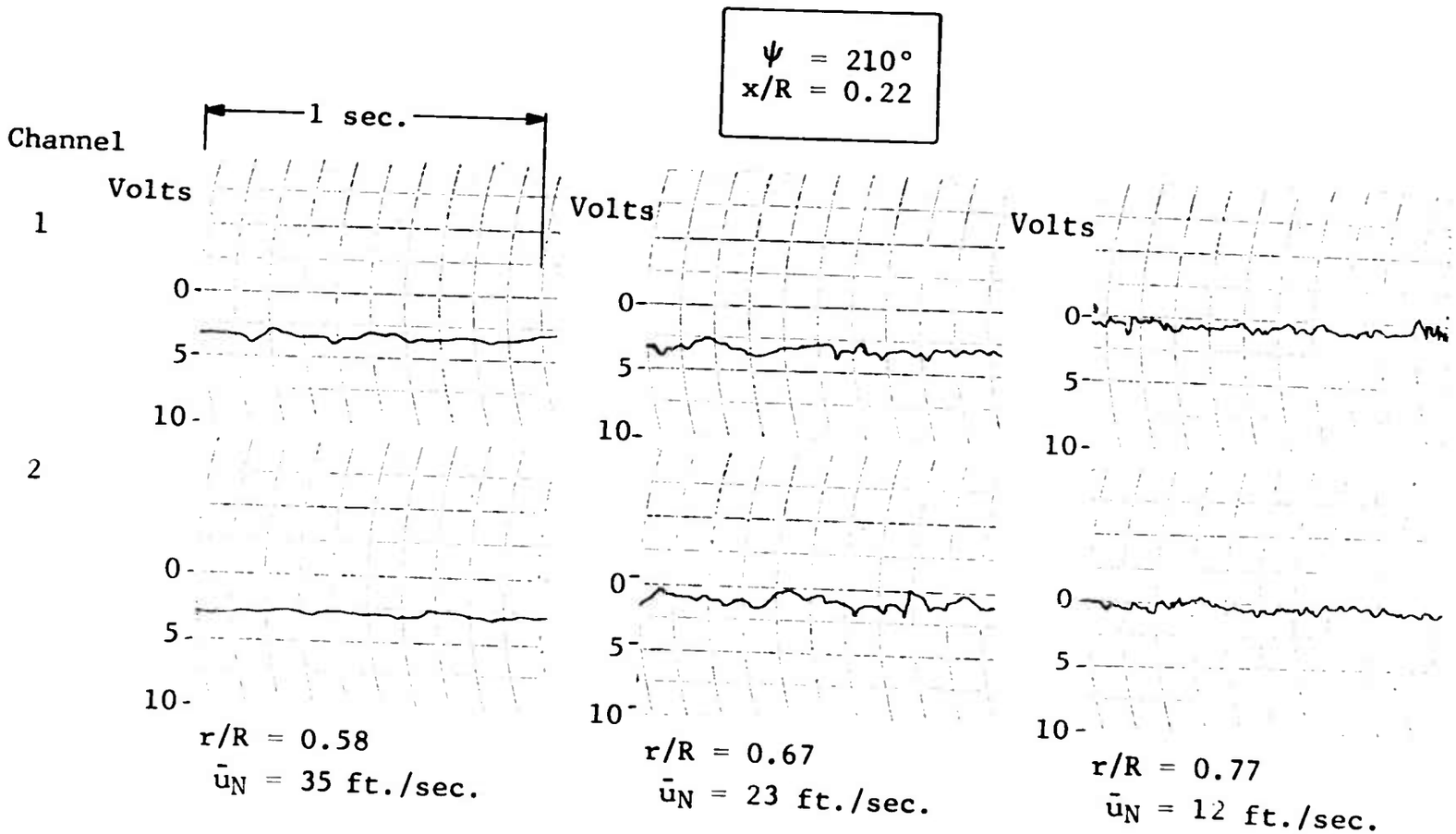

Figure 47. Variation of Instantaneous Velocity During Hovering, OGE, ψ = 210°, x/R = 0.22.

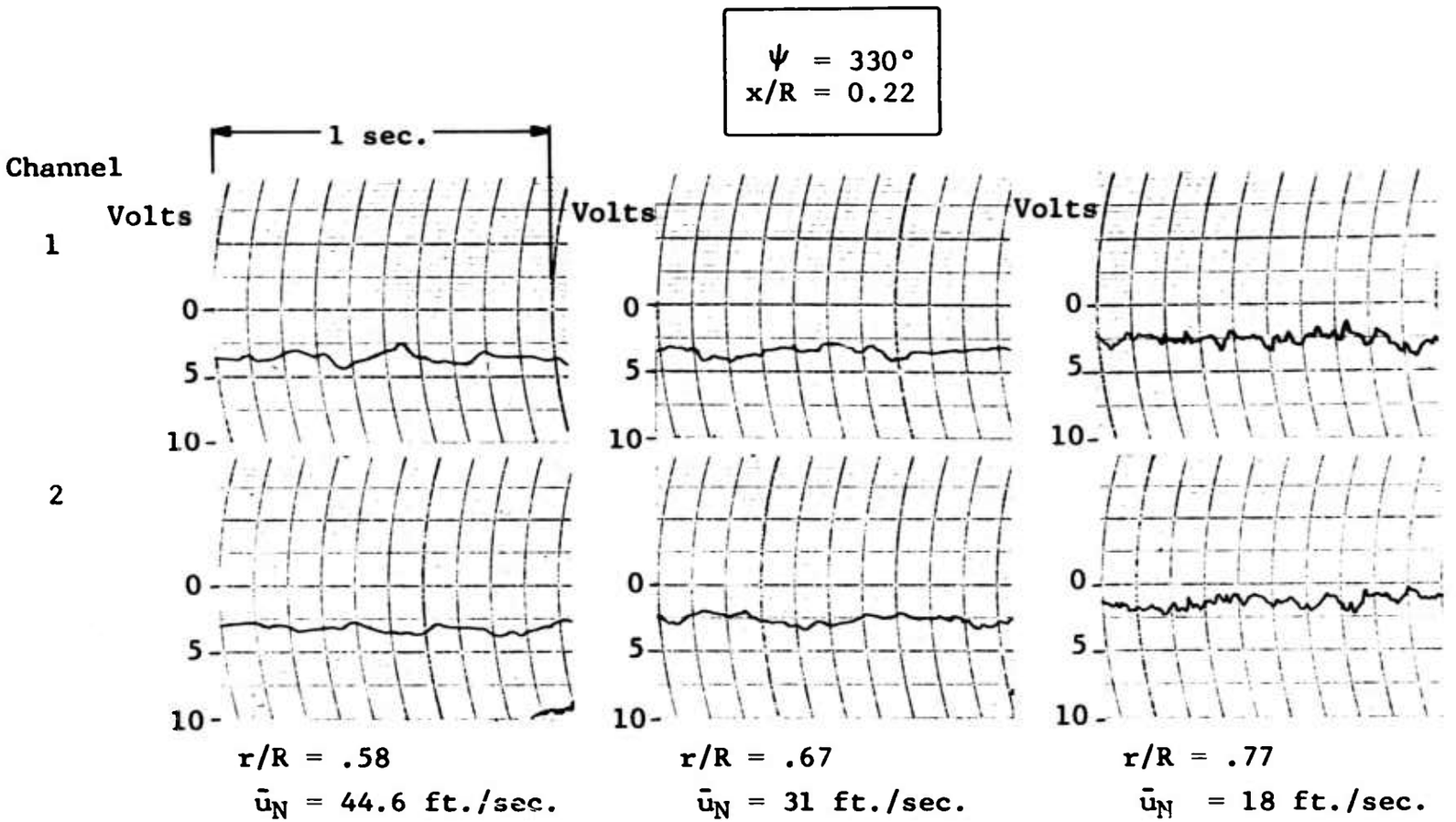

Figure 48. Variation of Instantaneous Velocity During Hovering, OGE, ψ = 330°, x/R = 0.22.

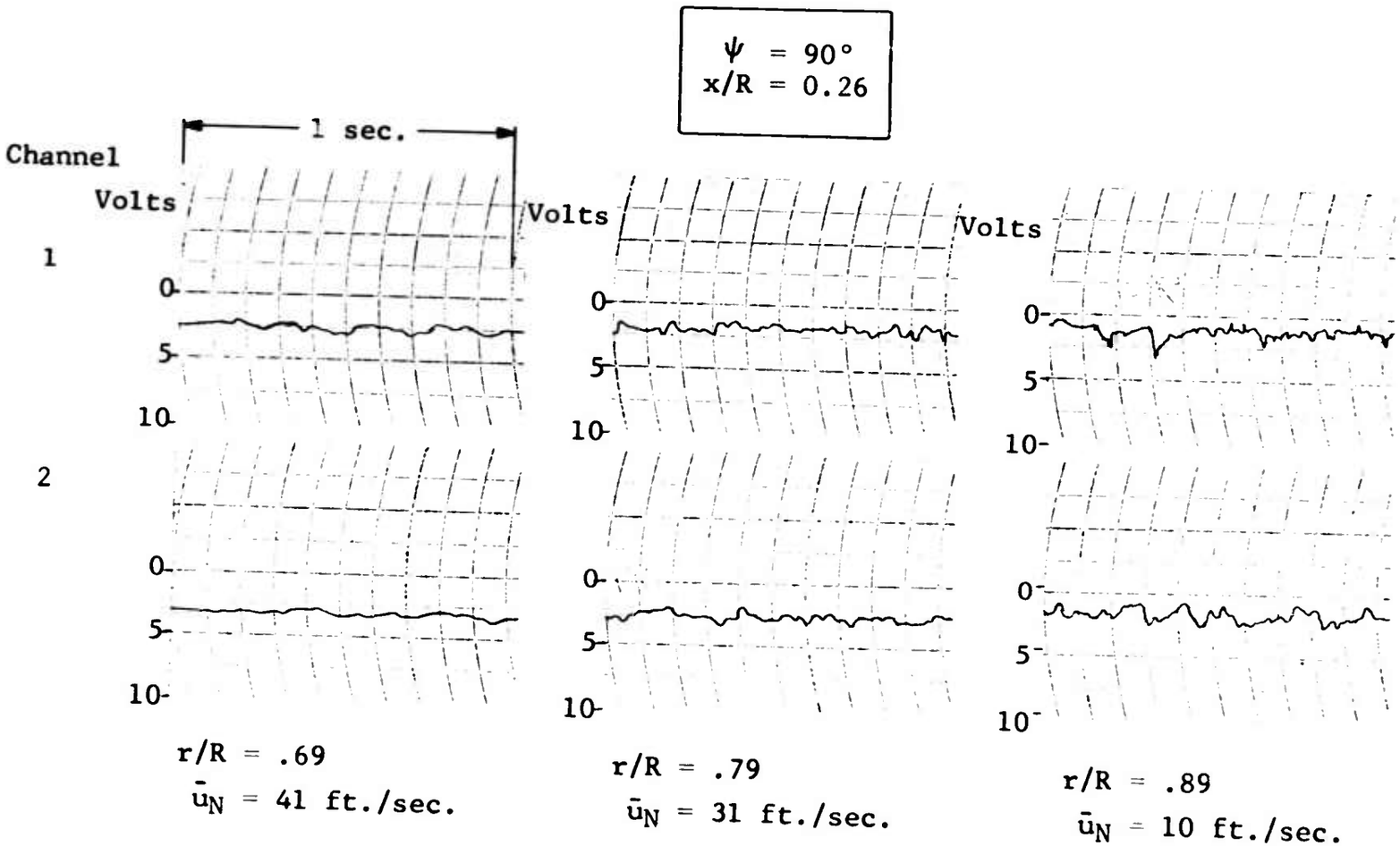

Figure 49. Variation of Instantaneous Velocity During Hovering, OGE, $\psi = 90°$, $x/R = 0.26$.

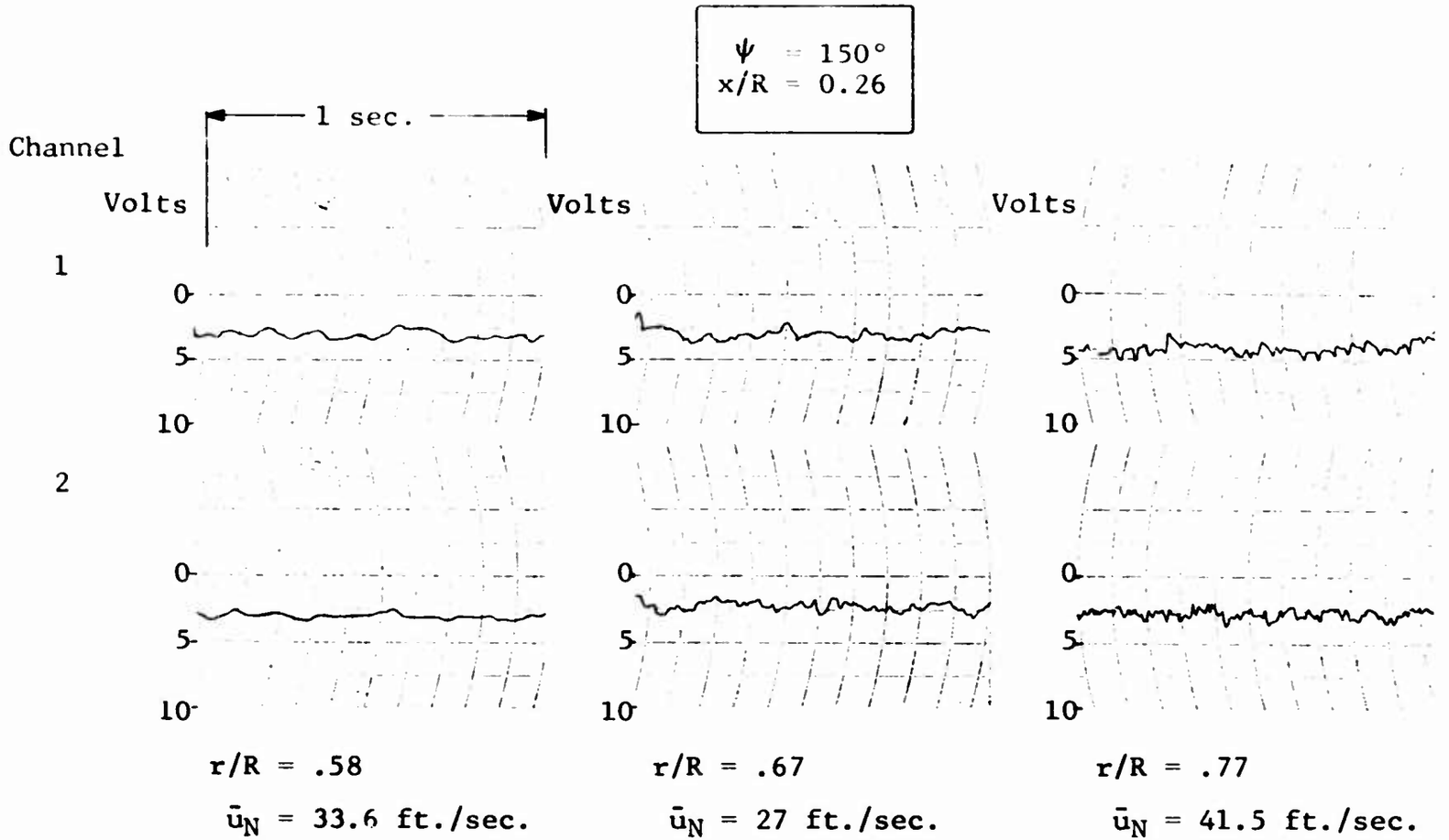

Figure 49a. Variation of Instantaneous Velocity During Hovering, OGE, ψ = 150°, x/R = 0.26.

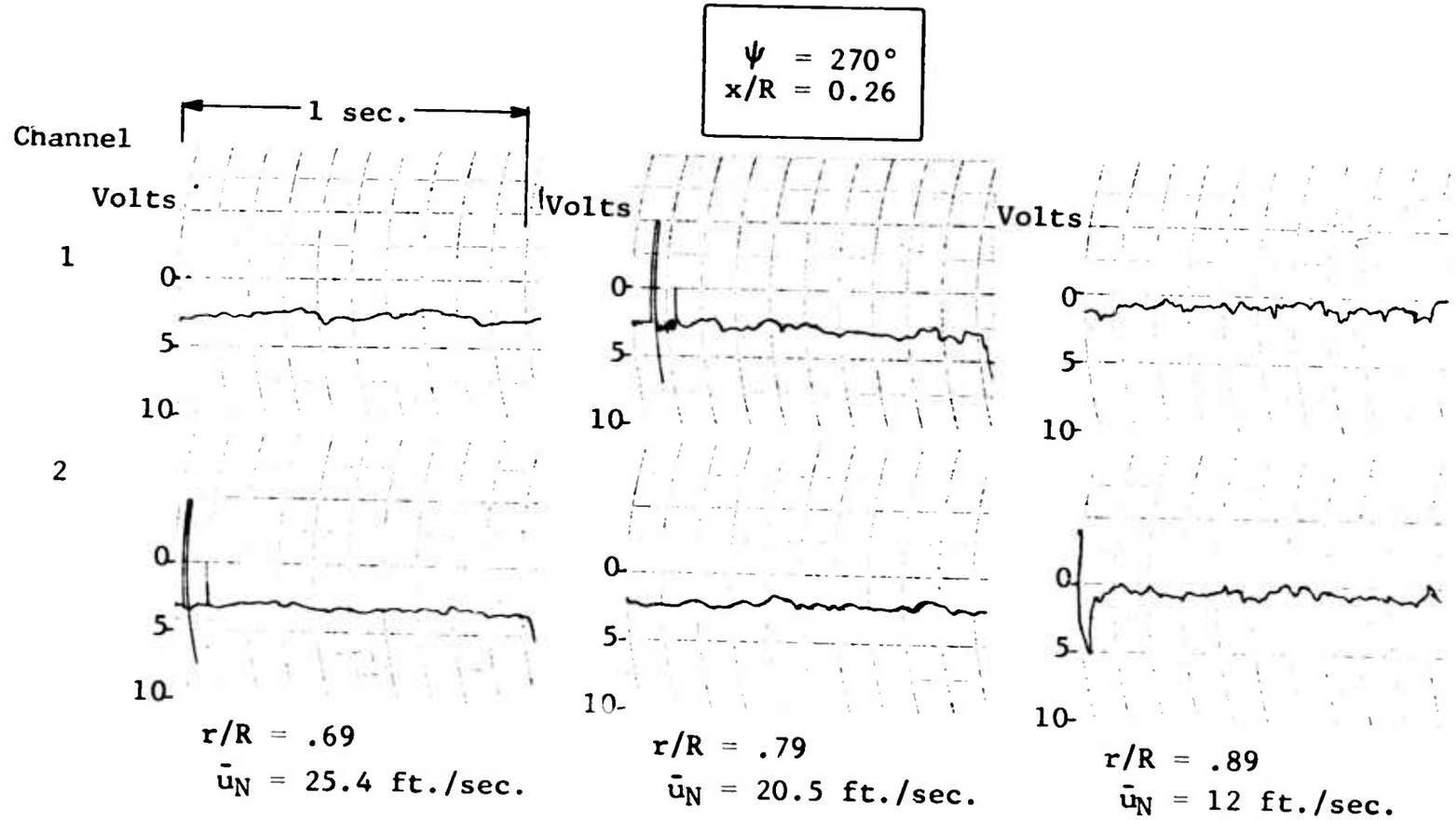

Figure 50. Variation of Instantaneous Velocity During Hovering, OGE, ψ = 270°, x/R = 0.26.

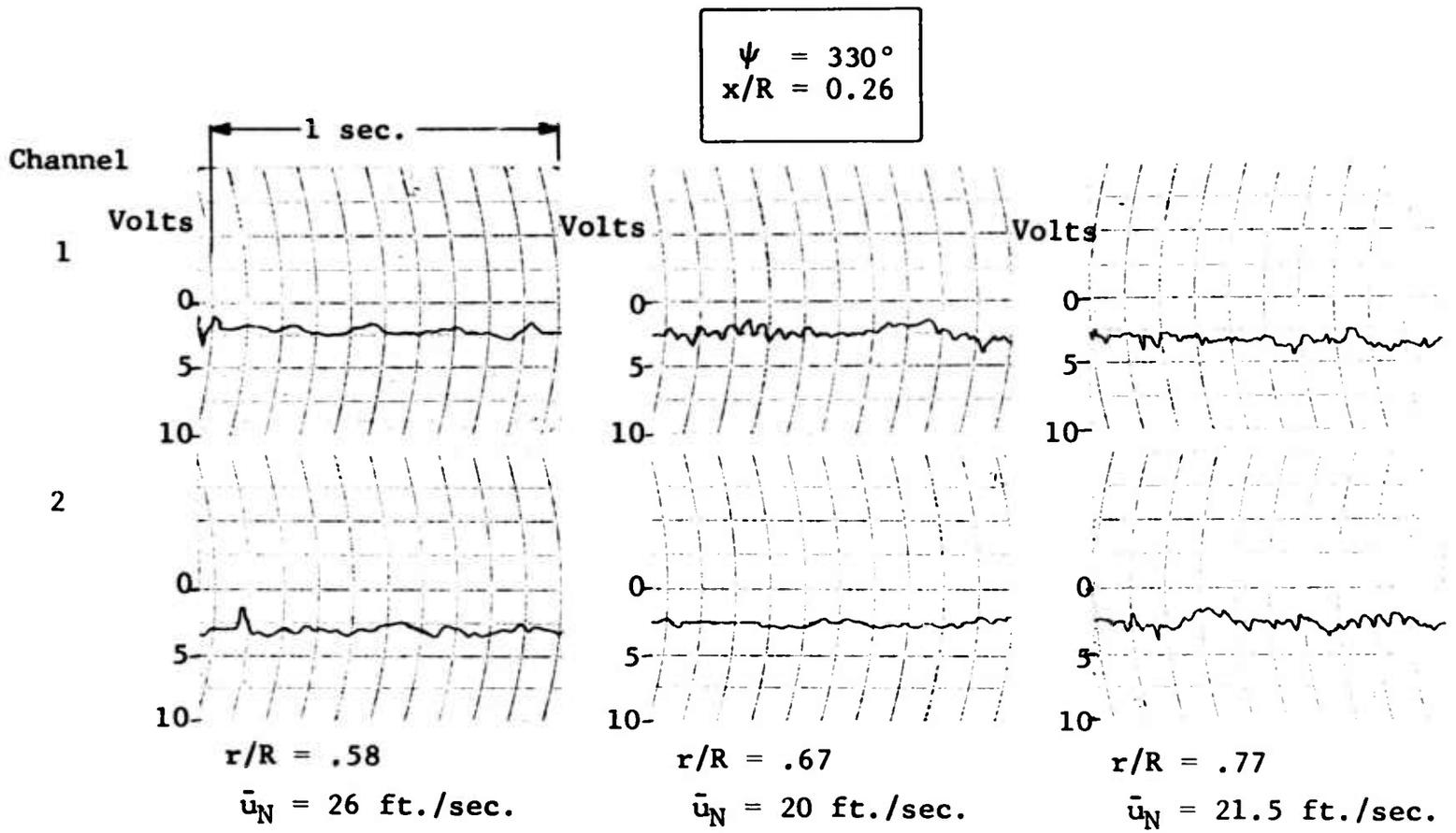

Figure 51. Variation of Instantaneous Velocity During Hovering, OGE, ψ = 330°, x/R = 0.26.

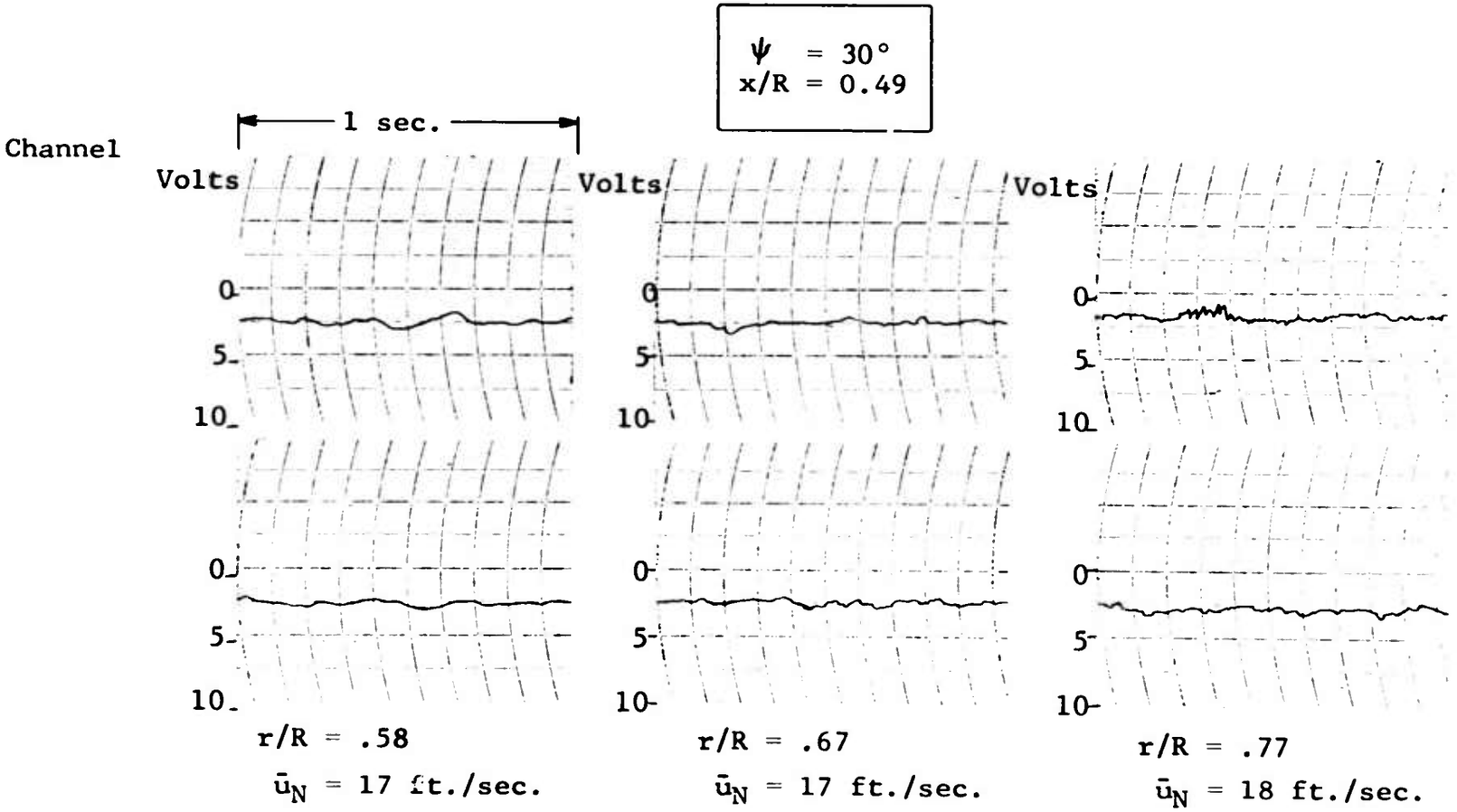

Figure 52. Variation of Instantaneous Velocity During Hovering, OGE, ψ = 30°, x/R = 0.49.

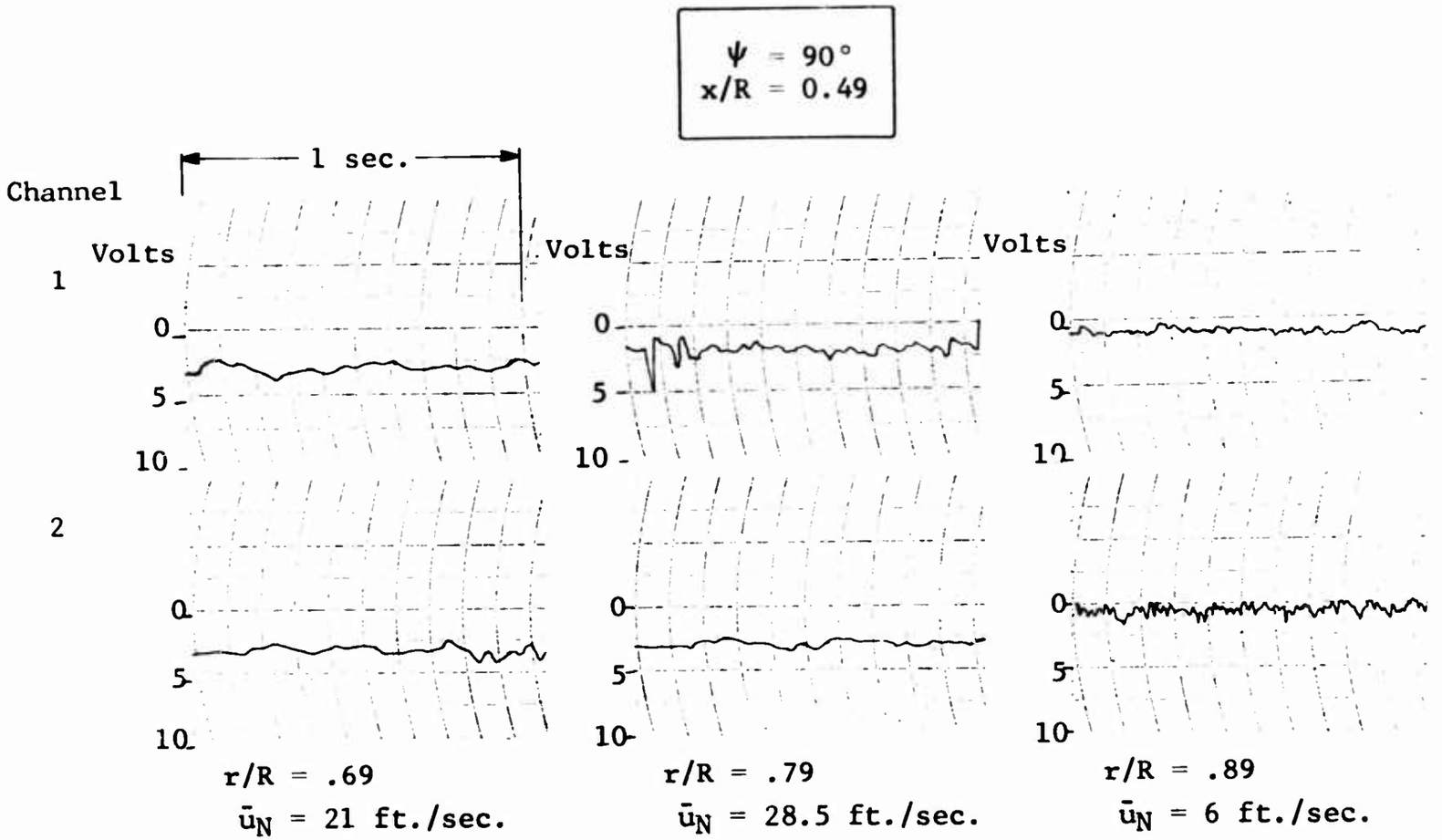

Figure 53. Variation of Instantaneous Velocity During Hovering, OGE, ψ = 90°, x/R = 0.49.

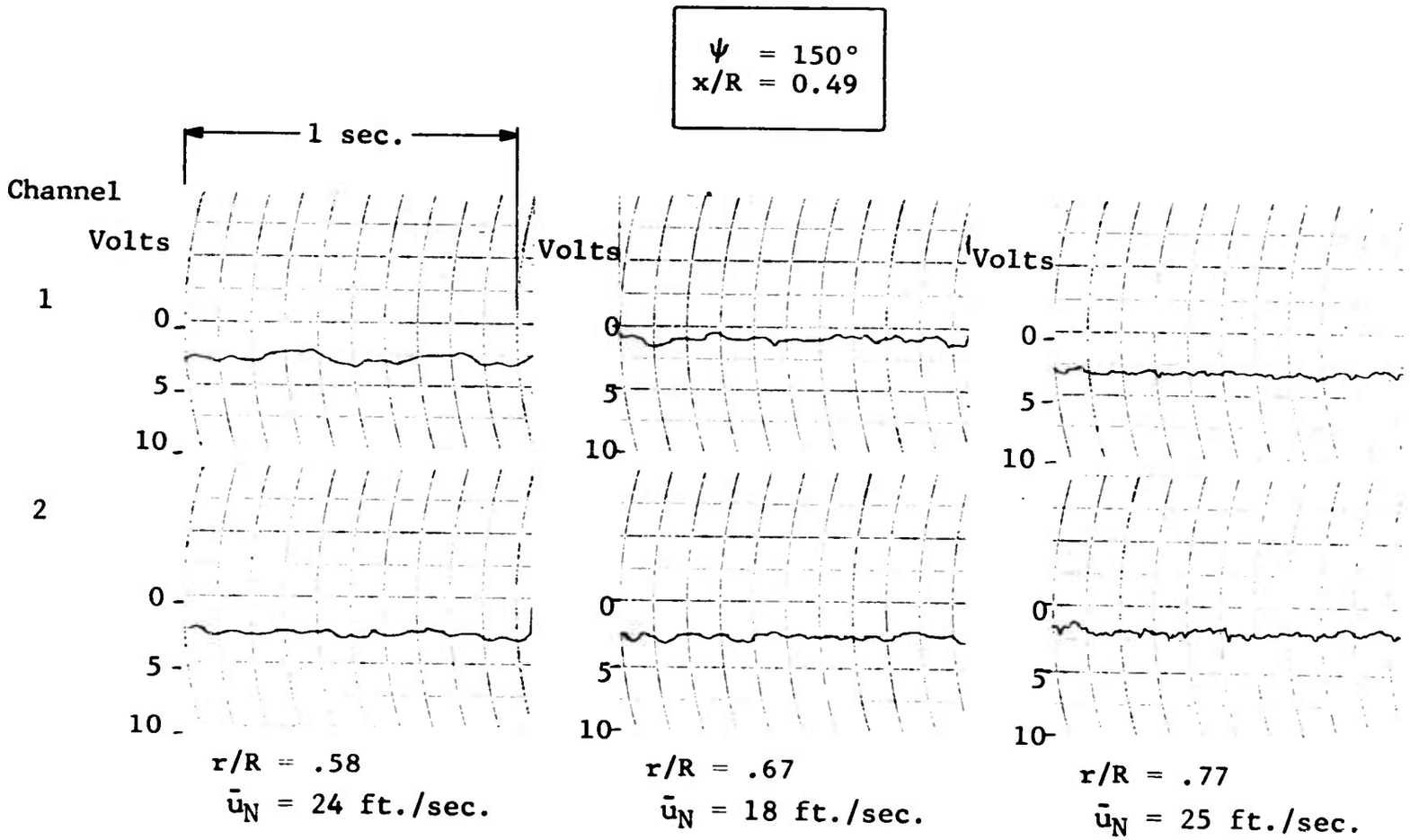

Figure 54. Variation of Instantaneous Velocity During Hovering, OGE, ψ = 150°, x/R = 0.49.

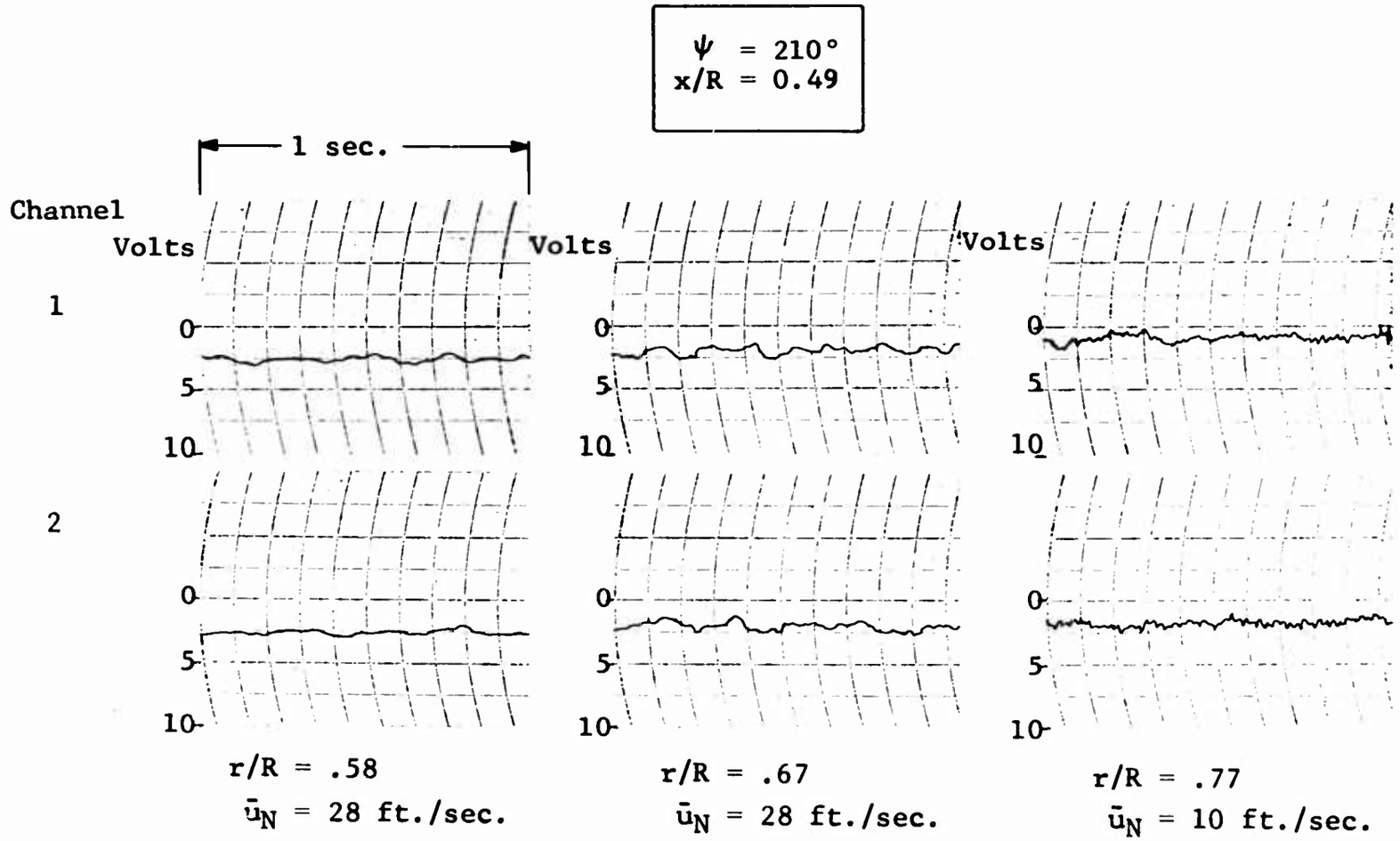

Figure 55. Variation of Instantaneous Velocity During Hovering, OGE, ψ = 210°, x/R = 0.49.

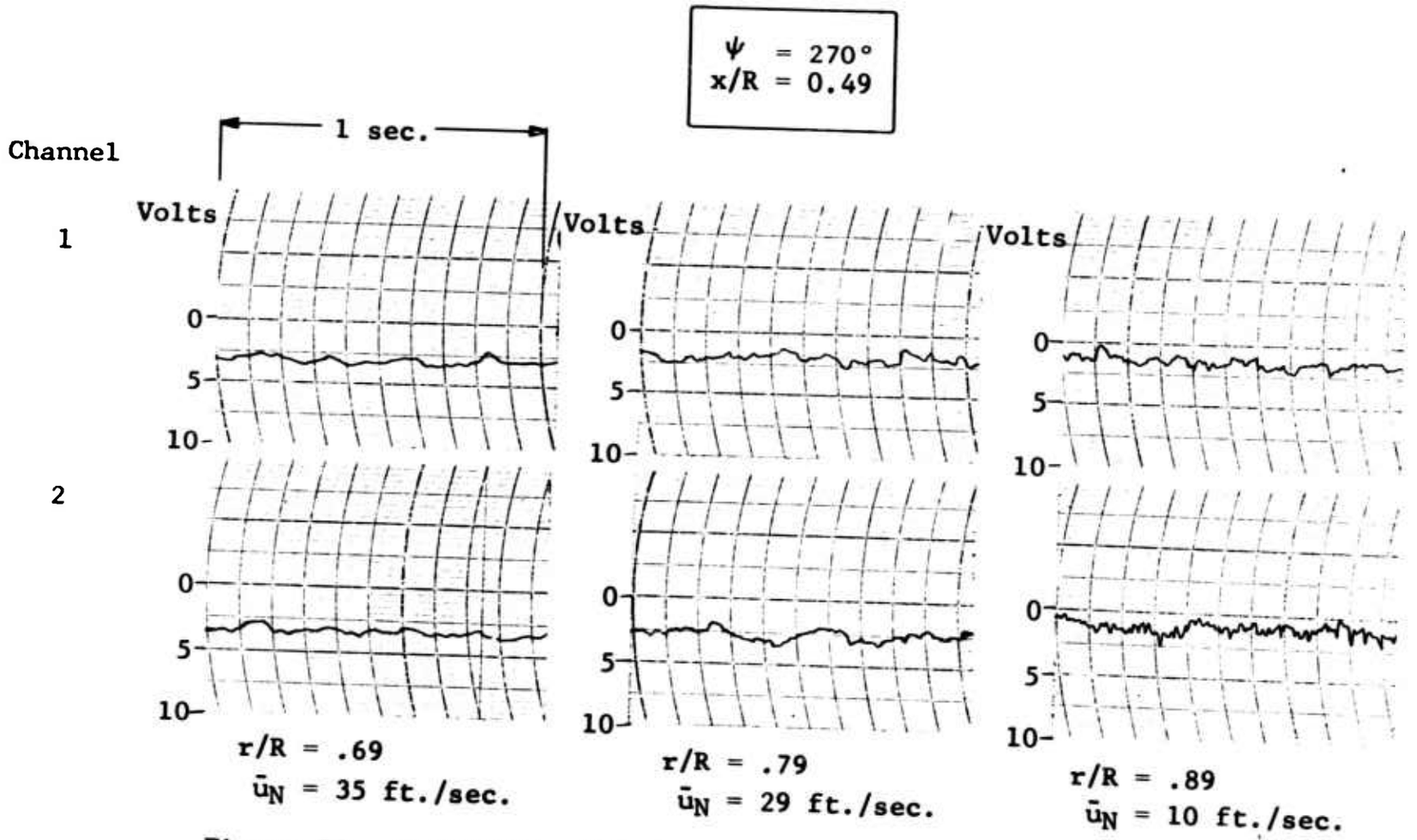

Figure 56. Variation of Instantaneous Velocity During Hovering, OGE, ψ = 270°, x/R = 0.49.

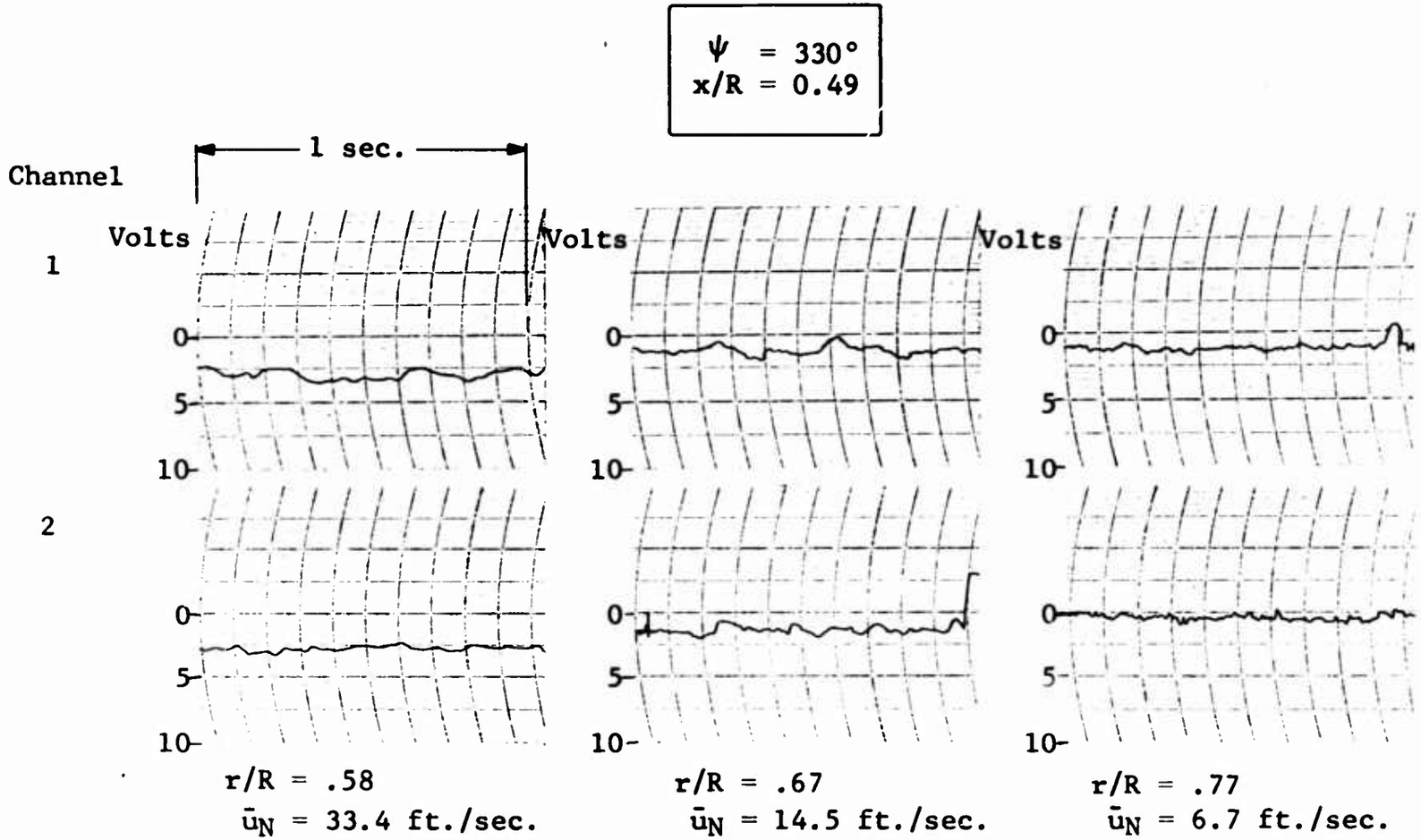

Figure 57. Variation of Instantaneous Velocity During Hovering, OGE, ψ = 330°, x/R = 0.49.

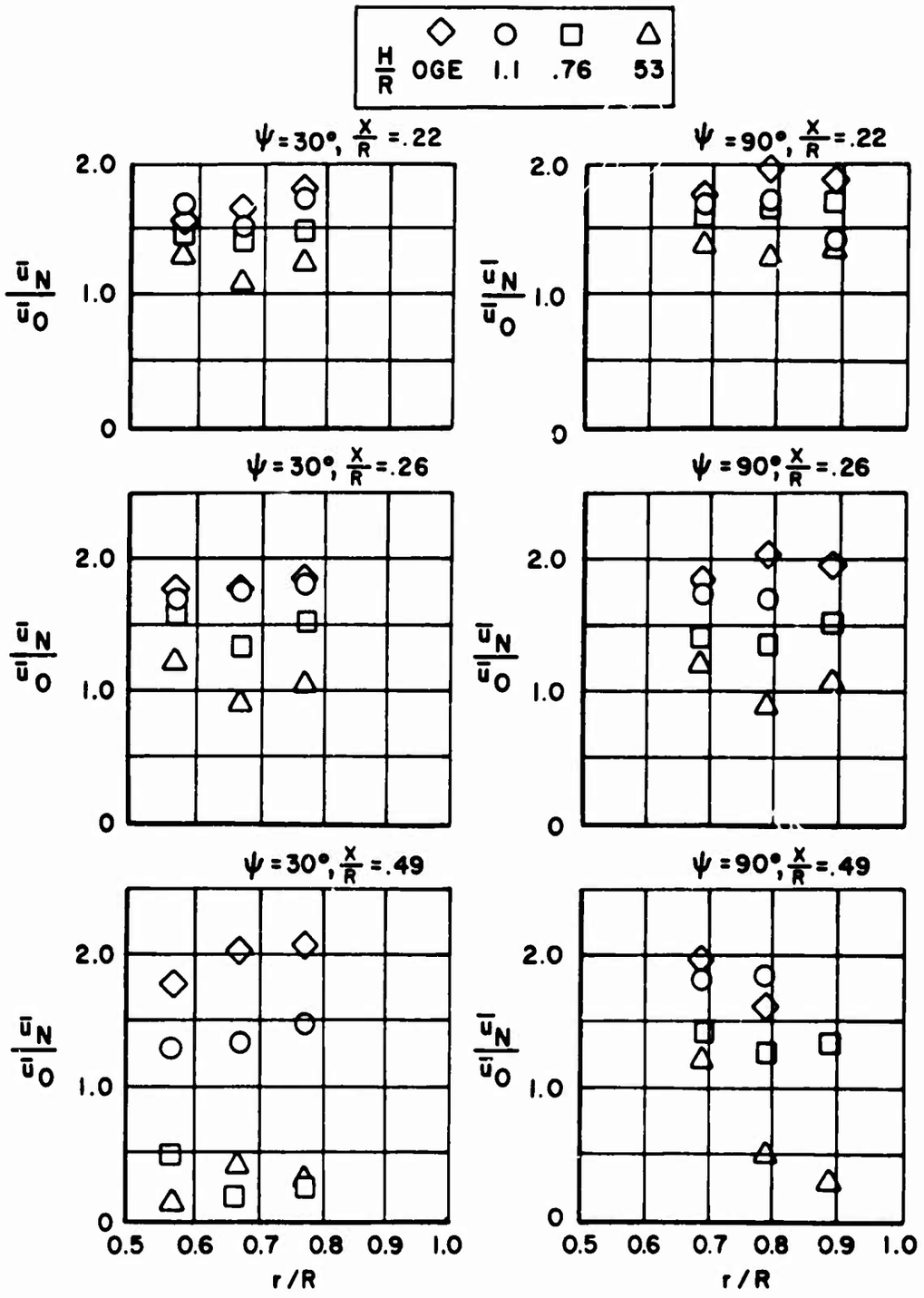

Figure 58. Measured Normal Induced Velocities In-Ground Effect.

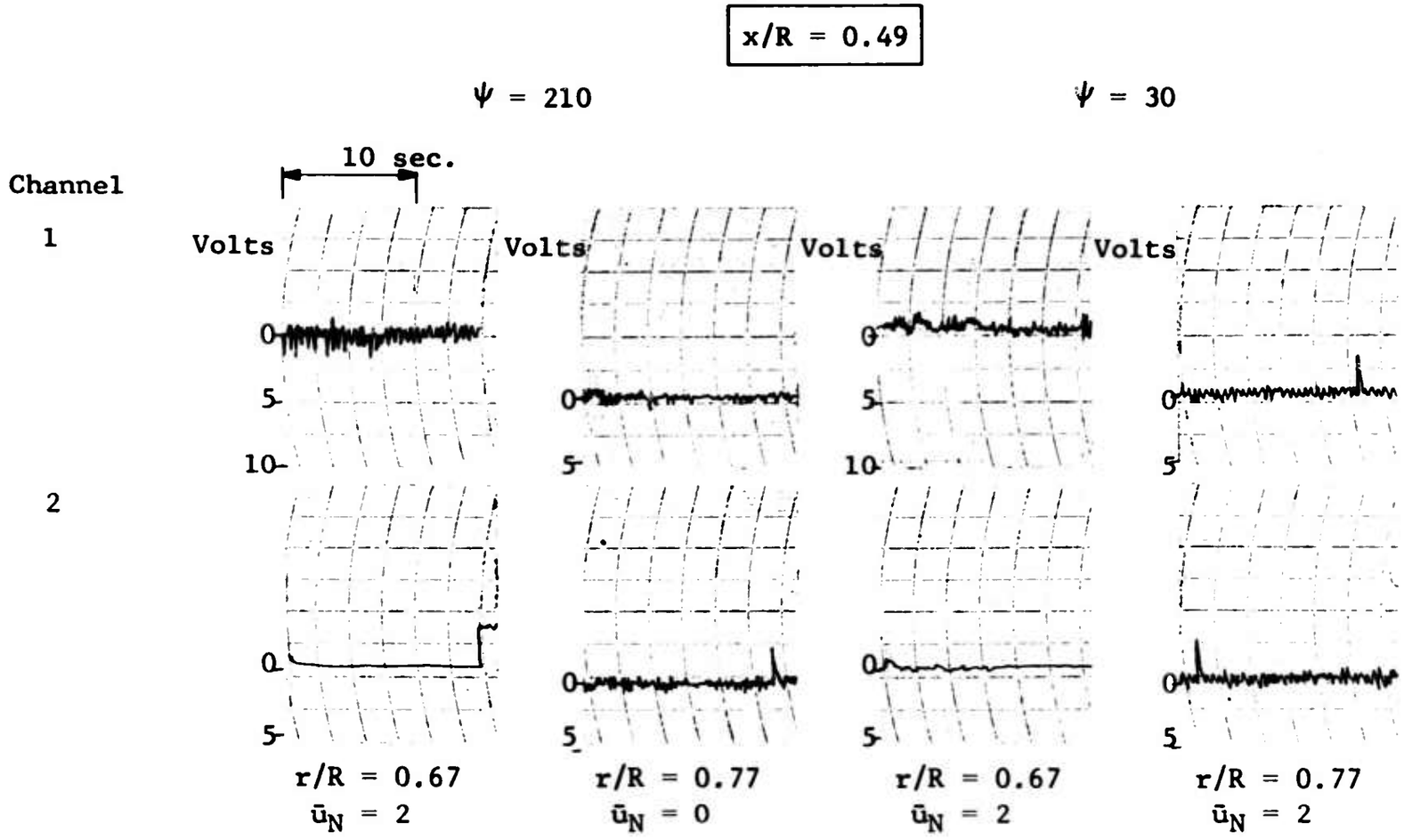

Figure 59. Variation of Instantaneous Velocity During Hovering, In-Ground Effect, h/R = 0.53.

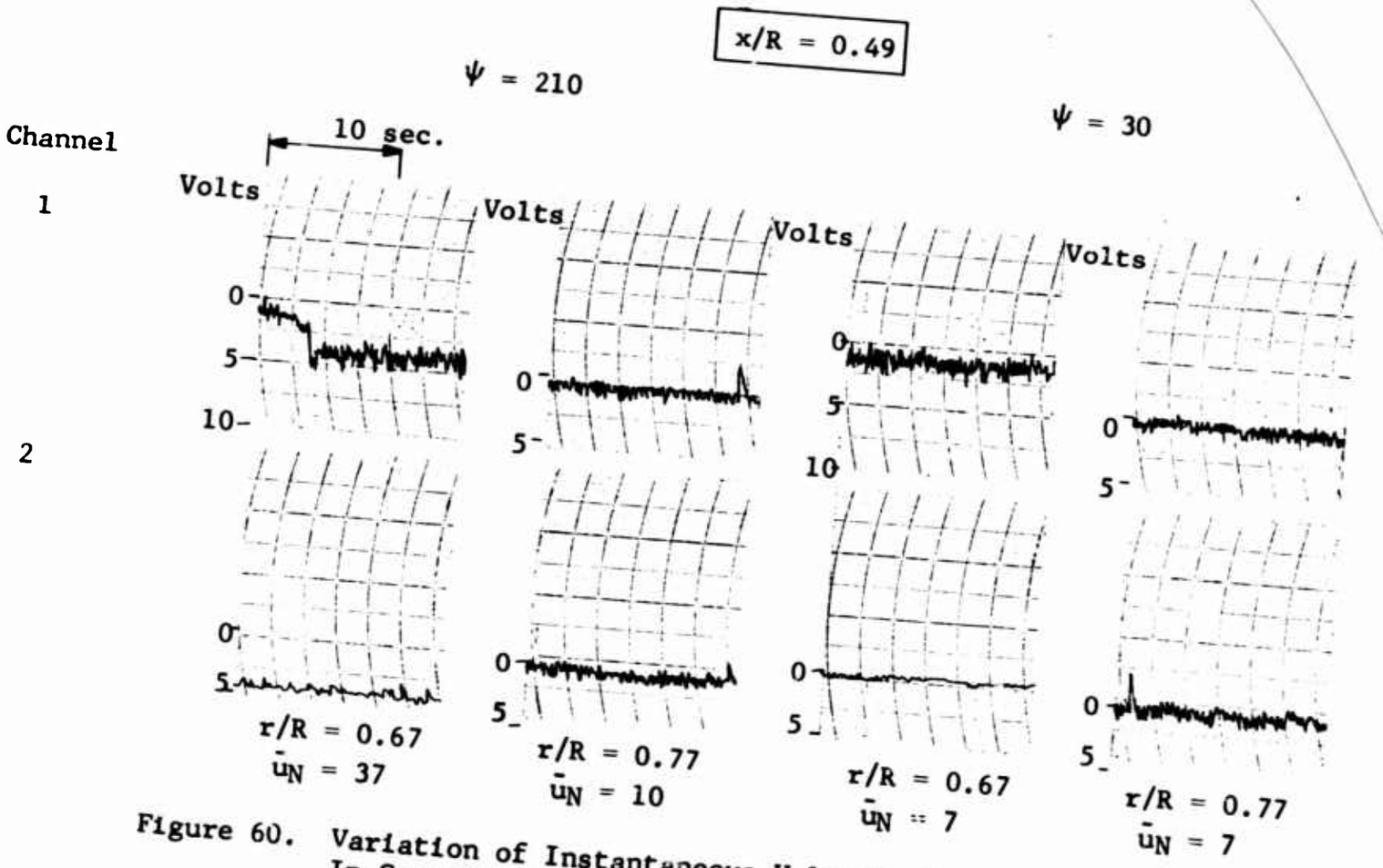

Figure 60. Variation of Instantaneous Velocity During Hovering, In-Ground Effect, h/R = 0.76.

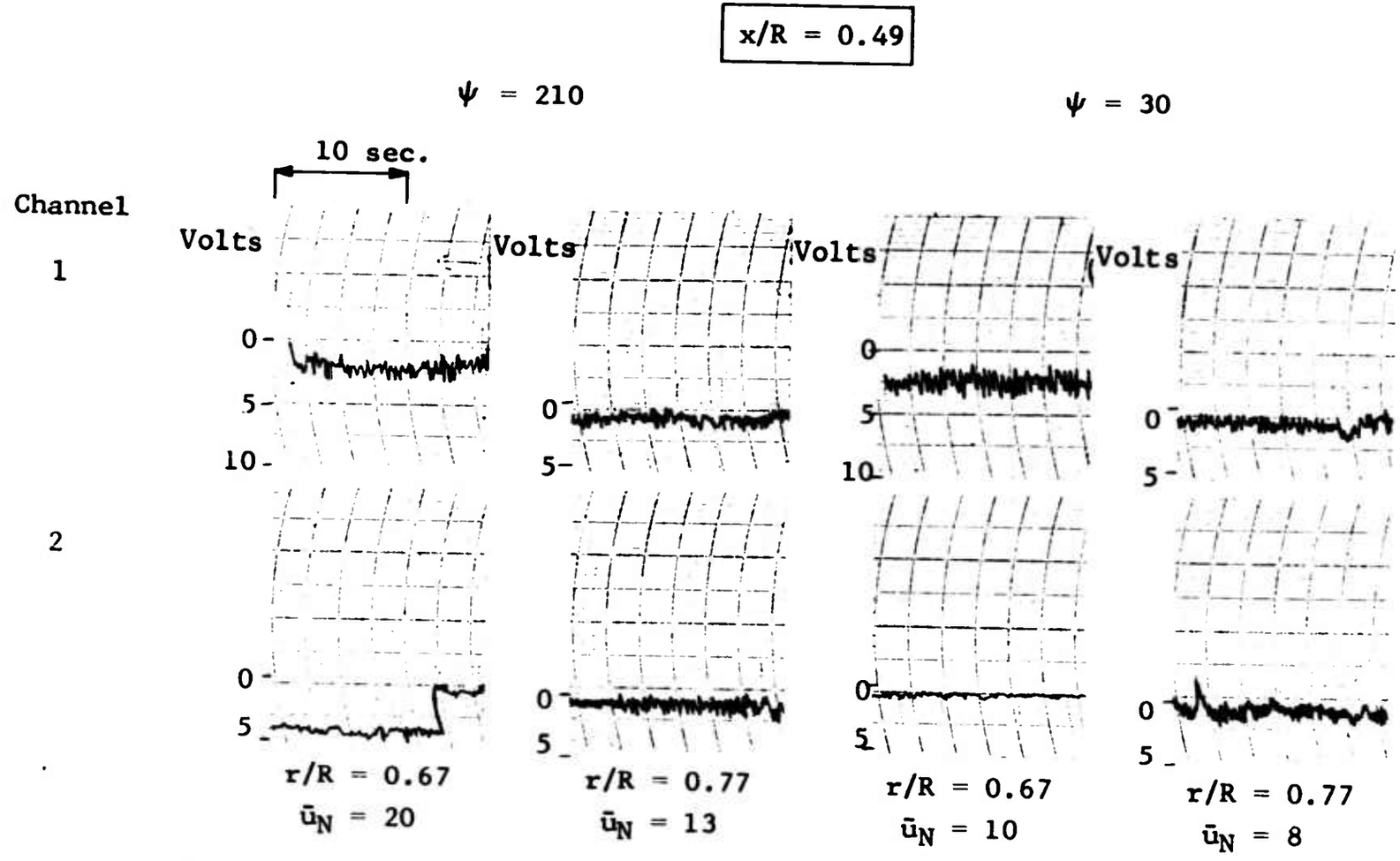

Figure 61. Variation of Instantaneous Velocity During Hovering, In-Ground Effect, h/R = 1.1.

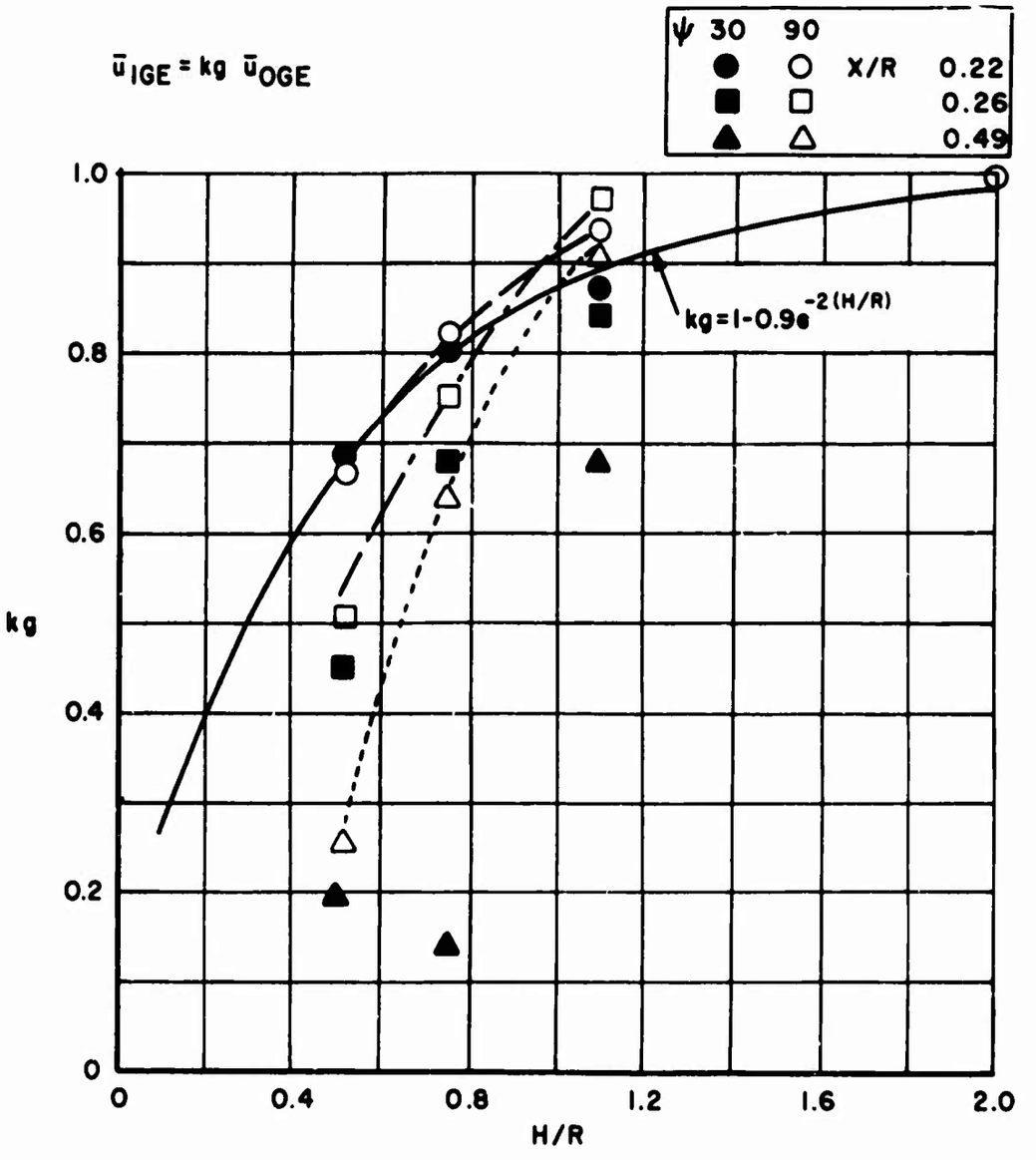

Figure 62. Effect of Ground on Rotor Induced Velocities.

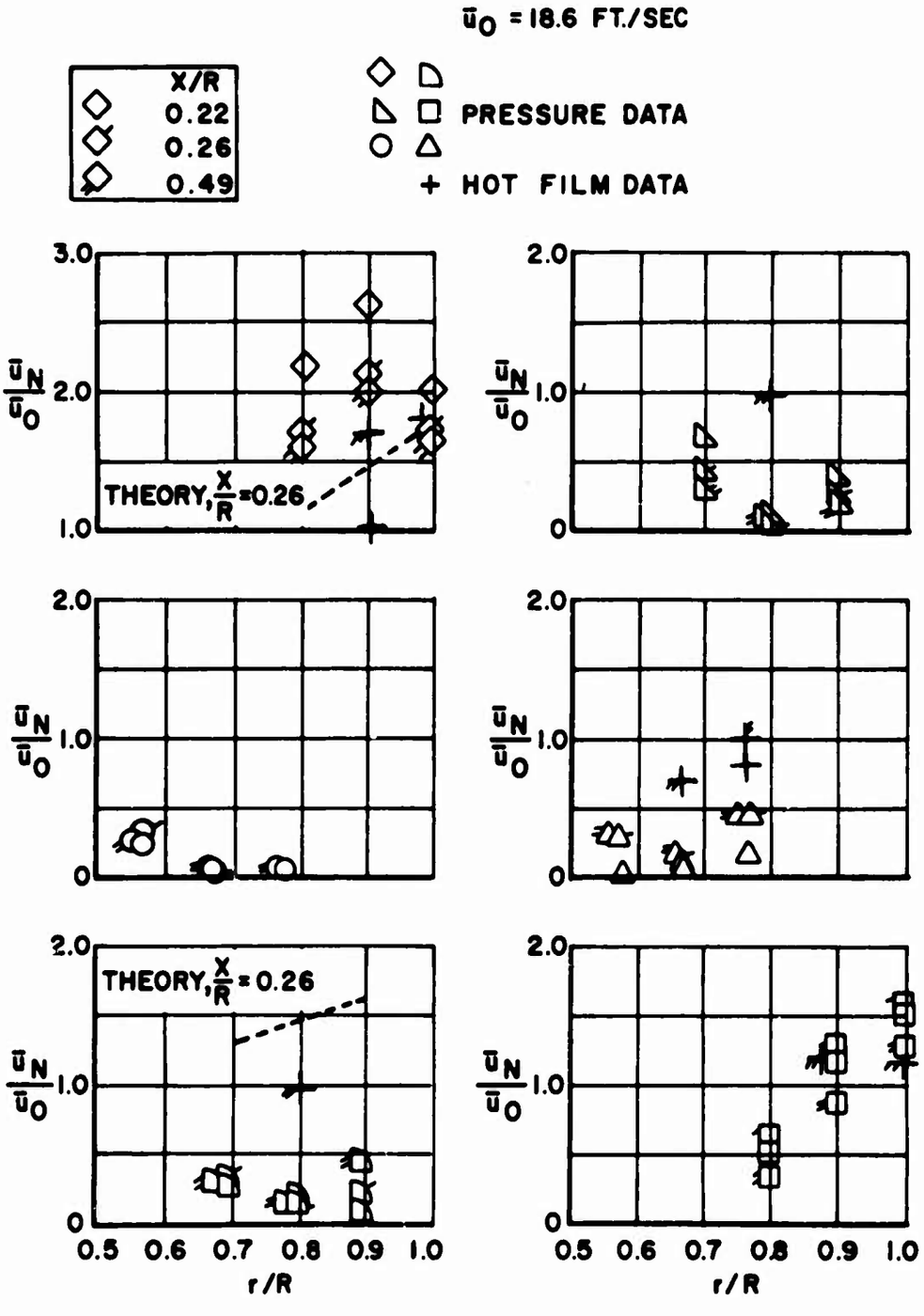

Figure 63. Variation of Normal Velocity With Azimuth and Distance Below the Rotor, V=20 m.p.h.

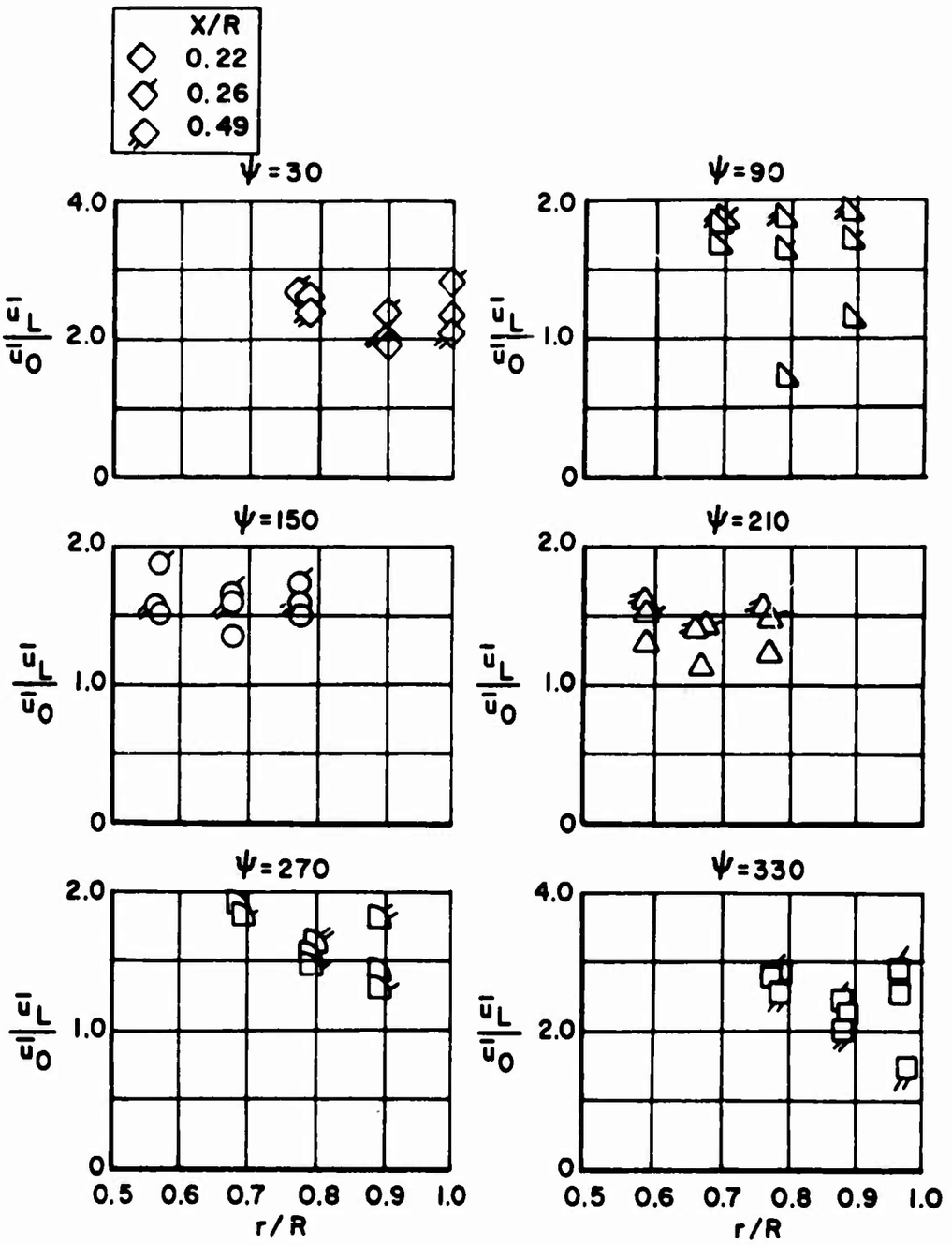

Figure 64. Variation of Longitudinal Velocity With Azimuth and Distance Below the Rotor, V=20 m.p.h. (Pressure Data).

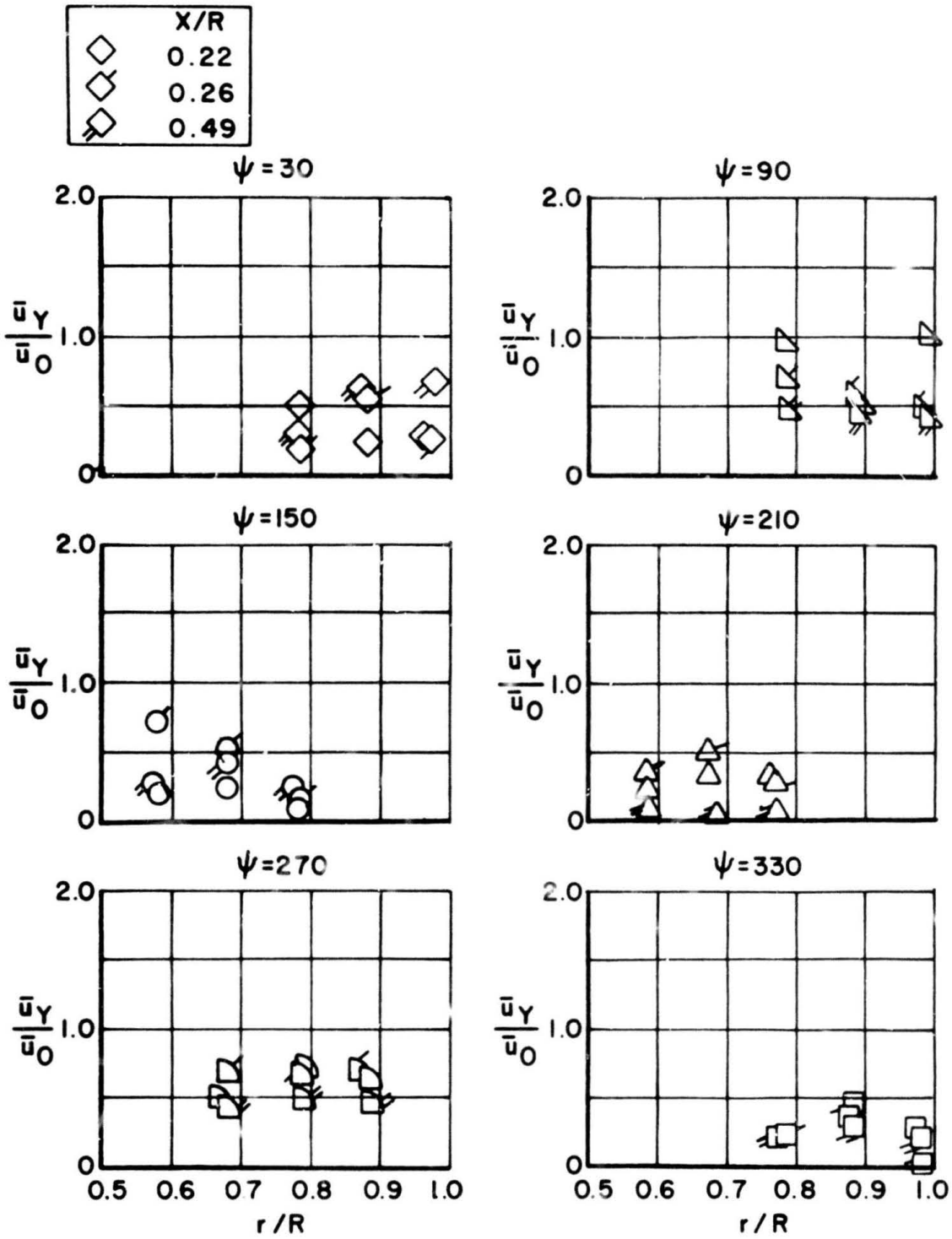

Figure 65. Variation of Lateral Velocity With Azimuth and Distance Below the Rotor, V=20 m.p.h. (Pressure Data).

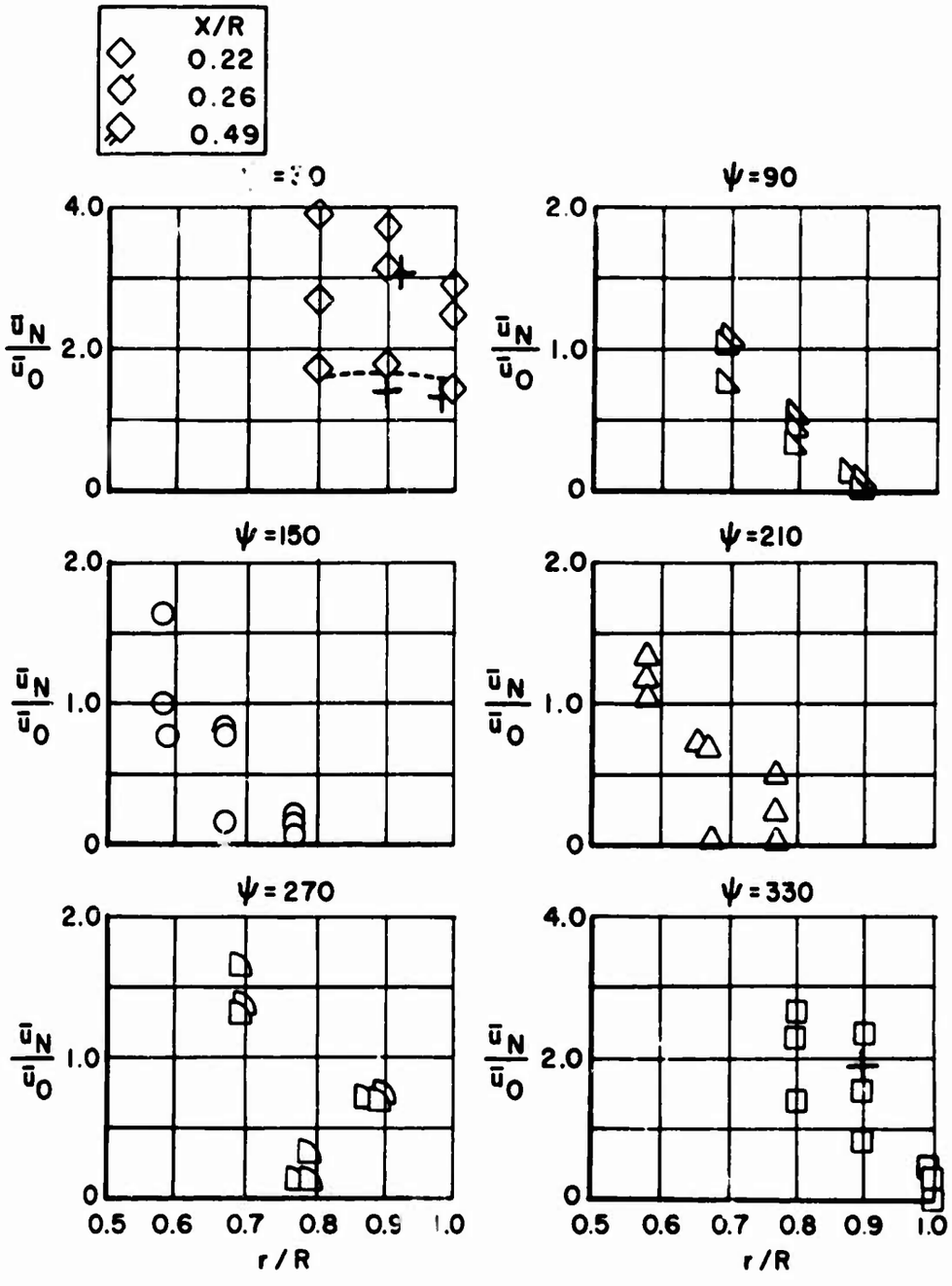

Figure 66. Variation of Normal Velocity With Azimuth and Distance Below the Rotor, V=46 m.p.h.

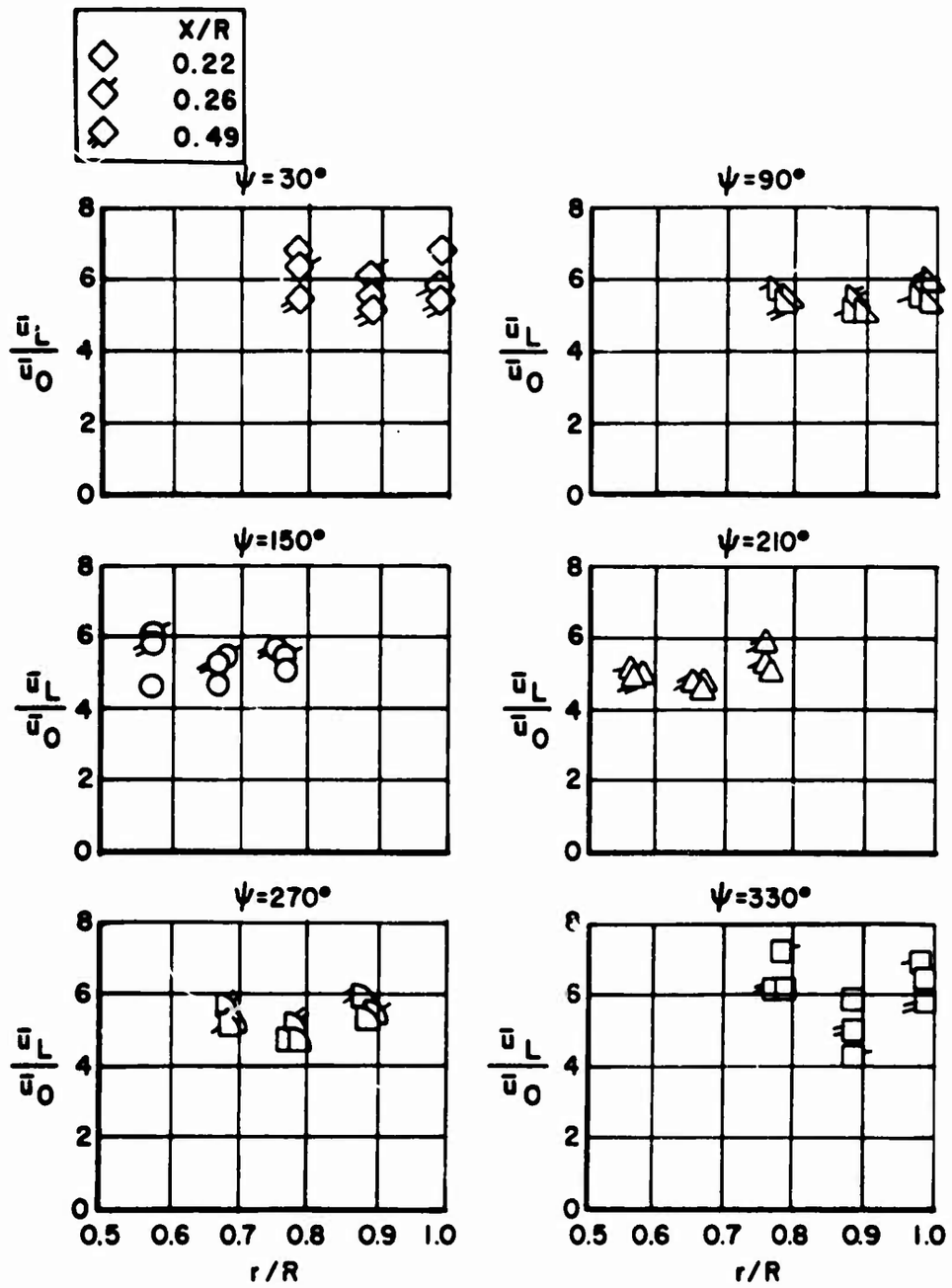

Figure 67. Variation of Longitudinal Velocity With Azimuth and Distance Below the Rotor, V=46 m.p.h. (Pressure Data).

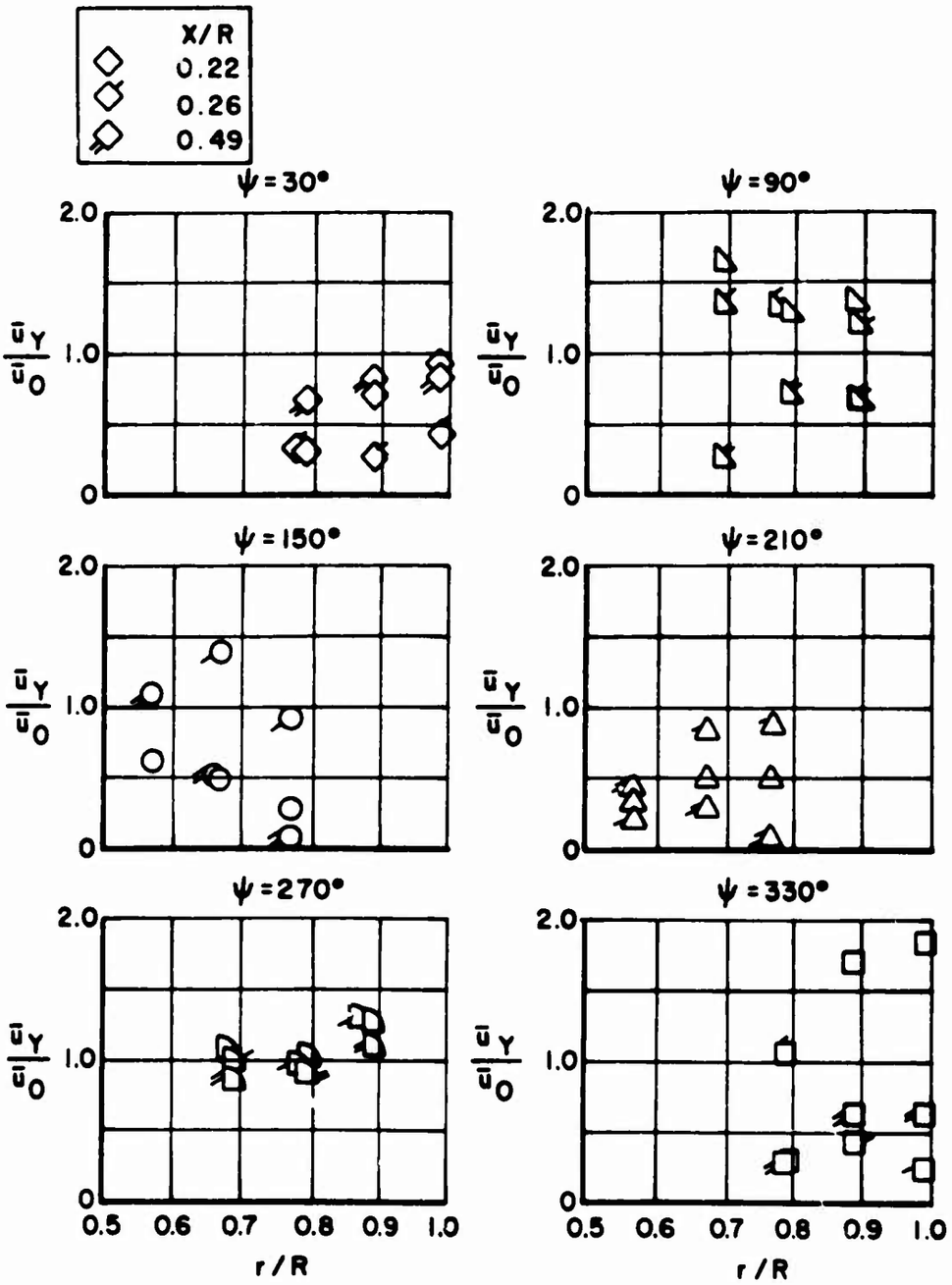

Figure 68. Variation of Lateral Velocity With Azimuth and Distance Below the Rotor, V=46 m.p.h. (Pressure Data).

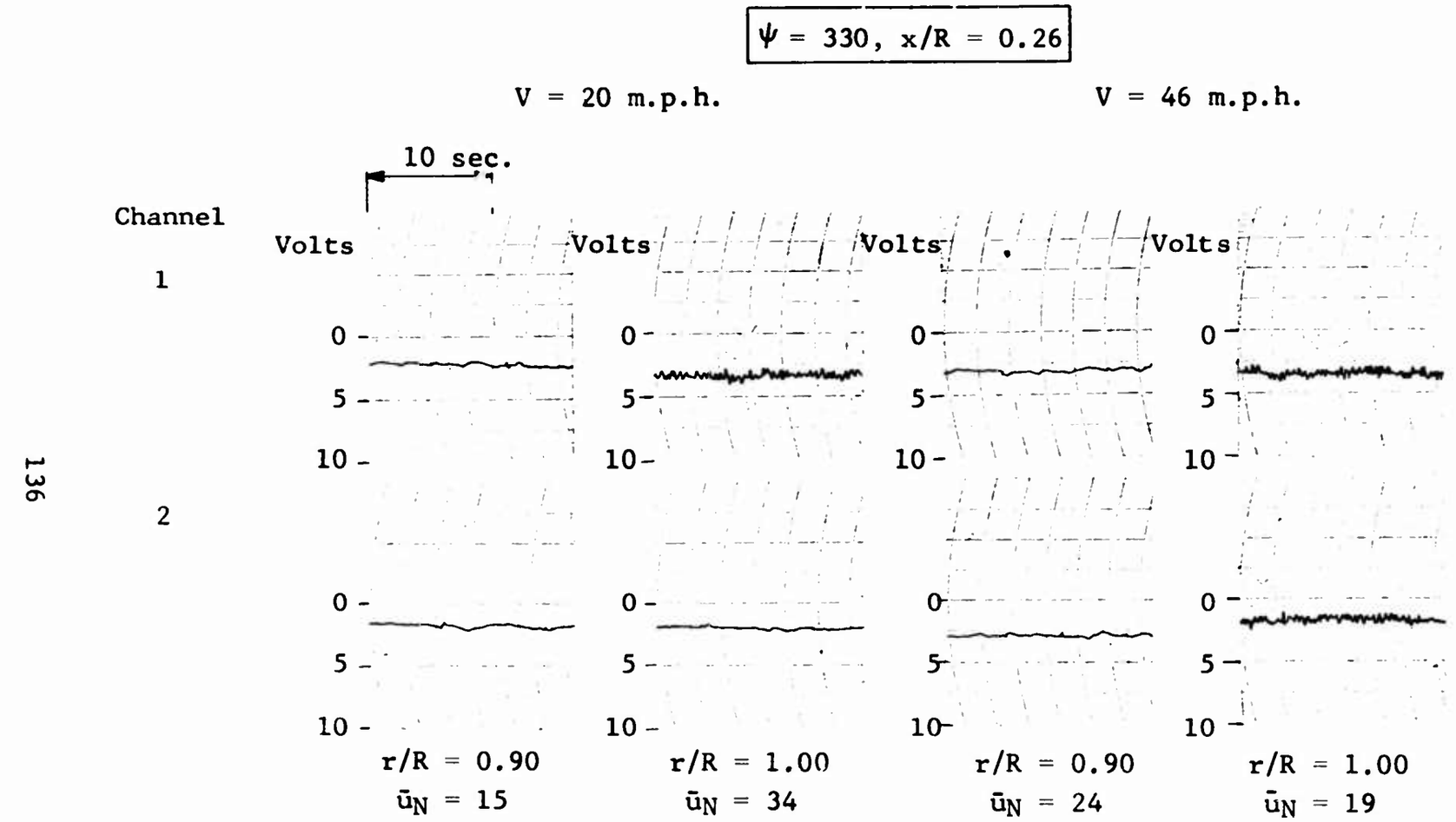

Figure 69. Variation of Instantaneous Velocity During Forward Flight, x/R = 0.26, ψ = 330°.

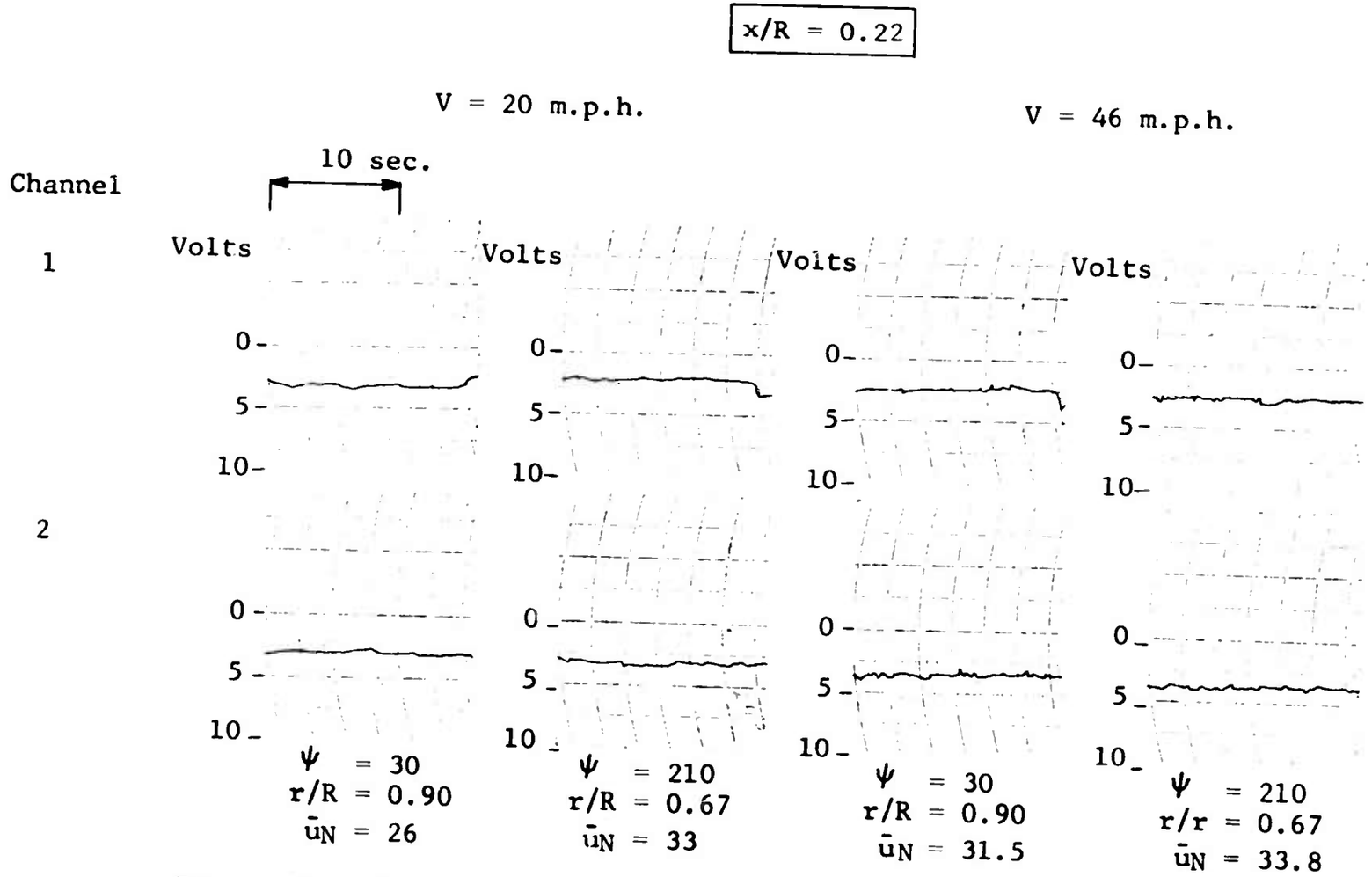

Figure 70. Variation of Instantaneous Velocity During Forward Flight, x/R = 0.22.

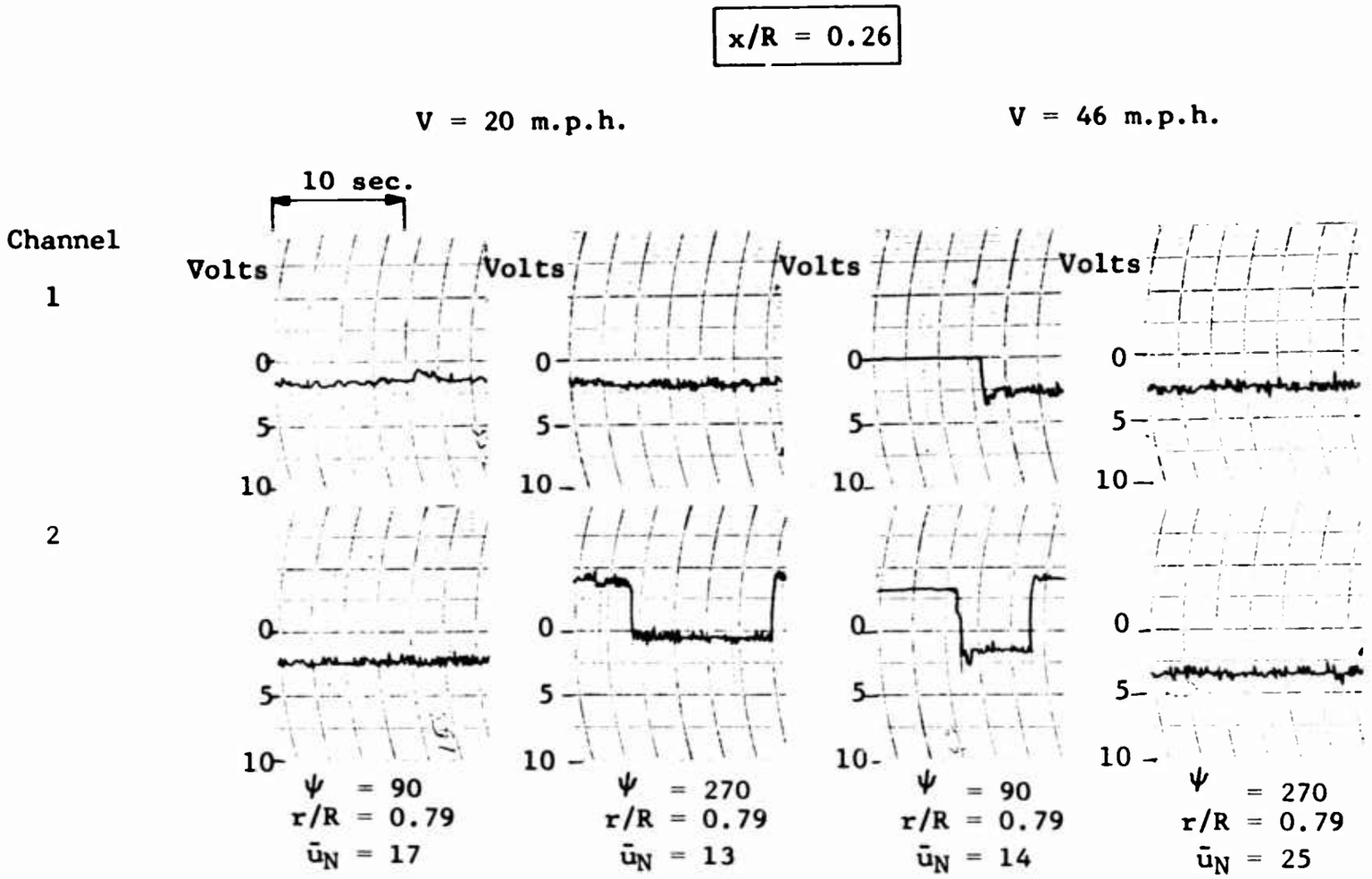

Figure 71. Variation of Instantaneous Velocity During Forward Flight, x/R = 0.26, r/R = 0.29.

TABLE I

DIMENSIONS AND CHARACTERISTICS OF TEST HELICOPTER

GENERAL:	
Gross Weight	1,600 lbs.
Useful Load	590 lbs.
Overall Length	28 ft. 5 in.
Overall Height	8 ft. 2 in.
Rotor Clearance (Ground to tip, rotor static)	7 ft. 2 in.
C.G. Limit (Total Travel)	5 in.
MAIN ROTOR DATA:	
Rotor Diameter	25.29 ft.
Number of Blades	3
Disc Area	502 ft.
Blade Chord	9.562 ft.
Blade Solidity	0.043
Blade Airfoil	NACA 0015
Tip Speed	596 ft./sec.
Rotor r.p.m.	450 r.p.m.
Disc Loading	3.18 lbs./ft.^{2}
Rotor System	Single (Articulated)
POWER PLANT:	
Engine	Lycoming
Power (Takeoff)	180 HP
Power (Normal)	160 HP
PERFORMANCE:	
Maximum Forward Speed	75 kn.
Endurance (2700 Engine r.p.m.)	2 hrs. @ 65 kn.
Hover Ceiling, STOL Day OGE	4,000 ft.
Hover Ceiling, 110°F Day OGE	1,200 ft.

TABLE II

SUMMARY - CALIBRATION DATA

Ch. No.	Description	Transducer	Dropping Resistor	Calibration Resistance	Damping Resistor	Trace Deflection	Calibration Value
2	Collective Pitch Stick	Lockheed WR8	0	470 KΩ	0	ref. ↑ incr.	3.3 in.
3	Altitude	Statham P968-154-350	0	301 KΩ	0	ref. ↓ incr.	380.1 in. H_2O
4	Manifold Pressure	Statham PA208TC-15-350	0	24.9 KΩ	0	ref. ↓ incr.	9.9 in. Hg.
5	Airspeed	Statham PM96TC±.5-350	0	100 KΩ	0	ref. ↓ incr.	3.22 in. H_2O
6	Pitch Attitude	Giannini 3111C-1	75.0 KΩ	5.11 KΩ	0	ref. ↑ nose up	13.8°
7	Normal Acceleration	Statham AJ17-1-350	0	30.1 KΩ	0	ref. ↓ +G	1.43 G
8	Longitudinal Cyclic	Lockheed WR8	0	9.53 KΩ	0	ref. ↓ fwd.	7.4 in.

TABLE II (Continued)

Ch. No.	Description	Transducer	Dropping Resistor	Calibration Resistance	Damping Resistor	Trace Deflection	Calibration Value
9	Rotor r.p.m.	Electro Products 3015A	None	None	0.350 KΩ	↕	None
10	Engine r.p.m.	Electro Products 3015A	None	None	0.35 KΩ	↕	None
11	Common Time Ref.		20.5 KΩ	None	0.35 KΩ	↕	None
12	Hot Film Probe Correla-tion		90.8 KΩ	None	.085 KΩ	*	None

* Hot film probe correlation trace on oscillograph for probes recording on left side of helicopter. Trace off paper for right-side recording.

TABLE III

TYPICAL WEIGHT AND BALANCE

Aircraft Configuration: 22 November 1966

Instrumentation and related structure installed
Doors removed
Cabin trim removed except pilot seat and back
Zero fuel
Full oil; engine and transmissions
Skid wheels stowed forward

A. Most Aft C.G., Booms at Station 137.0

SCALE	WEIGHT (#)	ARM (in.)	MOMENT x 10^{-3} (in.#)
Left Main	680.0	96.0	65.280
Right Main	597.0	96.0	57.312
Tail	28.0	267.0	7.476
Empty Weight	1305.0	99.6	130.068
Pilot	170.0	83.9	14.263
Fuel (25 Gal.)	150.0	107.0	16.050
Gross Weight	1625.0	98.7	160.381

B. Most Forward C.G., Booms at Station 100.0

Left Main	678.0	96.0	65.088
Right Main	608.0	96.0	58.368
Tail	19.0	267.0	5.073
Empty Weight	1305.0	98.5	128.529
Pilot	170.0	83.9	14.263
Zero Fuel	--	--	--
Gross Weight	1475.0	96.8	142.792

The instrumented booms positioned in azimuth are fixed at 180° relative to each other for all test configurations. Thus the composite C.G. of the two booms is not affected by changes in azimuth positions.

Hughes Helicopter Model 269A
Registration No. N-8908F

TABLE IV

FLIGHT TEST SCHEDULE

Flight	Flight Velocity	Boom* Horizontal Station	Position* Vertical	Azimuth Position	Purpose
1	OGE Hover	I	1	1A, 1R	Azimuthal Vel. Var.
2				2A, 2R	
3				3A, 3R	
4			2	1A, 1R	
5				2A, 2R	
6				3A, 3R	
7			3	1A, 1R	
8				3A, 3R	
9	OGE Hover			3A, 3R	
10	0-Foot Hover		3	1A, 1R	Azimuthal Vel. Var. in Ground Effect
11				3A, 3R	
12	3-Foot Hover			1A, 1R	
13				3A, 3R	
14	7-Foot Hover			1A, 1R	
15		I	3	3A, 3R	

TABLE IV (Continued)

Flight	Flight Velocity	Boom* Horizontal Station	Position* Vertical	Azimuth Position	Purpose
16	20 Knots	I	1	1A, 1R	Azimuthal Vel. Var. in Fwd. Flight
17		I II		2A 2R	
18		I II		3R 3A	
19	20 Knots	I	2	1A, 1R	
20		I II		2A 2R	
21		I II		3R 3A	
22		I	3	1A, 1R	
23		I II		2A 2R	
24		I II		3R 3A	
25	40 Knots	I	1	1A, 1R	
26		I II		2A 2R	
27		I II		3R 3A	
28		I	2	1A, 1R	

TABLE IV (Concluded)

Flight	Flight Velocity	Boom* Horizontal Station	Position* Vertical	Azimuth Position	Purpose
29		I		2A	Vel. Var. in Fwd. Flight
		II		2R	
30		I		3R	
		II		3A	
31		I	3	1A, 1R	
32	40 Knots	I		2A	
		II		2R	
33		I		3R	
		II		3A	

*See Table V and Figure 37 for definitions.

TABLE V

TEST NOTATION

Longitudinal Position of Boom

I Station 100.0 (see Figure 36)

Vertical Position of Boom

I Station 100.0

1. W.L. 67.0
2. W.L. 60.5
3. W.L. 25.0

Sensor Coordinates		Sensor					
		PR 1		PR 2		PR 3	
Position	Description	Sta.	B.L.	Sta.	B.L.	Sta.	B.L.
	Rt. Boom:						
3A	Aft	172.4	-50.2	186.6	-54.3	200.8	-58.4
1A	Outboard	100.0	-105.0	100.0	-120.0	100.0	-135.0
2A	Forward	27.6	-50.2	13.4	-54.3	-0.8	-58.4
		PL 1		PL 2		PL 3	
		Sta.	B.L.	Sta.	B.L.	Sta.	B.L.
	Left Boom:						
2R	Aft	172.4	50.2	186.6	54.3	200.8	58.4
1R	Outboard	100.0	105.0	100.0	120.0	100.0	135.0
3R	Forward	27.6	50.2	13.4	54.3	-0.8	58.4

TABLE V (Continued)

Longitudinal Position of Boom

II Station 137.0

Vertical Position of Boom

II Station 137.0

1. W.L. 65.0
2. W.L. 62.0
3. W.L. 25.0

Sensor Coordinates		Sensor					
		PR 1		PR 2		PR 3	
Position	Description	Sta.	B.L.	Sta.	B.L.	Sta.	B.L.
	Rt. Boom:						
3A	Aft	204.0	-62.6	217.6	-68.8	230.8	-75.0
1A	Outboard	137.0	-105.0	137.0	-120.0	137.0	-135.0
2A	Forward	62.0	-36.0	47.2	-37.2	32.4	-38.4
		PL 1		PL 2		PL 3	
		Sta.	B.L.	Sta.	B.L.	Sta.	B.L.
	Left Boom:						
2R	Aft	204.0	62.6	217.6	68.8	230.8	75.0
1R	Outboard	137.0	105.0	137.0	120.0	137.0	135.0
3R	Forward	62.0	36.0	47.2	37.2	32.4	38.4

TABLE VI

CALCULATED VELOCITIES

$\bar{u}_0$ = 25.86 ft./sec.
Flight Condition #5 (x/R = 0.26, Ψ = 150°)

X'_e	r'_e	Blade Azimuth Position	$u_N / \bar{u}_0$	$u_\alpha / \bar{u}_0$	$u_r = \bar{u}_r$
0.306	0.682	A	1.39	-0.0665	
		B	1.33	-0.00911	0.19
		C	1.31	-0.0149	
	0.788	A	1.67	-0.0650	
		B	1.53	-0.00837	0.27
		C	1.52	-0.0104	
	0.906	A	1.98	-0.0510	
		B	1.78	-0.00715	0.36
		C	1.74	-0.00715	

$$X'_e = \frac{X}{R_e}$$

$$r'_e = \frac{r}{R_e}$$

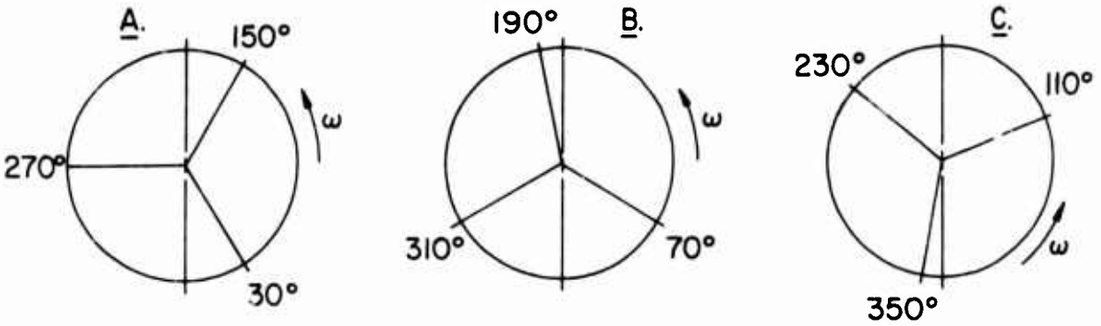

TABLE VII

HELICOPTER FLIGHT DATA

Flight No.	Gross Weight (lb.)	Collective (in.)	Pitch (deg.)	Longitudinal Cyclic (in.)
1	1558	5.25	2.7	1.99
2	1605	5.62	-.3	3.25
3	1597	5.9	-.74	2.82
4	1566	5.5	.29	3.3
5	1621	5.65	2.2	2.7
6	1572	5.5	1.52	3.0
7	1608	5.45	.46	3.15
8	1600	5.7	1.45	3.2
9	1594	5.6	1.45	3.2
10	1586	5.6	-	-
11	1586	-	-	-
12	1586	-	-	-
13	1586	-	-	-
14	1586	-	-	-
15	1586	-	-	-
16	1575	4.24	-.2	.2
17	1590	-	-	-
18	1585	-	-	-
19	1569	-	-	-
20	1609	-	-	-

TABLE VII (Continued)

Flight No.	Gross Weight (lb.)	Collective (in.)	Pitch (deg.)	Longitudinal Cyclic (in.)
21	1598	4.24	-.2	.2
22	1618	-	-	-
23	1602	-	-	-
24	1609	-	-	-
25	1575	4.4	1	1
26	1590	-	-	-
27	1585	-	-	-
28	1569	-	-	-
29	1609	-	-	-
30	1599	-	-	-
31	1618	-	-	-
32	1602	-	-	-
33	1609	-	-	-

TABLE VIII

CALCULATED VELOCITIES

V m.p.h.	$\bar{u}_o$	Flight No.	Azimuth	χ	χ'	r'	χ_1'	R_1	r_1'	Blade Position*	$u_N/\bar{u}_o$
20	18.55	34(a)	30°	57.57°	0.23	1.0	0.851	10.1	0.703	A	1.82
										B	1.70
										C	1.65
46	9.32	34(b)	30°	79.93	0.23	1.0	0.889	9.61	0.658	A	1.64
										B	1.56
										C	1.55

*(See Table VI)

V. CONCLUSIONS

The results of the work performed in this program lead to the following conclusions:

1. The feasibility of obtaining full-scale induced velocity data by use of the measuring techniques utilized was established.

2. Hovering data show that the normal induced velocity increased with increasing radial distance. Radial induced velocities are on the order of one-half the average normal induced velocity, but tangential induced velocities are less than ten percent of this value.

3. Test data obtained for hovering while in ground effect show that the induced velocity reductions are similar to those obtained by earlier researchers.

4. Significant azimuth variations of normal induced velocities were measured in forward flight.

5. Theoretically calculated values of the induced velocities show some correlation with the hovering test data. The theory does not provide good correlation with the forward speed test data in the proximity of the rotor.

6. Calculations indicate that the effect of the fuselage on the induced velocities is negligible for the Model 269-A helicopter.

7. Experimental error for time-averaged velocity values ranged from 1 percent to 5 percent.

8. Experimental error for instantaneous velocities ranged from 3 percent to 10 percent.

VI. REFERENCES

1. Heyson, H. H., and Katzoff, S., "Induced Velocities Near a Lift-Rotor With Nonuniform Disc Loading", NACA Report 1319, 1957.

2. Crimi, P., "Theoretical Prediction of the Flow in the Wake of a Helicopter Rotor", CAL No. BB-1994-S-1, Cornell Aeronautical Laboratory, Inc., Buffalo, N.Y., September 1965.

3. Davenport, F. D., "Analysis of Propeller and Rotor Performance in Static and Axial Flight by an Explicit Vortex Influence Technique", R-372, Vertol Division, The Boeing Company, Morton, Pennsylvania, February, 1965.

4. Goland, L., "An Investigation of the Induced Velocity in the Vicinity of a Propeller and Its Influence on Wing Lift", a Dissertation in Mechanical Engineering, University of Pennsylvania, 1962.

5. Betz, A., "Applied Airfoil Theory", Vol. IV, Edited by W. F. Durand, Dover Publications, Incorporated, New York, New York, 1943.

6. Castles, W., Jr., and Deleeux, J. H., "The Normal Component of the Induced Velocity in the Vicinity of a Lifting Rotor and Some Examples of Its Application", NACA Report 1184, 1954.

7. Knight, M., and Hefner, R. A., "Analysis of Ground Effect on the Lifting Airscrew", NACA TN 835, 1941.

8. Zbrozek, J., "Ground Effect on the Lifting Rotor", Br. ARC Royal Aircraft Establishment Technical Note, No. Aero 1903, 1947.

9. Fradenburgh, E. A., "Flow Field Measurements for a Hovering Rotor Near the Ground", Paper Presented Before the American Helicopter Society's Fifth Annual Forum, 1958.

10. Fukushima, T., et al., "Investigation of the Contaminated Atmosphere Surrounding Hovering Rotors", Dynasciences Corporation Report DCR-206, March 1966.

DISTRIBUTION

US Army Materiel Command	6
US Army Aviation Materiel Command	5
United States Continental Army Command	1
United States Army, Pacific	1
Chief of R&D, DA	2
Director of Defense Research and Engineering	2
US Army R&D Group (Europe)	2
US Army Aviation Materiel Laboratories	23
US Army Limited War Laboratory	1
US Army Human Engineering Laboratories	1
Army Aeronautical Research Laboratory, Ames Research Center	1
US Army Research Office-Durham	1
Plastics Technical Evaluation Center	1
US Army Test and Evaluation Command	1
US Army Electronics Command	2
US Army Combat Developments Command, Fort Belvoir	2
US Army Combat Developments Command Experimentation Command	1
US Army Combat Developments Command Transportation Agency	1
US Army Combat Developments Command Aviation Agency	1
US Army Ordnance Weapons Command	1
Ordnance Special Weapons-Ammunitions Command	1
US Army Aviation School	1
Assistant Chief of Staff for Force Development	1
US Army Tank-Automotive Command	2
US Army Aviation Test Board	4
US Army Aviation Test Activity, Edwards AFB	2
Air Force Flight Test Center, Edwards AFB	2
US Army Field Office, AFSC, Andrews AFB	1
Air Force Materials Laboratory, Wright-Patterson AFB	2
Air Force Flight Dynamics Laboratory, Wright-Patterson AFB	4
Systems Engineering Group, Wright-Patterson AFB	2
Naval Air Systems Command, DN	11
Office of Naval Research	1
US Naval Research Laboratory	1
US Naval Air Test Center, Patuxent River	1
Commandant of the Marine Corps	1
Marine Corps Liaison Officer, US Army Transportation School	1
Testing and Development Division, US Coast Guard	1
Manned Spacecraft Center, NASA	1
Langley Research Center, NASA	1
NASA Scientific and Technical Information Facility	2

NAFEC Library (FAA)	2
US Army Aviation Human Research Unit	1
US Army Board for Aviation Accident Research	1
Bureau of Safety, Civil Aeronautics Board	2
US Naval Aviation Safety Center, Norfolk	1
US Naval Air Station, Norfolk	1
Federal Aviation Agency, Washington, DC	3
Federal Aviation Agency, Jamaica, NY	1
1st Cavalry Division	1
US Government Printing Office	1
Defense Documentation Center	20

Unclassified

Security Classification

DOCUMENT CONTROL DATA - R & D

(Security classification of title, body of abstract and indexing annotation must be entered when the overall report is classified)

1. ORIGINATING ACTIVITY (Corporate author) Dynasciences Corporation Blue Bell, Pennsylvania	2a. REPORT SECURITY CLASSIFICATION Unclassified 2b. GROUP

3. REPORT TITLE

Theoretical and Experimental Investigation of the Instantaneous Induced Velocity Field in the Wake of a Lifting Rotor

4. DESCRIPTIVE NOTES (Type of report and inclusive dates)

Final Report

5. AUTHOR(S) (First name, middle initial, last name)

Miller, N.
Tang, J. C.
Perlmutter, A. A.

6. REPORT DATE January 1968	7a. TOTAL NO. OF PAGES 170	7b. NO. OF REFS 10
8a. CONTRACT OR GRANT NO. DA 44-177-AMC-383(T) b. PROJECT NO. Task 1F125901A13903 c. d.	9a. ORIGINATOR'S REPORT NUMBER(S) USAAVLABS Technical Report 67-68 9b. OTHER REPORT NO(S) (Any other numbers that may be assigned this report) Dynasciences Report No. DCR-227	

10. DISTRIBUTION STATEMENT

This document has been approved for public release and sale, its distribution is unlimited.

11. SUPPLEMENTARY NOTES	12. SPONSORING MILITARY ACTIVITY U.S. Army Aviation Materiel Laboratories, Fort Eustis, Virginia

13. ABSTRACT

Measurements have been made of the instantaneous and time-averaged values of the induced velocities in the wake of a full-scale helicopter in actual steady flight conditions. These measurements were made with three-dimensional pitot static and two-dimensional hot film probes. The test setup provided for measurements at several radial, axial, and azimuthal positions relative to the rotor centerline.

Simple, analytical methods are formulated to predict the instantaneous and time-averaged, induced velocities in the rotor wake.

Calculated values of the induced velocities are compared with the experimental data, and agreement is obtained for the hovering flight condition.

DD FORM 1 NOV 68 1473 REPLACES DD FORM 1473, 1 JAN 64, WHICH IS OBSOLETE FOR ARMY USE.

Unclassified

Security Classification

Unclassified

Security Classification

14. KEY WORDS	LINK A		LINK B		LINK C	
	ROLE	WT	ROLE	WT	ROLE	WT
Helicopter downwash velocity measurements						

Unclassified

Security Classification

292-68